ENHANCED PHOTOCATALYTIC ACTIVITY OF COPPER-DOPED TITANIUM OXIDE USING ZINC OXIDE HETEROJUNCTION AND IODIDE CO-DOPING FOR WATER TREATMENT APPLICATION

MASOUMEH DORRAJ

FACULTY OF SCIENCE
UNIVERSITY OF MALAYA
KUALA LUMPUR

2018

ENHANCED PHOTOCATALYTIC ACTIVITY OF COPPER-DOPED TITANIUM OXIDE USING ZINC OXIDE HETEROJUNCTION AND IODIDE CO-DOPING FOR WATER TREATMENT APPLICATION

MASOUMEH DORRAJ

THESIS SUBMITTED IN FULFILMENT OF THE REQUIREMENTS FOR THE DEGREE OF DOCTOR OF PHILOSOPHY

DEPARTMENT OF CHEMISTRY
FACULTY OF SCIENCE
UNIVERSITY OF MALAYA
KUALA LUMPUR

2018

UNIVERSITY OF MALAYA

ORIGINAL LITERARY WORK DECLARATION

Name of Candidate: **Masoumeh Dorraj**

Matric No: **SHC140096**

Name of Degree: **DOCTOR OF PHILOSOPHY (EXCEPT MATHEMATIC & SCIENCE PHILOSOPHY)**

Title of Project Paper/Research Report/Dissertation/Thesis ("this Work"):

ENHANCED PHOTOCATALYTIC ACTIVITY OF COPPER-DOPED TITANIUM OXIDE USING ZINC OXIDE HETEROJUNCTION AND IODIDE CO-DOPING FOR WATER TREATMENT APPLICATION

Field of Study: **CATALYSIS**

I do solemnly and sincerely declare that:

(1) I am the sole author/writer of this Work;
(2) This Work is original;
(3) Any use of any work in which copyright exists was done by way of fair dealing and for permitted purposes and any excerpt or extract from, or reference to or reproduction of any copyright work has been disclosed expressly and sufficiently and the title of the Work and its authorship have been acknowledged in this Work;
(4) I do not have any actual knowledge nor do I ought reasonably to know that the making of this work constitutes an infringement of any copyright work;
(5) I hereby assign all and every rights in the copyright to this Work to the University of Malaya ("UM"), who henceforth shall be owner of the copyright in this Work and that any reproduction or use in any form or by any means whatsoever is prohibited without the written consent of UM having been first had and obtained;
(6) I am fully aware that if in the course of making this Work I have infringed any copyright whether intentionally or otherwise, I may be subject to legal action or any other action as may be determined by UM.

Candidate's Signature Date:

Subscribed and solemnly declared before,

Witness's Signature Date:

Name:

ENHANCED PHOTOCATALYTIC ACTIVITY OF COPPER-DOPED TITANIUM OXIDE USING ZINC OXIDE HETEROJUNCTION AND IODIDE CO-DOPING FOR WATER TREATMENT APPLICATION

ABSTRACT

Doping titanium dioxide (TiO_2) with 3d transition metal elements is a popular technique that facilitates its visible-light-induced photocatalytic performance. However, many experimental reports indicate that these dopants in TiO_2 lattice are recombination centers, which resulted in limited enhancement of photocatalytic activity. Thus, designing a photocatalyst composed of semiconductor heterojunctions and nonmetal co-dopants are viable approaches to address this challenge. In this thesis, Cu doped TiO_2 was coupled with ZnO (Cu-TiO_2/ZnO) at different molar ratios by sol-gel method and subsequent precipitation. The apparent rate constants are 0.0011, 0.0166, and 0.0306 min^{-1} for TiO_2, 3% Cu-TiO_2, and 3% Cu-TiO_2/30% ZnO, respectively. The photocatalytic activity of the 3% Cu-TiO_2/30% ZnO nanocomposite is approximately 2-folds higher than that of 3% Cu-TiO_2 nanoparticles and 28-folds higher than that of bare TiO_2 during degradation of methyl orange (MO). The enhanced photocatalytic activity of the Cu-TiO_2/ZnO nanocomposites was mainly attributed to the heterojunction formation, which allowed the efficient separation of photoinduced electron−hole pairs at the interface. Cu-I-co-doped TiO_2 nanoparticle photocatalysts responsive to visible light were also prepared through hydrothermal treatment and calcined at different temperatures (350, 450 and 550 °C). The co-doped powders calcined at 350 °C showed the largest BET surface area and the decrease in photoluminescence intensity demonstrated that the electron-hole recombination was also decreased. The synthesis of co-doped TiO_2, mono-doped TiO_2 and pure TiO_2 was performed at this optimized temperature. The presence of Cu^{2+} and I^{5+} in the XPS spectrum indicated that the Cu^{2+} and I^{5+} substituted the titanium (Ti^{4+}) in TiO_2 lattice. The degradation rate constant (k)

of Cu-I-co-doped TiO_2 (0.030 min^{-1}) is about 1.67 and 1.5 larger as compared to the *k* value of the Cu mono-doped TiO_2 (0.018 min^{-1}) and I mono-doped TiO_2 (0.020 min^{-1}) under visible light irradiation. The enhanced photocatalytic activity is due to the strong visible light absorption and effective separation of the photogenerated charges caused by the Cu and I co-dopants.

Keywords: Copper-doped titanium dioxide, photocatalytic activity, heterojunction, co-doping

PENINGKATAN AKTIVITI FOTO-PEMANGKINAN TITANIUM OKSIDA DIDOP DENGAN TEMBAGA MENERUSI KAEDAH HETERO-SIMPANGAN ZINK OKSIDA DAN PENDOPAN BERSAMA IODIDE UNTUK PERAWATAN AIR

ABSTRAK

Titanium dioksida (TiO_2) yang didopkan dengan unsur logam peralihan 3d adalah teknik yang terbaik dalam memperbaiki aktiviti foto-pemangkinan. Walau bagaimanapun, banyak laporan menunjukkan bahawa dopan-dopan yang berada dalam kekisi TiO_2 bertindak sebagai pusat rekombinasi, yang merencatkan aktiviti foto-pemangkinan. Oleh itu, reka bentuk foto-pemangkin yang terdiri daripada semikonduktor heterosimpang dan ko-dop bukan logam adalah pendekatan yang mampu menangani cabaran tersebut. Dalam tesis ini, TiO_2 didopkan dengan Cu dan digabungkan dengan ZnO (Cu-TiO_2 / ZnO) dengan nisbah molar yang berlainan melalui kaedah sol-gel dan penghabluran berturutan. Pemalar kadar yang jelas adalah 0.0011, 0.0166, dan 0.0306 min^{-1} bagi TiO_2, 3% Cu-TiO_2, dan 3% Cu-TiO_2/30% ZnO. Aktiviti foto-pemangkinan nanokomposit Cu-TiO_2/30% ZnO adalah 3% lebih tinggi daripada nanozarah Cu-TiO_2 3% dan 28 kali ganda lebih tinggi daripada TiO_2 yang tidak didopkan semasa penguraian metil jingga (MO). Peningkatan aktiviti foto-pemangkinan oleh nanokomposit Cu-TiO_2/ZnO adalah disebabkan oleh pembentukan hetero-simpang, yang membolehkan pemisahan yang cekap pasangan elektron-lubang foto-aruhan antara fasa. Foto-pemangkin nanopartikel TiO_2 Cu-I-ko-dop yang responsif terhadap cahaya nampak disediakan melalui rawatan hidroterma dan dikalsin pada suhu yang berbeza (350, 450 dan 550 °C). Serbuk foto-pemangkin yang didopkan dan dikalsinkan pada suhu 350 °C menunjukkan kawasan permukaan BET terbesar dan penurunan keamatan foto-pencahayaan. Ini menunjukkan bahawa penggabungan semula elektron-lubang juga berkurangan. Sintesis TiO_2 dop, ko-dop dan TiO_2 tulen telah dilakukan pada suhu

optimum ini. Kehadiran Cu^{2+} dan I^{5+} dalam spektrum XPS menunjukkan bahawa Cu^{2+} dan I^{5+} menggantikan titanium (Ti^{4+}) dalam kekisi TiO_2. Kekerapan kadar degradasi (k) Cu-I-ko-dop TiO_2 (0.030 min^{-1}) adalah kira-kira 1.67 dan 1.5 lebih besar berbanding dengan nilai k TiO_2 dop Cu (0.018 min^{-1}) dan TiO_2 dop I (0.020 min^{-1}) di bawah sinaran cahaya nampak. Aktiviti foto-pemangkinan yang dipertingkatkan adalah disebabkan penyerapan cahaya yang ketara dan pemisahan yang berkesan bagi caj foto-penghasilan yang disebabkan oleh ko-dopan Cu dan I.

Kata kunci: Titanium dioksida dop kuprum, aktiviti foto-pemangkinan, hetero-simpang, ko-dop.

ACKNOWLEDGEMENTS

First, I would like to express my sincere gratitude to my supervisors, Prof. Dr. Wan Jeffrey Basirun, Dr. Nor Asrina Sairi and Dr. Woi Pei Meng for their support, insightful guidance and encouragement during my research. Starting from their energetic discussions to stimulating ideas about research planning or results, they were successful to induce a high level of liveliness to their students. Working closely with them for almost three years, I learnt a lot about multi-tasking ability and time management.

My appreciation also goes to Prof. Dr. Yatimah Alias and Dr. Boon Tong Goh for the technical and financial support in part of my research.

Finally, a special thank you also goes to my lovely mom and dad for their unconditional support, patience, and love, without which I would not have been able to succeed. I thank you for being beside me through my entire life.

TABLE OF CONTENTS

LIST OF FIGURES

LIST OF TABLES

LIST OF SYMBOLS AND ABBREVIATIONS

λ	:	wavelength of radiation
BET	:	Brunauer-Emmett-Teller
CB	:	conduction band
e^-	:	electron
E_g	:	band gap
EDX	:	Energy Dispersive X-Ray Spectroscopy
EIS	:	Electro-chemical impedance spectroscopy
FESEM	:	Field emission scanning electron microscopy
g	:	gram
h^+	:	hole
ICP-MS	:	Inductively coupled plasma mass spectrometry
mL	:	milliliter
MO	:	methyl orange
NP	:	nanoparticle
$O_2^{\bullet-}$	:	superoxide radical
$^{\bullet}OH$	:	hydroxyl radical
$^{\bullet}OOH$	:	hydroxyl radical
PL	:	Photoluminescence spectroscopy
TEM	:	Transmission Electron Microscopy
UV	:	Ultraviolet
UV-Vis	:	Ultraviolet Visible
VB	:	valance band
XPS	:	X-ray photoelectron spectroscopy
XRD	:	X-Ray Diffraction

CHAPTER 1: INTRODUCTION

1.1 Background and motivation

Water scarcity is a serious global challenge as the available sources of drinking water are diminishing due to water pollution, population increase, and economic growth (Blomquist et al., 2012; Kesieme et al., 2013; Shahzad et al., 2017). Globally it is estimated that about 1.2 billion people are without access to clean drinking water, 2.6 billion people have poor or inadequate sanitation, and millions people die each year from diseases as a result of unsafe drinking water (Chong at al., 2010; Gober et al., 2018; Khalid et al., 2018). Researchers estimate that about 3.9 billion people live in areas faced with water stress or scarcity (Flörke et al., 2018; Jensen & Wu, 2018).

In addition to this, poor water quality is becoming a global issue of concern in many parts of the world. Rapid industrial and urban development has led to sewage and waste disposal problems having toxic chemicals and harmful pathogens. Industrial wastewater is one of the major sources in water pollution in the environment (Han, & Lu, 2018). Industrial activities (e.g. food, textile, leather, pharmaceuticals, paper and painting) consume dyes and coloring materials for aesthetic and decorative purposes daily.

Nowadays, textile industries are well-known economic benefits in developing countries. The textile dyeing industry uses large volume of water for various steps and produces large amount of wastewater. Textile dyeing is estimated to cause about 17-20% of total industrial water pollution (Sureshkumar et al., 2018; Tahir et al., 2018). The effluents from textile processing industry wastewater consist of suspended and dissolved solids, dye stuff and other dyeing auxiliaries (Rajkumar & Kim, 2006). It is estimated that approximately 10-15% of dyes might be discharged in water streams during the dyeing processes (Murugesan et al., 2017).

Almost 72 toxic chemicals have been recognized in wastewater from textile coloring and treatment, 30 of which cannot be eliminated effectively (Kaur al. 2018). These dangers toxic chemicals contain heavy metals, dioxins, and formaldehyde have been classified as a known causes of cancer. In addition to their toxicity properties, dyes can reduce sunlight penetration into the water and hence inhibits the photosynthesis processes (Ananthashankar, 2013). The complex molecular structures of dyes make them fade resistant when exposed to light, water and many chemicals (Liu et al., 2018). Thus, color removal from effluents is a major environmental concern because of severe damage to the natural environment.

1.2 Problem statement

The various conventional methods for wastewater treatment include adsorption, oxidation using hydrogen peroxide, coagulation, aerobic and anaerobic biological processes adsorption treatment methods (Hsiao et al., 2006; Ncibi et al., 2007). However, these processes have significant disadvantages such as secondary pollution due to sludge generation, and high operational costs. Therefore, there is an urgent need for treating wastewater using modern technology to successfully address these complex obstacles in water treatment.

The recent studies have attempted to discover new processes for wastewater treatment that enhance pollutant removal through relatively low-cost modifications (Zhao et al., 2017). Nanotechnology applications for waste water research have gained global popularity. Developments in nanotechnology associated with the wastewater treatment reveals that the current problems in water purification process could be resolved through photocatalysis.

Photocatalytic degradation of wastewater using TiO_2 is a prospective environmental clean-up tool for dye pollution and eliminates the drawbacks associated with the

aforementioned conventional methods. The biocompatibility, chemical inertness, high photocatalytic activity and cost-effectiveness, make TiO_2 the benchmark of semiconductor photocatalysis (Liu, 2017; Mahmoodi & Arami, 2009). However, due to its wide band gap, TiO_2 is only activated by ultraviolet (UV) light (λ<387 nm). This limits its photocatalytic reaction in visible light. It is known that UV radiation constitutes only 5% of the total solar energy while visible light consists of 42.3%. Thus, the visible light activated photocatalysts material is necessary for utilizing the full potential of sun-light as a safe, inexpensive and abundant degradation process. Therefore, it has a great importance to adjust the band structure of photocatalyst to effectively improve its photocatalytic activity by efficient use of solar energy.

1.3 Justification

Photocatalytsis has been intensively studied since the discovery of photocatalytic water splitting phenomenon using a TiO_2 electrode in 1972 by Fujishima-Hond (1972). Photocatalysis studies showed that irradiated semiconductors particles could effectively catalyze a wide range of organic and inorganic pollutants in the reduction-oxidation reactions (Fujishima et al., 2007). Many semiconductor nanoparticles with different photocatalytic properties have been investigated (Fujishima et al., 2007). Photocatalytic degradation of organic pollutants in water by semiconductor photocatalyst materials has attracted wide attention due to their effectiveness has been proved by many research papers (Fujishima et al., 2007; Heinlaan et al., 2008).

In contrast to other traditional remediation approaches for environmental cleaning, photocatalysis includes the decomposition of the pollutants from complex molecules into simpler and non-hazardous molecules. Therefore, no residue is produced and no sludge is formed in the process. Moreover, the secondary treatment is not required to process the sludge. In addition, the catalyst remains unchanged itself at the end of the

reaction and is thus reusable; consequently no consumable chemical is required. All the above benefits result in notable reduction of operating expenses. Thus, semiconductor photocatalysis provide an affordable and effective solution to wastewater treatment.

Among the various semiconductors employed, TiO_2 has known to be a promising photocatalyst because of its outstanding properties including chemical stability, strong oxidizing activity, corrosion resistance, low cost, nontoxity as well as high photocatalytic activity (Joshi et al., 2009). Numerous studies have found that nano-sized TiO_2 is an effective semiconductor photocatalyst in the degradation of different kinds of organic pollutants such as dyes (Agorku et al., 2014; Binas et al., 2017; Lee et al., 2018; Zahoor et al., 2018). Nevertheless, the wide electronic band gap (e.g., 3.0 and 3.2 eV for rutile and anatase), limits its photocatalytic activity under visible light irradiation.

The photon energy used for electron excitation in a semiconductor to degrade organic compounds in aqueous solution is the major source of expenses during photocatalytic purification and treatment of water (Ibhadon & Fitzpatrick, 2013). The most important limitations for photocatalysis application with semiconductors are their wide optical bandgap and ultraviolet activity (He et al., 2017; Ibhadon & Fitzpatrick, 2013). Improvement of the photocatalytic applications has required the use of sunlight or visible light responsive systems, which can make the process of their application efficient and inexpensive.

Tailoring the TiO_2 crystal structure to improve charge separation and extend its light response into the visible light region is an active area of research. These modifications are aimed at narrowing the band gap of TiO_2 or introduce impurity states within the band gap which can facilitate visible light absorption. Doping TiO_2 with metal ions (transition metals, rare earth metals and noble metals), nonmetals (N, S, B, C, P and halogens), co-doping (metal+metal, metal+nonmetal and nonmetal+nonmetal),

multidoping, coupling TiO_2 with other semiconductors to form heterojunction nanocomposites are some of the strategies investigated to improve the photocatalytic properties of TiO_2 under visible light irradiation. In this thesis, metallic doping, hetero-junction formation and metal/nonmetal co-doping techniques were explored.

Doping with metal or nonmetal ions serves as an effective method in the modifications of TiO_2 since this method not only preserve the crystal structure or the integrity of the host photocatalyst, but also identify desirable changes in the electronic structure (Zhang et al., 2018). To date, theoretical and experimental works have been devoted to the study of 3d transition-metal (TM) doped TiO_2 (Aljawfi et al., 2018; Wang et al., 2018). According the theoretical based research, 3d TM dopants can induce the formation of new states close to the valence band or conduction band. This produces significant band gap narrowing along with higher optical absorption (Shao, 2008). Nevertheless, many reports in the literature specify that the 3d TM dopants loading levels could play a key role on the photocatlytic activity of metal-doped TiO_2. Higher amount of dopants act as recombination centers (Dong et al., 2015), thus resulting in the limited enhancement of photocatalytic performance or even lower than pure TiO_2 (Dong et al., 2015; Liu et al., 2012). But, the effect of red shift by low content of these dopants is not obvious. Hence, extending the light absorption spectra to the visible along with the inhibition of the electron–hole pair recombination has been challenging.

Coupling two semiconductors materials to form a heterojunction has been recognized to be a viable approach to address the above challenges (Li et al., 2018; Liu et al., 2018). Heterojunctions between two semiconductors significantly suppress the recombination of photogenerated charge carries and also extends the solar light-response range, leading to substantial enhancement of solar photocatalytic efficiency (Guo et al., 2018; Yua et al., 2014).

Recent efforts and research reveal that doped semiconductors with a metal and nonmetal could result in the improvement of a highly effective visible light-active photocatalyst. Doping transition metal ions with nonmetals has become a popular research area. For example co-doping a transition metal with N, C, S or I could enhance the spectral response, charge separation and the overall photocatalytic activity compared to the mono- and pure TiO_2 through the combined effect of a metal and a nonmetal oxide semiconductor (Li et al., 2017; Li et al., 2011; Reisi et al., 2010; Song et al., 2011). Hence, the improved photocatalytic performance of co-element doped photocatalyst could be ascribed to the synergic effect of the dopants.

1.4 Aim and objectives

The main goal of this research is to improve of the photocatalytic activity of copper doped TiO_2 under visible light irradiation by either heterostructure formation with ZnO or nonmetal co-doping with I and evaluate their photocatalytic performance using methyl orang dye. Therefore, the following objectives were formulated:

1. To synthesize, characterize and optimize a variety of Cu-doped TiO_2 coupled with ZnO nanoparticles (Cu-TiO_2/ZnO) as photocatalyst by sol-gel method and subsequent precipitation.
2. To synthesize and characterize a variety of Cu-I-co-doped TiO_2 nano-particles as photocatalyst in different temperatures by the hydrothermal method.
3. To utilize the prepared Cu-TiO_2/ZnO photocatalyst and Cu-I-co-doped photocatalyst for the degradation of methyl orange under visible-light irradiation.

1.5 Thesis outline

The following outline provides a brief overview of the contents of the thesis:

Chapter 1 introduces the study undertaken in terms of the problem that it sought to address and the justification of undertaking this study. The objectives of the thesis are also presented in this chapter.

Chapter 2 includes a brief overview of the fundamentals of photocatalytic processes, in particular TiO_2, synthetic methods, and strategies for manipulating pure TiO_2 in order to improve its visible light photocatalytic.

Chapter 3 gives a brief description of the synthesis method employed to prepare the different photocatalysts in two projects as follows;

1. Enhanced visible light photocatalytic activity of copper-doped titanium oxide–zinc oxide heterojunction for methyl orange degradation.
2. Improved visible light photocatalytic activity of TiO_2 co-doped with copper and iodine.

A brief description about different characterization tools utilized during this research is presented in this chapter. Materials and reagents utilized for the preparation of the photocatalysts are also listed in this chapter. The procedure for evaluation of the photocatalytic properties of the prepared photocatalysts is presented in this chapter.

Chapter 4 presents the results and discussion for each project. The first part explores the effect of ZnO nanoparticles coupled with Cu-doped TiO_2. The effect of ZnO coupling with Cu-doped TiO_2 on bandgap and photocatalytic performance is discussed. The second part describes the effect of I co-doped in Cu-doped TiO_2 photocatalysts. The synergistic effect of I and Cu on bandgap reduction and photocatalytic activity in the

visible region is discussed. The photocatalytic performances of the both novel photocatalysts toward MO dye under visible light were determined. Finally, a possible photocatalytic degradation mechanism is proposed for each prepared photocatalyst in this chapter.

Chapter 5 provides some general conclusions and highlights some recommendations on possible future studies on different aspects of this work.

CHAPTER 2: LITERATURE REVIEW

This chapter begins with a detailed discussion of TiO_2 as the semiconductor photocatalyst. A brief discussion on the methods for modifying TiO_2 for improved visible light photocatalytic activity, are also presented in this chapter.

2.1 Titanium dioxide (TiO_2)

Titanium dioxide (TiO_2) is known as *n*-type semiconductor, and is the most researched semiconductor photocatalyst because of its high photocatalytic activity, low cost, non-toxicity and good chemical and thermal stability (Wang et al., 2009). There have been several great-leap-forward developments with respect to TiO_2 in the past few decades. The first significant breakthrough was by Fujishima and Honda (1972), who discovered the ability of TiO_2 electrode to split H_2O molecules into H_2 and O_2 under ultraviolet (UV) radiation (Fujishima & Honda, 1972). The TiO_2 photocatalyst was first applied for environmental purification in 1977 when Frank and Bard (1977) examined the decomposition cyanide in water. Thus, these areas have received dramatic attention from researchers due to the great potential for water and air purifications through the use of "free" and "renewable" solar energy (Hoffman et al., 1995). Other major advance involved the work of Wang et al. (1998), reported that TiO_2 surface possesses good self-cleaning performance and excellent anti-fogging ability. In addition, efficient dye-sensitized solar cell (DSSC) constructed with nano TiO_2 was reported by O'Regan and Graetzel in 1991 (O'Regan & Gratzel, 1991).

TiO_2 exists mainly in three known crystalline phases: anatase, rutile and brookite (Nolan et al., 2009). Generally, rutile is the best thermodynamically stable and common natural form of TiO_2 at high-temperature and high-pressure. Typically the metastable anatase and brookite forms of TiO_2 will transform to the stable rutile form upon calcination at high temperature (Hu et al., 2003). Among these TiO_2 phases, anatase and

rutile are the most studied phases for photocatalytic applications (Leung et al., 2010). Bookite has a major drawback in photocatalytic application because of the difficulties in synthesis due to its metastable character and is generally photocatalytically inactive (Zhao et al., 2013). The crystal structure of anatase and rutile can be described of terms of the TiO_6 octahedral chains. However, the two crystal structures are different in distortion and assembly patterns of the octahedral (Figure 2.1) (Nicholls, 1974).

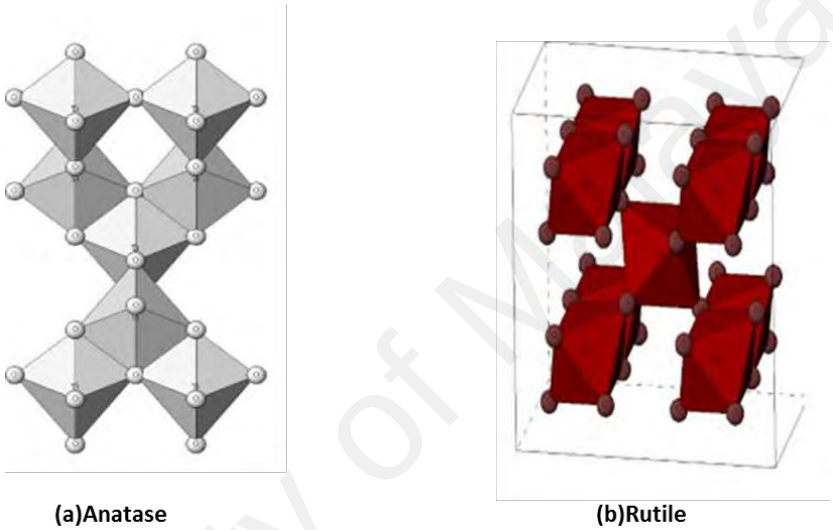

Figure 2.1: Crystal structures of anatase and rutile. Adapted and reproduced with the permission of ref. (Pelaez et al., 2012) copyright Elsevier.

The anatase TiO_2 is considered more photocatalytically active phase compared with the rutile phase (Liu et al., 2009), mostly because of fast electron–hole recombination in rutile (Zhao et al., 2013).

Nevertheless, mixtures of anatase–rutile such as Degussa P-25 (approximately 75% anatase and 25% rutile) exhibited a higher photocatalytic activity than that of each of the single-phase anatase or rutile (Luo et al., 2015). The enhanced photoactivity has been attributed to the interfacial properties between the different polymorphs. Bickley et al. (1991) demonstrated that the existence of an intimate contact between anatase and

rutile particles are essential to attain an improvement from the mixed phase. The anatase and rutile difference band gap values (3.2 eV and 3.0 eV, respectively), result in formation of a heterojunction between the two phases (Jing et al., 2008). Therefore, the anatase-rutile phase junction effectively facilitates the photoinduced charge separation. Based on the energy band alignment between the anatase and rutile, the conduction band (CB) edge position of rutile is higher than that of anatase, which provides a favorable condition for electron transfer from rutile to anatase (Zhao et al., 2013).

The change between the proportions of anatase-rutile phases has shown different level of enhancement in the mixed-phase TiO_2. According the Liu et al. (2016), an optimal amount of rutile TiO_2 for mixed phase TiO_2 can be varied over a large range (from < 10% up to > 70%), depending on the preparation method and reaction conditions.

2.2 Basic principles of TiO_2 photocatalysis

Photocatalysis is usually defined as the acceleration of a photoreaction process when a semiconductor material, interacts with the sufficient light wavelength to produce several active species which can facilitate the reaction.

In photocatalysis, photons with energy higher than the band gap energy of the semiconductor is absorbed, and excites the valence band (VB) electrons (e^-) to the higher energy conduction band (CB) simultaneously forming holes (h^+) in the VB. Figure 2.2 depicts the mechanism of the ($e^- - h^+$) pairs formation when the TiO_2 particle is irradiated with light of adequate energy. For anatase TiO_2, the UV light with $\lambda \leq 387$ nm is required due to a wide band gap (3.2 eV) (Equation 2.1).

$$TiO_2 + h\nu \rightarrow e^- + h^+ \qquad \text{(Equation 2.1)}$$

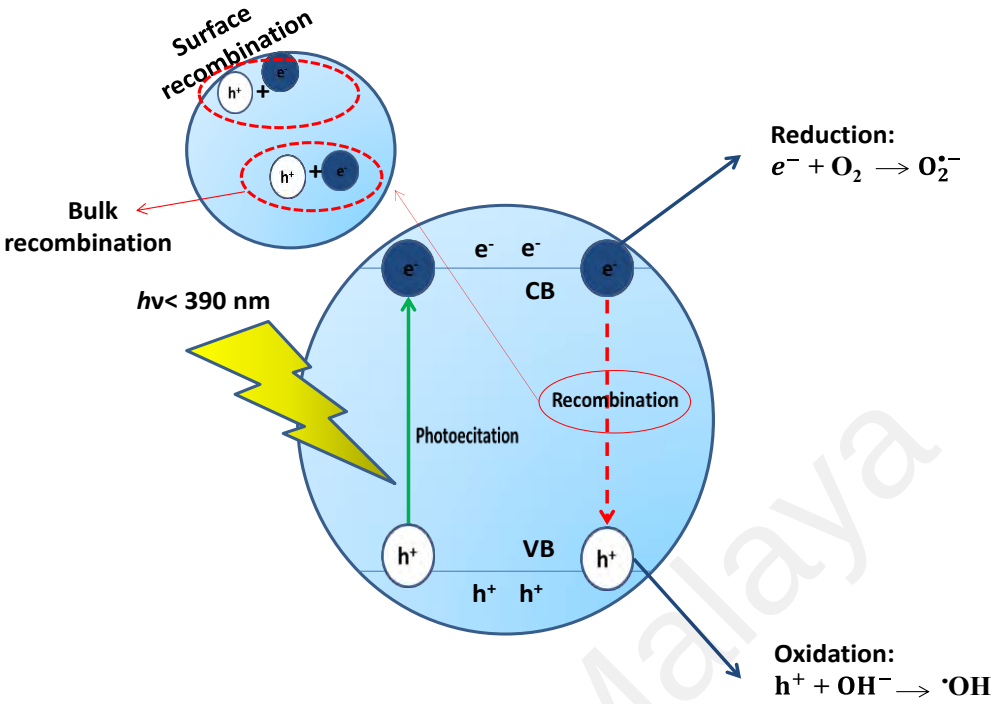

Figure 2.2: Schematic of TiO_2 photocatalytic mechanism**.**

The photogenerated $(e^- - h^+)$ pairs can migrate to the catalyst surface and participate in redox reactions (Cozzoli et al., 2003). Photogenerated h^+ can oxidize the absorbed substrate hydroxide ions (OH^-) or water (H_2O) to produce hydroxyl radicals ($^{\bullet}OH$) (Equations. 2.2 and 2.3). The $^{\bullet}OH$ radicals are the primary and powerful oxidants that promote the photocatalytic mineralization of organic pollutants in the aqueous solution (Table 2.1) (Hoffman et al., 1994).

$$h^+ + OH^- \rightarrow \cdot OH \qquad \text{(Equation 2.2)}$$

$$h^+ + H_2O \rightarrow \cdot OH + H^+ \qquad \text{(Equation 2.3)}$$

Table 2.1: Standard electrochemical reduction potentials of common oxidants. Adapted and reproduced with the permission of ref. (Pelaez et al., 2012) copyright Elsevier.

Oxidant	Half-cell reaction	Oxidation potential (V)
$^{\bullet}OH$ (Hydroxyl radical)	$^{\bullet}OH + H^+ + e^- \rightarrow H_2O$ (aq)	2.80
O_3 (Ozone)	O_3 (g) + $2H^+$ + $2e^- \rightarrow$ O_2 (g) + H_2O (aq)	2.07
H_2O_2 (Hydrogen peroxide)	H_2O_2 (g)+ $2H^+$ + $2e^- \rightarrow$ $2H_2O$ (aq)	1.77
Cl^- (Chlorine)	Cl_2 (g) + $2e^- \rightarrow 2Cl^-$	1.49
HClO (Hypochlorous acid)	$2HClO + 2H^+ + 2e^- \rightarrow Cl_2 + 2H_2O$ (aq)	1.36

Meanwhile, the dissolved oxygen molecules presented in the solution can be reduced by the excitation of e^- in the CB to form superoxide radicals ($O_2^{\bullet -}$) (Equation 2.4).

$$e^- + O_2 \rightarrow O_2^{\cdot -} \quad \text{(Equation 2.4)}$$

This $O_2^{\bullet -}$ radicals may further protonate to generate the hydroperoxyl radical ($^{\bullet}OOH$) and subsequently produce hydrogen peroxide (H_2O_2) as shown in equations 2.5 and 2.6 (Pelaez et al., 2012). The H_2O_2 produced can also absorb photons to produce even more $^{\bullet}OH$ radicals directly (Equation 2.7).

$$O_2^{\cdot -} + H^+ \rightarrow OOH^{\cdot} \quad \text{(Equation 2.5)}$$

$$OOH^{\cdot} + OOH^{\cdot} \rightarrow H_2O_2 \quad \text{(Equation 2.6)}$$

$$H_2O_2 + h\nu \rightarrow OH^{\cdot} + OH^{\cdot} \quad \text{(Equation 2.7)}$$

These activated oxygen-containing radicals (e.g. $^{\bullet}OH$, $O_2^{\bullet -}$ and $^{\bullet}OOH$) contribute in the oxidization of organic species into non-harmful materials, such as CO_2 and H_2O (Equation 2.8). Furthermore, the photogenerated h^+ has been widely considered as a

powerful oxidant used for the degradation of organic contaminates in water (Dong et al., 2015).

$$(OH^{\cdot}, O_2^{\cdot -}, OOH^{\cdot} \; or \; h^+) + Pollutant \rightarrow Degradation \; products \quad \text{(Equation 2.8)}$$

2.3 Mechanism of hydroxyl radical attack on organic pollutants

During photocatalysis, both the superoxide and hydroxyl radicals are important and they complement each other (Nosaka & Nosaka, 2017). The superoxide radical can either oxidise the organic pollutants directly or undergo further reactions to form the hydroxyl radical as depicted in **Equation 2.7**. The degradation of organic compounds by the hydroxyl radical can proceed either through hydrogen abstraction, electrophilic attack or electron transfer. However, hydrogen abstraction has been highlighted as the most common route for degradation of organic compounds (Khan et al., 2017). During hydrogen abstraction, hydrogen is removed from the organic compound to form an organic radical as shown **in Equation 2.9**. Subsequent reaction with oxygen, transforms the organic radical to peroxyl radical. These peroxyl radicals undergo a series of thermal reactions of oxidative degradation, leading to the complete mineralisation of the organic compound to carbon dioxide, water and inorganic salts (**Equation 2.10**) (Miller et al., 2017). Electrophilic addition is another proposed mechanism whereby the hydroxyl radical is added to the organic compounds π-system to form the organic radical (**Equation 2.11**). In cases where hydrogen abstraction or electrophilic addition is unfavourable due to multiple halogen substitution or steric hindrance, electron transfer is a possible route for initiating degradation of the organic compound. The hydroxyl radical is reduced to hydroxide ions by the organic compound while forming the organic radical (**Equation 2.12**). Thereafter, the organic radical undergoes the transformations depicted in **Equation 2.10**. In addition to radical attack on organic compounds, direct reduction by the conduction band electrons (**Equation 2.13**) and oxidation by the

valence band holes (**Equation 2.14**) have been reported as other possible routes through which degradation of organic pollutants such as dyes is initiated during semiconductor photocatalysis (Huang et al., 2017).

$$OH^{\cdot} + RH \rightarrow R^{\cdot} + H_2O \quad \text{(Equation 2.9)}$$

$$R^{\cdot} + O_2 \rightarrow RO_2^{\cdot} \rightarrow CO_2 + H_2O + Inorganic\ ions \quad \text{(Equation 2.10)}$$

$$PhX + OH^{\cdot} \rightarrow HOPhX^{\cdot} \quad \text{(Equation 2.11)}$$

$$OH^{\cdot} + RX \rightarrow RX^{\cdot +} + OH^{-} \quad \text{(Equation 2.12)}$$

$$Dye + e_{CB}^{-} \rightarrow Dye^{-} \rightarrow Degradation\ products \quad \text{(Equation 2.13)}$$

$$Dye + h_{VB}^{+} \rightarrow Degardation\ products \quad \text{(Equation 2.14)}$$

2.4 Drawbacks of TiO_2 as a photocatalyst

Although TiO_2 has some advantages that make it an excellent photocatalyst, it has some serious limitations that hinder its full exploitation as an environmental clean-up tool for organic pollution especially dye-pollution. First, TiO_2 has a wide band gap (3.2 eV, anatase and 3.0 eV, rutile) which only allows absorption in the UV region. This poses a serious energy problem because UV light only accounts for about 4% of the solar spectrum which rules out the possibility of using sunlight as a source of energy. Visible light absorption would enable TiO_2 to harness sunlight as a source of energy owing to its approximately 40% abundance in the solar spectrum (Wang et al., 2008). Solar energy is a clean, natural energy which could replace the artificial UV sources which consume large electrical energy and require eyes and skin protection during application which ultimately lead to escalating costs (Epling & Lin, 2002).

The other major shortfall of TiO_2 is the fast recombination rate of the photogenerated electron-hole pairs. This limits the formation of the hydroxyl and superoxide radicals which are responsible for the photocatalytic degradation of the organic pollutants. Consequently, the efficiency of the photocatalytic process is remarkably lowered (Soutsas et al., 2010).

2.5 Preparation of TiO_2 by aqueous methods

When TiO_2 is prepared in aqueous medium, as in the case of most transition metal oxides, the Ti−O−Ti bond network is formed in two steps: hydrolysis and condensation (Cargnello et al., 2014). The hydrolysis step results in the formation of a metal complex with water in the form of aquo, hydroxo or oxo complexes, depending on the metal cation and the reaction conditions. Moreover, the condensation is the reaction between two (or more) of the formed complexes to give the Ti−O−Ti bonds, which are the precursors of the final oxide network.

The majority of syntheses are performed using either titanium tetrachloride or a form of titanium alkoxide, such as titanium isopropoxide, as the titanium precursor. However, the hydrolysis and condensation rates of these kinds of titanium precursor are usually fast, due to the sensitivity of these precursors to the moisture which leads to undesirable consequences such as the precipitation of particles with uncontrolled shapes and sizes. An oxy-carboxylate precursor, titanium (IV) bis (ammonium lactato) dihydroxide is shown schematically in Figure 2.3. Due to its solubility and stability in neutral aqueous mediums, which can be considered as an ideal precursor to obtain crystalline and dispersible titanium dioxide (Kessler, 2017).

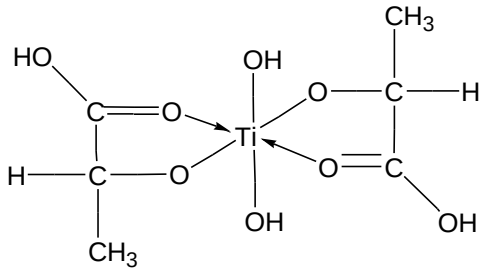

Figure 2.3: Titanium (IV) bis (ammonium lactato) dihydroxide structure.

2.5.1 Sol-gel

The process involves the transformation of a sol into a gel, which is then usually thermally treated to obtain the final material. Sol is a solution of precursor compound (either inorganic or metal−organic). Following a series of chemical reactions and/or thermal treatments, the precursor reacts to form a network of bonds, resulting in a solid skeleton of metal−oxygen bonds within a continuous liquid phase. At this point the structure is called a gel. Finally, thermal treatment is generally needed to transform the dried gel into the final desired material.

2.5.2 Precipitation

Precipitation is a reaction between cations and anions in solution which combines to form an insoluble solid salt, known as a precipitate. Precipitation can be controlled by the kinetics of the precipitation. Moreover, concentration of the reactants, ions and pH are the essential factors which determine the precipitation process and control the particle size (Burda et al., 2005).

2.5.3 Hydrothermal

Hydrothermal synthesis is a technique to exploit the solubility of inorganic material in water at high temperatures and pressures, and following crystallization of the dissolved material. Water at elevated temperatures has an effect on the precursor material transformation due to the increased vapor pressure. High temperature could

also change the solubility and reactivity of the reactant, which can produce different high quality nanoparticles and nanotubes. In the hydrothermal synthesis, water pressure, temperature, and reaction time can be controlled to maintain a high simultaneous nucleation rate and narrow particle size distribution (Burda et al., 2005).

2.6 Approaches to enhance the visible-light photocatalytic activity of TiO_2 particles

In order to enhance the photocatalytic efficiency of TiO_2, there is a need to overcome the drawbacks highlighted in **Section 2.3**. This means modifying TiO_2 with some promising technologies to extend its photo response into the visible light region and improve the charge separation. Techniques include doping with metal or nonmetal dopants, coupling and co-doping of TiO_2 with different elements. These modifications enable utilization of the abundant solar energy and improve the photocatalytic activity of TiO_2 which could pave way for effective environmental clean-up and protection.

2.6.1 Metal and nonmetal doping

The optical properties of TiO_2 can be improved through the addition of metal and nonmetal ion(s). The band gap properties of TiO_2 could be modified once metals or nonmetals dopants replace Ti in the substitutional sites, occupy in the interstitial sites or form nanoparticle aggregates on the surface of TiO_2 (Sahu & Biswas, 2017). In this thesis, doping is the process of introducing some impurity atoms into the crystal lattice of a semiconductor material (Neamen, 2012), which changes the physicochemical characteristics of the semiconductor. According to Pagot and Clerjaud (2012), the local lattice distortions could happen in substitutional and interstitial doping due to the atomic radius difference between doped impurity atoms and host atoms and their ability of interact with the surrounding atoms. These lattice defects can change the electric properties of host atoms by disruption of the covalent bonds between the atoms and

distortion of the geometric shape of atoms (Neamen, 2012). The introduction of dopants has been found to alter the degree of crystallinity and crystalline phase transformations, thus, subsequently changing in the peak intensities (Hanaor & Sorrell, 2011). Anatase-rutile phase transformation can be promoted or restricted by introduction of dopant ions into anatase lattice which cause an increase or decrease in the oxygen vacancies level. This results in the consequent rearrangement of atoms in the lattice structure of TiO_2 through the substitution of Ti^{4+} site by doping ions consequently facilitating or inhabiting the phase transformation to rutile.

2.6.1.1 Metal doping TiO_2

Transition metal, noble metal and rare earth metal ions are the most extensively used dopants to modify the TiO_2 to extend the response into the visible light region and improve the charge separation. It was reported that metal ion doping could influence interfacial the electron transfer rates, photogenerated ($e^- - h^+$) recombination, light response, and considerably influence the photocatalytic performance of TiO_2.

Once metal ions are introduced into the TiO_2 crystal lattice, the impurity energy levels are produced in the band gap of TiO_2 ((2.9) and (2.10)) (Ola & Maroto-Valer, 2015).

$$M^{n+} + h\nu \rightarrow M^{(n+1)+} + e_{CB}^- \quad \text{(Equation 2.9)}$$

$$M^{n+} + h\nu \rightarrow M^{(n-1)+} + h_{VB}^+ \quad \text{(Equation 2.10)}$$

where M is metal and M^{n+} is the metal ion dopant. Moreover, transfer of charge (electron/hole) between TiO_2 and metal ions can alter the recombination of electron/hole pairs rate through the following processes:

$M^{n+} + e_{CB}^{-} \rightarrow M^{(n-1)+}$ as electron trap (Equation 2.11)

$M^{n+} + h_{VB}^{+} \rightarrow M^{(n+1)+}$ as hole trap (Equation 2.12)

Photoactivity of metal ion-doped TiO_2 is a complex function of the dopants' nature and amount, and the preparation procedure etc (Soria et al., 1991). It has also been reported that even the method of doping such as hydrothermal, impregnation, sole-gel and co-precipitation methods have led to change in the morphological and crystalline properties of the photocatalytic activities of semiconductors (Zaleska, 2008).

(a) ***Doped TiO_2 with transition metals***

Numerous studies have been reported from transition metals doped TiO_2 such as Fe (Ambrus et al., 2008), Co (Subramanian et al., 2008), Ni (Correa, 2006), Mn (Mohamed et al., 2007), V (Tsuyumoto & Nawa, 2008), Cu (Dorraj et al., 2017), Zn (Wang et al., 1997) and etc. Transition metal ions doping of TiO_2 has been found to contribute positively to the photocatalytic activity, due to shifting in the absorption region from UV to visible light caused by a change in the electronic structure (Zhang & Zeng, 2011). The red shift of absorption edge to the visible light region can be assigned to the charge transfer between the d electrons of the transition metals and the TiO_2 conduction or the valence band (Teh & Mohamed, 2011). George et al. (2011) found that Fe-doped TiO_2 nanoparticles prepared from a versatile and reproducible flame spray pyrolysis technique could tune the band gap energy by introducing trap levels between the valence and conduction bands of TiO_2 to study the oxidation of biomolecules in the near-visible wavelength conditions (Figure 2.4).

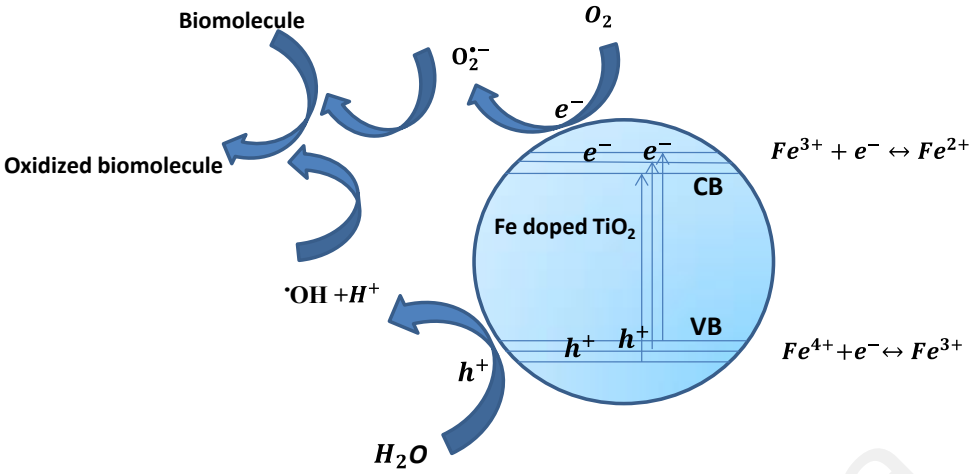

Figure 2.4: Mechanisms of Fe-doped TiO_2 nanoparticles for oxidation of biomolecules under visible light.

Hsieh et al. (2009) reported that an obvious peak appears between 550–650 nm after doping TiO_2 with Co , which the author theorized, were due to the creation of additional energy levels within the band gap. Kerkez et al. (2015) prepared cation-doped TiO_2 photocatalyst by adding various transition metals such as Fe, Cu, Ni, Co, Mn and Cr and found that the transition metals could increase the visible light absorption of the catalyst while Ola et al. (2015) also observed that the visible light absorption shifts to the longer wavelengths (red shift) with increasing metal (V, Cr and Co) concentration doped on the TiO_2 photocatalyst. Both studies concluded that the enhanced absorption observed for the transition metal doped TiO_2 in the visible region might be due to the electron transfer from the 3d orbitals of the metal ions to the TiO_2 CB. Moreover, Ola et al. (2015) also reported that the optical properties of V doped TiO_2 were modified to the visible light due to the substitution of the Ti^{4+} by V^{4+} or V^{5+} ions since the V^{4+} is centered at 770 nm while the absorption band of V^{5+} is lower than 570 nm. Both results showed that the band gap of TiO_2 is significantly decreased after the metal doping.

Besides, transition metal ions into the TiO_2 lattice could function as photogenerated holes and electrons traps, which retars the recombination rate of electrons and holes,

thus enhancing the photocatalytic activity of TiO_2 (Kment et al., 2010). Tieng et al. (2011) reported that Fe^{3+} ions could be trapping sites for both photogenerated electrons in the conduction band and holes in the valence band. Consequently, the photogenerated charge carriers could be separated more easily and protected for a longer time. As a result, adsorbed species redox reaction occurs more efficiently.

Cu is also an important dopant with high abundance and relatively lower cost (Cao et al., 2011). Cu incorporated photocatalysts have been proved to be active and widely applied in the reduction of NO to N_2 (Aritani et al., 1997), reduction of CO_2 to methanol (Bando et al., 1997; Yamashita et al., 1994), complete oxidation of CO (Larsson et al., 1998), and oxidation of organic pollutants, such as, toluene, ethanol, ethyl acetate (Larsson et al., 1998), phenol (Colon et al., 2006; Kim et al., 2007) and cyanide (Chiang et al., 2002). All chemical states of Cu ($Cu/Cu_2O/CuO$) have been studied for the enhancement of photodegradation of organic pollutants.

Lo´pez et al. (2009) reported enhanced TiO_2 photocatalysis by Cu for the degradation of 2,4- dichlorophenoxyacetic acid. The chemical state of Cu doped TiO_2 lattice in their study was metallic Cu and Cu^+ which occurred by the reduction of Cu^{2+}. Colo´n et al. (2006) revealed that Cu_2O species at the TiO_2 surface was able to increase the photocatalytic oxidation of phenol under visible light irradiation. They indicated that copper ions in the form of Cu^+ promote good dispersion into the TiO_2 matrix, stabilized by the presence of oxygen vacancies, which consequently gave a higher photocatalytic activity for degrading phenol. More common than metallic Cu and Cu^+, the divalent Cu^{2+} is also reported both in substitutional sites and in CuO clusters form as well. Li et al. (2008) discovered the attendance of both substitutional Cu^{2+} sites and highly dispersed CuO clusters participated to the enhanced photooxidative activity of the coupled $CuO\text{-}TiO_2$ nanocomposite for the methylene blue degradation under visible

light. They also found that the optimum CuO loading was 0.1 wt %, and at higher copper loadings, the bulk form of CuO produced recombination centers that decrease in photocatalytic activity of the composites. Xia's group (2008) also studied the degradation of aqueous brilliant red X-3B solution over Cu^{2+} doped rutile TiO_2 photocatalyst. In their study, the copper concentration influences the photocatalytic activity of TiO_2 as well as the structure. They reported that the photo-catalytic activity was remarkably enhanced by 2% Cu^{2+} doped TiO_2 compared to the pure TiO_2. Their results confirm that the embedding of some portion of copper into TiO_2 particle inhibits the growth of rutile crystal of TiO_2 particles.

Photocatalytic performance of the Cu-TiO_2 is strongly related to the preparation method, preparation procedure, chemical property and Cu content etc. In the above discussions, we have mentioned the different photocatalytic activity of "loaded" and "doped" Cu-TiO_2. Boccuzzi et al. (1997) compared the characteristics of Cu-TiO_2 prepared by wet impregnation and chemisorptions-hydrolysis, and found that the samples with same chemical compositions had very different properties: different behaviors under electron beam, different peak positions and widths in temperature programmed reduction (TRP) profiles, and different FTIR data. Tseng et al. (2004) reported three factors such as copper precursor type, adding time with sol and post-treatment processes which heavily affect the characteristics and activity of the Cu-TiO_2 photocatalyst prepared by modified sol-gel process. They revealed that Cu-TiO_2 prepared from $CuCl_2$ added in the early stage of the sol-gel process was more photoactive than that fabricated from copper acetate since $CuCl_2$ precursor increased the Cu dispersion. They also found that additional post-treatments before the photocatalytic reaction decreased the yield due to change in Cu dispersion and oxidation state. In addition, for higher photocatalyst degradation activity, both Li and Xia reported the presence of optimum Cu content in separate studies.

Recently, a theoretical study of copper doped TiO_2 shows that copper dopant at anatase surface is most stable in the 2+ oxidation state whereas the formation of secondary CuO phases is strongly unfavorable (Assadi & Hanaor, 2016). Biswajit and his co-workers (2013) concluded that the Cu^{2+} *d* states and oxygen defects are responsible for the effective reduction of TiO_2 band gap. Their study explained that the larger size Cu^{2+} (0.72 Å) replaces the Ti^{4+} (0.68 Å), and hence, this feature causes the lattice distortions. The charge difference between the Cu^{2+} and Ti^{4+} may produce oxygen vacancies to maintain the local charge balance in the lattice of TiO_2, which distorts the local symmetry of the TiO_6 octahedral and changes the geometrical structure from octahedral to tetragonal (Figure 2.5). Cu^{2+} has a d^9 electronic configuration and the single electron in the *d* orbital undergoes Jahn-Teller geometrical distortion which could easily contribute to a broad absorption band in the visible region. However, this charge transfer cannot tack place in the Cu^{+} or Cu^{0} because of the fully–filled 3d shell.

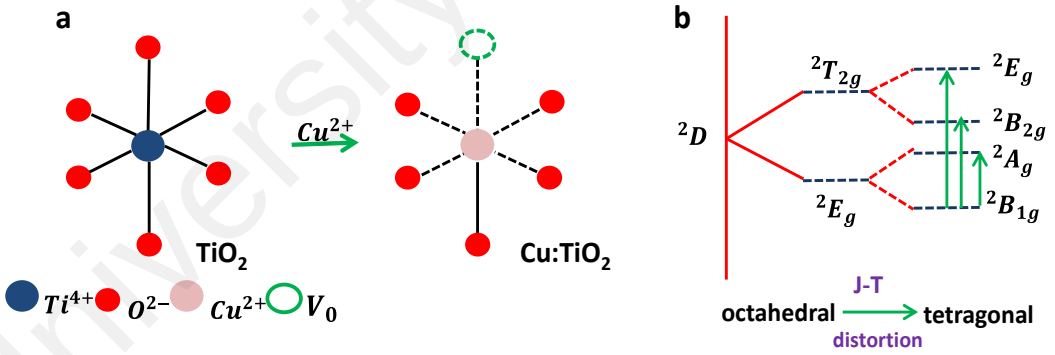

Figure 2.5: Distortion of the TiO_6 octahedral. (a) Schematic representation of the distortion of the TiO_6 octahedral on doping Cu^{2+} ion on the Ti^{4+} lattice site. Doping of Cu^{2+} on Ti^{4+} generates oxygen vacancies (white ball) nearby Cu^{2+} (shown by a dashed line). (b) Jahn-Teller (J-T) distortion of the octahedral symmetry of TiO_6 and changes in the *d-d* transition from octahedral to tetragonal.

Recently , Jaiswal et al. (2015) also reported that Cu^{2+} doped TiO_2 is able to narrow the band gap significantly due to localization of Cu 3d levels above the valance band maximum (VBM) and shifting of the conduction band minimum (CBM) towards lower

energy (due to presence of oxygen vacancies) in the band-gap. In addition, Cu^{2+} ions can trap not only holes but also electrons. According the theoretical calculation study by Dashora et al (2014), the energy levels formed by Cu^{2+} species can act as hole trapping sites while the oxygen vacancies or defects assist in capturing electrons thus promoting an efficient separation of the photogenerated charges.

(b) ***Doped TiO_2 with noble metal and rare earth metal***

Nobel metals such as platinum (Pt), palladium (Pd), silver (Ag), and gold (Au) ions also facilitate visible light absorption of TiO_2 semiconductor (Grabowska et al., 2010). Dozzi et al. (2012) investigated the effect of noble metal (Pt and Au)-doped TiO_2 photocatalyst for the formic acid degradation. Kisch et al. (1998) also studied the photocatalytic degradation of 4-chlorophenol by TiO_2 modified with platinum (IV)-chloride complexes under visible light. The noble metals decorated on TiO_2 surface can facilitate the photogenerated charge carriers separation, and subsequently enhances the photocatalytic performances of the surface and bulk modified photocatalyst systems. According to Yoon (2009), the surface of noble metal functions as sensitizers to improve the visible light absorption and centers of charge separation.

Rare earth metals such as yttrium (Y), scandium (Sc), and the 15 lanthanoids, are a group of 17 chemical elements in the Periodic Table. According to Stengl et al. TiO_2 doped with rare earth such as La^{3+}, Ce^{3+}, Ce^{4+}, Eu^{3+}, Gd^{3+} and Sm^{3+} resulted in the strong absorption edge shift towards longer wavelength (Štengl et al., 2009). This was ascribed to the electronic transitions between the rare earth ions and the conduction or valence band of TiO_2. Moreover, visible light absorption due to the f-f electronic transitions was observed in the Nd^{3+}, Pr^{3+} and Dy^{3+} doped TiO_2. Drastic reduction in the band gap of TiO_2 has been reported by Nd and Yb doped TiO_2 due to the presence of new 4f states present in the TiO_2 band gap (Bingham & Daoud, 2011).

2.6.1.2 Nonmetal doping TiO_2

In recent years, increased efforts have been directed toward improving the photocatalytic efficiency of semiconductor under visible light via the doping of nonmetal ions in order to narrow the band gap. The previous research by Wang et al. (2011) has shown that C–N–S doped TiO_2 nanoparticles extended absorbance in the visible-light for tetracycline degradation. Studies also showed that the band gap narrowing of TiO_2 can be reached using C ion (Ren et al., 2007). The modified TiO_2 displayed stronger visible light absorption due to the narrow band gap result in enhanced photocatalytic degradation of organic pollutants in the visible region. It is found that the nonmetal doping TiO_2 can narrow the catalyst band edges by the hybridization between the O *2p* and nonmetal orbitals, because their energy states are very close. Daghrir et al. (2013) suggested that the band gap narrowing due to the N doping into TiO_2 lattice can be attributed to the orbital overlapping between the N *2p* and O *2p* orbitals (Figure 2.6). This generates an impurity levels in the TiO_2 lattice, which leads to enhanced performance for photocatalytic activity compared with that of bare TiO_2 under visible light.

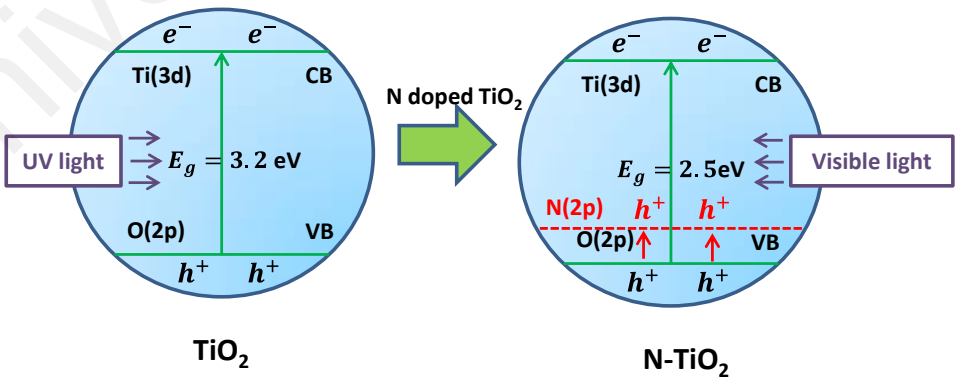

Figure 2.6: Schematic energy level of nitrogen doping TiO_2.

Several studies have indicated that iodine doping in TiO_2 can shift the optical absorption spectra to 500−700 nm from 400 nm for the bare TiO_2 and consequently broadening its application range.

Iodine doped titanium dioxide have been studied from both an experimental and theoretical perspective (Bagwasi et al., 2012; Long et al., 2009; Shi & Weng, 2008). A review of the above cited literature shows that the iodine ions can exist in a number of different oxidation states and therefore incompatible results are found from different authors on how iodine exists in TiO_2 structure. Some experiments confirmed that I^{5+} could substitute Ti^{4+} due to close ionic radius of I^{5+} (6.2 Å) and Ti^{4+} (6.4 Å). Long et al. (2009) applied density functional theory to analyze the electronic structure of I doped into TiO_2 lattice structure. They found that the I 5*p* orbitals of iodine could mix with the O 2*p* in the valence band and Ti 3d orbitals in the conduction bands, which enhance the visible light absorption. In addition, Li et al. (Li et al., 2014) suggested that I^{5+} can be an electron acceptor during the reduction to the lower multi valance states close to the CB, resulting in an efficient separation of photo induced charge carriers. Liu et al. (2009) argued using theoretical computation that I^{5+} ions preferred to be doped close to the surface of TiO_2, facilitating the electron transfer process to the surface of TiO_2.

Some authors pointed out that I ion can be existed on the surface of TiO_2 owing to its large ionic radius compared to both Ti^{4+} and O^{2-}. Su et al. proposed that the I^{7+}/I^- species are well dispersed on the anatase particle surface and not through crystal lattice substitution (Su et al., 2008).

2.6.2 Drawbacks of metals doping of TiO_2

As discussed in the previous section, the doping of TiO_2 with metallic ions has offered good effects on photocatalytic performance. Nevertheless, several authors have pointed out some drawbacks associated with metal doping (Crişan et al., 2015; Demirci

et al., 2016; Jiang et al., 2015; Moradi et al., 2016). Photocatalytic activity of metal-doped TiO_2 is found to be influenced by concentration of the dopant. In general, optimum dopant concentration could improve the photocatlytic performance. Nonetheless, some researchers reported that more than the optimal value of doping ions, the photodegradation rate decreased. It was concluded that the dopant ion concentration below its optimum dosage level can serve as electron−hole separation centers, and therefore enhance the photocatalytic efficiency, whereas the dopant ions with excessive dosage levels could function as electron−hole recombination centers which cause the detrimental effect in photocatalytic activity (Dong et al., 2015). Table 2.2 shows an optimum concentration of several metal dopants which enhances the photocalytic degradation.

Table 2.2: Optimum metal dopants concentration used for improved efficiency of catalyst.

Photocatalyst	Range of doping	Optimum doping	Light source	Pollutant	References
Transition Metals					
Fe-doped TiO_2	0.5, 1, 2 and 5 wt%	0.5 wt%	UV	nitrobenzene	(Crişan et al., 2015)
Fe-doped TiO_2	0.1, 1, 5 and 10 wt%	1 wt%	visible light	reactive red 198	(Moradi et al., 2016)
Fe-doped TiO_2	1,1.5 and 2 wt%	1.5 wt%	UV	diazinon	(Tabasideh et al., 2017)
Fe-doped TiO_2	0.25, 0.5, 1, 5 and 10 mol%	0.5 mol%	visible light	methyl orange	(Moradi et al., 2018)
Cu-doped TiO_2	0.5, 1, 3, 5 and 10 mol%	0.5	UV	methyl orange	(Wu et al., 2018)
V-doped TiO_2	0.1%, 0.25%, 0.5%,0.75%, 1.0%,1.25%, 1.5%, 2.0%,and 5.0% at%	1 at%	visible light	RhB	(Lu et al., 2015)
Co-doped TiO_2	0.1 %–3 at.%	3 at%	visible light	phenol	(Jiang et al., 2015)
Mn-doped TiO_2	0.02%, 0.05%, 0.2% and 0.5% wt%	0.05 wt%	visible light	Cr(VI)	(Chen et al., 2016)
Noble Metals					
Ag-doped TiO_2	0.1%, 0.3%, 0.5%, 0.7% and 0.9% mol%	0.7 mol%	UV	methylene blue	(Demirci et al., 2016)
Ag-doped TiO_2	3.5–0.75 at.%	0.75 at %	UV	phthalic acid	(Mogal et al., 2014)
Rare Earth Metals					
Gd-doped TiO_2	0–0.6 at.%	0.3–0.4 at.%	UV	methyl orange	(Cheng et al., 2016)
Gd-doped TiO_2	0.9, 1.8 and 3.6 at.%	1.8 at.%	UV	Methylene blue	(Farbod & Kajbafvala, 2013)

Besides, metal doping has shown other drawbacks such as thermal instability and photo-corrosion (Shayegan et al., 2017). In addition, although noble metals and rare earth metals could efficiently improve the photocatalytic efficiency, the cost-effectiveness required a certain degree for industrial use is usually caused their replacement by more economical transition or nonmetals doping.

2.6.3 Heterostructure photocatalysts

Heterojunction between different semiconductors is another interesting method which has received considerable interest in the last year (Hernández-Alonso et al., 2009; Ilieva et al., 2012). Zhang et al. (2009) reported that the good matching of the valence band and conduction band of the two semiconductors , ensuring efficient charge carriers transport from one to another.

Coupling TiO_2 with other semiconductors was applied to extend the photoresponse into the visible region and to accelerate the electron and hole separation (Ouyang et al., 2012). These semiconductors include CdS (Liu et al., 2012), SnO_2 (Zhao et al., 2014), WO_3 (Lee & Jo, 2016) and ZnO (Gholami et al., 2014). As illustrated in Table 2.3, semiconductors coupled with TiO_2 gave enhanced photocatalytic degradation compared to the pure TiO_2. Different types of metal/nonmetal dopants with semiconductor composites most be considered for the improvement of TiO_2 photoactivity.

Table 2.3: Summary of the common semiconductor coupled TiO_2 photocatalyst with their operated photocatalytic conditions and maximum efficiencies.

Photocatalyst	Dopant	Pollutant	Experimental condition	Efficiency before coupling	Efficiency after coupling	Remarks	References
CdS/TiO_2/GO	CdS/TiO_2 ratios : 0.18:1, 0.39:1, and 0.55:1	Methylene blue (MB) and Parachlorophenol 4-CP	300 W xenon lamp (390-770 nm); room temperature; MB solution (5 mg L^{-1}, 80 mL) or 4-CP solution (1 mg L^{-1}, 25 mL); treatment time = 120 min; phtocatalyst amount = 5 mg; Hydrothermal method	55.9% for MB and, 28.4% for 4-CP ($rGO-TiO_2$)	90.3% for MB dye , and 65.3% for 4-CP	• GO-TiO_2-0.55CdS exhibited high degradation of MB and 4-CP. • For rGO-TiO_2-0.55CdS, CdS nanoparticles with smaller size of ~30 nm can uniformly cover all the surface of TiO_2 spheres. • rGO-TiO_2-0.55CdS nanocomposite presented a good cycling stability.	(Tian et al., 2017)
CdS/TiO_2	CdS/TiO_2 ratios : 1:100, 2:100:4:100, and 8:100	Methyl Orange (MO)	300 W xenon lamp; room temperature; MO solution (10 mg L^{-1}, 50 mL); treatment time = 75 min; phtocatalyst amount = 50 mg; Sol-gel method	4% for pure TiO_2	100%	• The photocatalytic degradation efficiency of the CdS/TiO_2 catalysts enhanced by increasing in CdS loading from 0.1% to 2.0%, while, a further increase in the CdS loading to 8.0% resulted decreasing in photocatalytic efficiency. • CdS/TiO_2 composites were in a mesoporous structure with uniformly dispersed particles. • 2% CdS/TiO_2 possessed the	(Zhou et al., 2017)

Table 2.3, continued

						largest specific surface area. However, by more increasing from 2% to 8% the surface area was decreased.	
CdS/TiO_2	CdS/TiO_2 ratios : 1:8, 1:4, and 1:1	Acid Rhodamine B (AB)	300 W xenon lamp (λ>420) ; room temperature; AB solution (10 mg L^{-1}, 100 mL); treatment time = 120 min; phtocatalyst amount = 0.1g; wet chemical method	14.6 % for pure TiO_2	100%	• By increasing the mass ratio of CdS/TiO_2 to 1:4 the photocatalytic efficiency was enhanced. However, by more increasing from 1:4 to 1:8 the efficiency was decreased.	(Bai et al., 2011)
SnO_2/TiO_2	Sn/Ti molar ratio of 1:1	Methylene blue (MB)	UV- lamp ; room temperature; MB solution (1×10^{-5} mg L^{-1}, 200 mL); treatment time = 120 min; phtocatalyst amount = 0.08 mg; Sol-gel method	43% for SnO_2, 56% for TiO_2	71%	• Highly uniform structure with core size of ~22 nm and shell thickness of 4 nm was observed. • The Kinetics studies demonstrated the reaction rate constant of TiO_2/SnO_2 core-shell nanoparticles was much higher than those of pure TiO_2 and SnO_2 nanoparticles.	(Farhadi et al., 2017)
WO_3/TiO_2	WO_3/TiO_2 molar ratio : 0.025, 0.05, 0.075, and 0.1	Methylene blue (MB)	UV-lamp ; room temperature; MB solution (6 mg L^{-1}, 100 mL); treatment time = 100 min; phtocatalyst amount = 0.2 g; spray drying	70% for WO_3	90%	• The percentage of [001] planes of TiO_2 anatase increases up to the maximum 21.5 % for the hybrid WO_3/TiO_2 with molar ratio of 0.075, and afterwards it decreases by further increasing the WO_3 content.	(Khan et al., 2017)

Table 2.3, continued

						• By increasing the amount of WO_3 till 0.075 the BET specific surface area of WO_3/TiO_2 increased and more increasing of that resulted in decreasing of the surface area. • The recombination rate charge carriers in all WO_3/TiO_2 composites were effectively decreased. • The 0.075 molar ratio of WO_3/TiO_2 was the most active sample under UV light and dark.	
xBi_2S_3/TiO_2	x = 1, 5, 10, and 15 wt.%	orange G (OG)	tungsten-halogen-lamp; room temperature; OG solution (10 mg L^{-1}, 100 mL); treatment time = 240 min; phtocatalyst amount = 100 mg; precipitation method	NA	100%	• The fast degradation was obtained on 10% Bi_2S_3/TiO_2 and the degradation followed a first order kinetic with a rate constant of 0.32 h^{-1}. • The photoactivity was enhanced under solar irradiation because of TiO_2 activation. • The performance increased with raising the proportion of Bi_2S_3, whereas beyond 10%, the photo-activity decreased.	(Boumaza et al., 2016)

Table 2.3, continued

ZnO/TiO_2	Zn/Ti : 0.31/1, 0.62/1, 1.03/1, and 1.23/1	methyl orange (MO)	Xe-arc lamp ($\lambda \leq 420$); room temperature; MO solution (5 mg L^{-1}, 10 mL); Treatment time = 120 min; phtocatalyst amount = NA; pyrolysis method	20% for TiO_2 and 30% for ZnO	51%	• ZnO NPs were uniformly grafted on the surface of TiO_2-photonic crystal (PC) to form the heterojunction due to intimate interfacial contact between TiO_2 and ZnO NPs. • The ZnO/TiO_2-PC hybrid system possessed excellent photostability.	(Zheng et al., 2015)
ZnO/ N-doped TiO_2	50 wt% of ZnO and 50 wt% of TiO_2	benzene, toluene, and xylenes	White LED lamp ($\lambda \geq 420$); room temperature; benzene, toluene, and xylenes solution (100 mg L^{-1}, 10 mL); Treatment time = 120 min; phtocatalyst amount = 1 g; sol–gel method	NA	86% for benzene, 87% for toluene, and 86% for xylene	• Doped photocatalysts exhibited higher specific surface area. • The presence of nitrogen led to control nucleation and growth of crystallites, as well as the formation of a well-order porous structure. • The N-doped TiO_2 had visible light absorption due to the interstitial doping. • The N-TiO_2-ZnO composite caused to photosensitize ZnO in visible wavelength region and reduce recombination rate of charge carriers. • The highest efficiency was achieved by N-TiO_2-ZnO calcined at 500 °C.	(Ferrari-Lima et al., 2015)
ZnO/ Cu doped TiO_2	Cu:1%, 3%, and 5wt%;	MO	Xe lamp ($\lambda \geq 420$); room temperature; MO solution	For TiO_2 was negligible and	83%	• Doping percentage of 3%	(Dorraj et al., 2017)

Table 2.3, continued

TiO_2/ZnO:10 %, 30%, 50%, and 70%	(15 mg L^{-1}, 100 mL); Treatment time = 60 min; phtocatalyst amount =0.1 g; sol–gel method and subsequent precipitation	for Cu-TiO_2 was 61%	Cu and 30% ZnO exhibited the highest photocatalytic activity. • At the Ti/Zn mass ratio of 50% and 70%, the surface area was significantly small due to blocking the pores of the heterostructured by excess ZnO. • The 3% Cu-TiO_2/30% ZnO nanocomposite sample exhibited the lowest PL intensity.

NA: Not Available, NP: Nanoparticles

Coupling TiO_2 with CdS is regarded as a promising technique in the field of research (Wang et al., 2012). CdS with a 2.4 eV band gap is the one of the most popular semiconductor materials (Huo et al., 2011). The valence and conduction band edges of CdS are both higher than their corresponding counterparts in TiO_2 lattice (Huo et al., 2011). Such suitable alternation in the energy bands of valence and conduction bands allows CdS to serve as photosensitizer to absorb visible light and to generate an electron-hole pair. Consequently, the electrons in the conduction band are excited to the conduction band of the inactivated TiO_2 thus leaving positive holes in CdS valence band. The injected photoelectrons from CdS to TiO_2 can effectively hinder the recombination of electrons and holes in CdS (Jimmy et al., 2003). Due to improved charge separation under visible light illumination, the couple TiO_2/CdS has been extensively used to enhance the photocatalytic degradation of organic pollutants (acid orange II; organic dye drimaren red, phenazopyridine, methyl orange, etc.) by photocatalytic and photo-electrocatalytic reactions (Bessekhouad et al., 2006; Jiang et al., 2011; Tristão et al., 2006; Zyoud et al., 2011). According to Colmenares (2009), S^{2-} in CdS photocatalyst can be easily oxidized by the holes with an accompanying release of Cd^{2+} into the solution and the creation of a porous layer of elemental sulfur on the CdS surface. This phenomenon can harmfully influence the photocatalytic treatment (Robert, 2007).

The couple system SnO_2/TiO_2, where TiO_2 plays the role of photosensitizer for SnO_2 has attracted considerable attention (Khan & Kim, 2009; Zhao et al., 2014). The band gap of SnO_2 is 3.8 eV, and the conduction band of SnO_2 is more positive (0.5 V) than that of TiO_2 and can act as efficient electron sinks to capture photogenerated electrons. Using SnO_2 coupled to TiO_2, the electrons can store on the SnO_2 and the holes can store on the TiO_2 due to the formation of a heterojunction at the SnO_2/TiO_2 interface (Zhao et al., 2014). The SnO_2/TiO_2 system inhabits the charge carrier recombination, confirming

a high apparent quantum efficiency and better photocatalytic efficiency in degradation of organic pollutant under UV light (El-Maghraby et al., 2016). In spite of the greater photocatalytic and photo-electrocatalytic performances of the TiO_2/SnO_2 structure under UV irradiation, but the incorporation of this structure for the large scale environmental applications remains extremely limited owing to the Wide-band gap of both TiO_2 and SnO_2 (Pilkenton & Raftery, 2017).

WO_3/TiO_2 is a structure of semiconductor-semiconductor coupled material, which has been extensively studied and used as a photocatalyst since several decades (Gupta & Tripathi, 2011). The band gap of WO_3 (2.8 eV) is lower than that of TiO_2, and the upper edge position of the valence band and the lower edge position of the conduction band of WO_3 are both lower than that of TiO_2. Therefore, WO_3 can be excited by visible light illumination, and the photogenerated holes transfer from WO_3 to TiO_2 (Miyauchi et al., 2002), while the photogenerated electron in the conduction band of TiO_2 can be accepted by WO_3. However, the preparation technique of coupled semiconductor TiO_2/WO_3 is considered a critical factor that effects the properties of the band structure and, thus, the photocatalytic activity (Zhang et al., 2009).

Zinc oxide (ZnO) is another very important oxide semiconductor photocatalyst and as an alternative to TiO_2 because the photocatalytic mechanism is similar to TiO_2 (Ji et al., 2017; Tejasvi et al., 2015). Furthermore, the main benefit of coupling ZnO to TiO_2 is that it can absorb a larger fraction of the UV radiation and the corresponding threshold value is 425 nm. According to Ferrari-Lima et al. (2015), the heterojunction of TiO_2 and ZnO semiconductors, creates synergic effects, decreases the recombination rate, and increases charge carriers' lifetime. Under illumination, the photogenerated electrons of TiO_2 could transfer to the conduction band of ZnO, whereas the photogenerated holes of ZnO can be easily injected to the valence band of TiO_2. This

effect promotes the charge carrier separation process (Figure 2.7). However both TiO_2 and ZnO require an excitation wavelength that falls in the UV region of 300–390 nm due to high band gap energies. Hence, in order to make ZnO/TiO_2 nanocomposites suitable for receiving and utilizing visible light with high efficiency, numerous methods such as the doping of TiO_2 or ZnO with metal or nonmetal have been investigated (Zha et al., 2015). Kwiatkowski et al. (2017) reported that the visible light response of the ZnO/TiO_2 core/shell composites through the N-doping of TiO_2 shell and its decoration with Au nanoparticles. By a sol-gel method, Li et al. (2015) obtained a visible light active Ce/F co-doped TiO_2–ZnO composite films with a band gap of 1.82 eV.

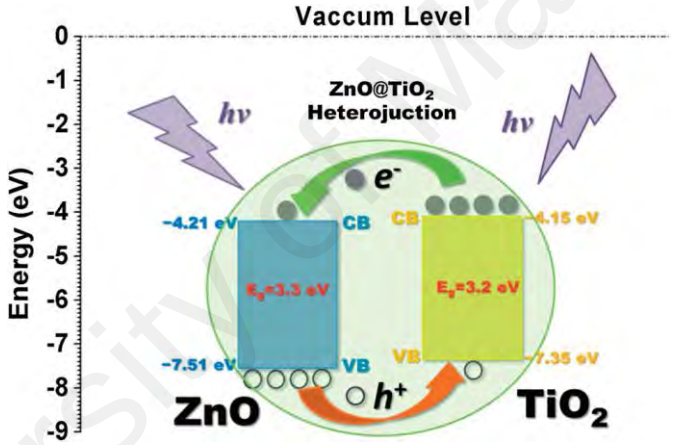

Figure 2.7: An energy level scheme of ZnO and TiO_2. The heterojunction formed between ZnO and TiO_2 promotes charge separation. Reproduced from ref. (Wang et al., 2014) with permission from the Royal Society of Chemistry.

2.6.4 The co-doping of TiO_2

The co-doping of TiO_2 entails the simultaneous incorporation of two heteroatoms into the TiO_2 lattice to tune its optical properties, photocatalytic properties, surface area and crystal structure. It is advancement from the mono-doping process where only one heteroatom is incorporated into the TiO_2 framework. The co-doping of TiO_2 may be achieved by introducing two different nonmetal elements (Wen et al., 2017), two metals

(Cai et al., 2013) or a metal and a nonmetal (Xu et al., 2008) while the mechanism of action is based on the synergy between the two dopants and TiO_2 (Kuvarega et al., 2011). The co-doping of TiO_2 allows the tailoring of the materials with the combined properties of the two dopants such as good visible light absorption (bang gap narrowing) and efficient electron scavenging, resulting in an improved photocatalytic performance.

TiO_2 co-doped with nitrogen and sulfur (N,S-TiO_2) has been prepared by various methods and its photocatalytic properties were studied. The incorporation of N and S improved the photocatalytic performance under visible light as compared to the N-TiO_2, S-TiO_2 and P25. This improvement was attributed to the formation of sub-band gap states by N and S states in the TiO_2 band gap (band gap narrowing) allowing for visible light excitation of electrons from these new states to the TiO_2 conduction band. Simultaneous incorporation of the two dopants provided more routes through which the hydroxyl and superoxide radicals can be generated leading to enhanced photocatalytic activity. Moreover, the co-doping of TiO_2 with N and S suppressed the TiO_2 grain size, increased the surface area, and enhanced the surface acidity of the photocatalyst (Wei et al., 2008; Xiao et al., 2011). Hojamberdiev et al. (2012) prepared N-F co-doped TiO_2 by thermal decomposition of ammonium oxofluorotitanate and the co-doped TiO_2 displayed good photocatalytic activity toward the degradation of methyl orange compared to P25. This was described by contribution of strong absorption in the visible light region, good crystallinity and porous structure. Strong visible light absorption, band gap narrowing and enhanced photoactivity were reported as key modifications induced on TiO_2 by the combined contribution of N and C co-doping (Wang et al., 2011). Similarly, co-doping TiO_2 with other double nonmetal combinations such as I-F(Wen et al., 2009), B-F (Wang et al., 2013), N-P (Han et al., 2010), N-I (Zhou et al.,

2009) and C-F (Lim et al., 2008) displayed the synergistic effect of the dopants towards improvement of the overall photocatalytic activity of TiO_2.

Double metal doped TiO_2 such as Gd/La-TiO_2 (Cai et al., 2013), Nd/Er, Nd/Eu, Eu/Ho-TiO_2 (Reszczyńska et al., 2014), La/Eu-TiO_2 (Huixian et al., 2011) and Li/Y-TiO_2 (Hamden et al., 2014) displayed enhanced photocatalytic activity for the degradation of various organic compounds compared to the mono-doped TiO_2. This was attributed to the efficient visible light harnessing and charge separation.

Many studies have revealed that co-doping TiO_2 with a metal and a nonmetal can lead to a highly efficient visible light active photocatalyst (Sakatani et al., 2004). Gadolinium and nitrogen co-doped TiO_2 (Gd, N-TiO_2) nanotubes were synthesized by a hydrothermal method and ion exchange technique and investigated for degradation of rhodamine B under visible light. Higher photocatalytic degradation efficiency was observed and attributed to co-doping which inhibited the particle growth resulting in a larger surface area of the photocatalyst. Moreover, co-doping improved charge separation, visible light absorption and crystallinity of the photocatalyst (Liu et al., 2011). Similarly, Wu et al. (2011) prepared praseodymium and nitrogen co-doped TiO_2 (Pr,N-TiO_2) via the sol-gel and microwave methods for methyl blue degradation. Both Pr and N were incorporated into the TiO_2 lattice and restrained the TiO_2 grain size growth, extended visible light response toward the visible region and inhibited recombination of the charge carriers, leading to higher photocatalytic activity. The Eu,N-TiO_2 (Xu et al., 2008), Ce,N-TiO_2 (Wang et al., 2011), La,B-TiO_2 (Lan et al., 2014) and Cr,S-TiO_2 (Shao-You et al., 2011) prepared by different methods showed improved visible light response, charge separation and photoactivity, owing to the cooperative effect of the co-dopants. Kuvarega et al (2011) proved that the combination of N/Pd into TiO_2 by improved sol-gel technique shows enhanced photocatalytic

activity of TiO_2 under visible light. The enhancement of photocatalytic activity was attributed to the synergistic doping effects of N and Pd. The previous study by Sakatani et al. (2003) also indicated that La/N co-doped TiO_2 photocatalyst obtained by means of a polymerization technique can lead to high efficiency for the degradation of acetaldehyde under visible light. Pr doping in Pr/N co-doped TiO_2 system was found to hinder the grain growth and anatase to rutile phase transformation. The Pr/N-TiO_2 photocatalyst showed higher photocatalytic activity than those mono-doped N-TiO_2 and pure TiO_2. The N ions were effectively incorporated into the TiO_2 lattice and narrowed the band gap energy. The Pr doping could also decrease the recombination between photogenerated electrons and holes in the TiO_2. The improved photocatalytic activity was ascribed to the synergic effect of N and Pr in co-doped system (Yang et al., 2011).

Usually co-doping involves the use of metals and nonmetals are an effective technique for enhancing the visible-light-induced photocatalytic performance. The simultaneous doping of metal and nonmetal ions creates synergic effect that improves the catalytic properties for enhancement of visible light response. Various studies were performed on metal and nonmetal co-doping, it is clear that the application of new co-doped photocatalytic materials has been greatly focused in photodegradation reactions of organic pollutants in water. The major advantages of this method are: material phase transformation, small grain size, large specific surface area, band-gap narrowing by shifting the light absorption ability from the UV to the visible region, decrease the electron–hole recombination, dopant serves as an active site for pollutant adsorption to accelerate degradation reactions and they can act as photosensitizers to absorb visible light (Tan et al., 2011).

CHAPTER 3: MATERIALS AND METHODS

This chapter gives a detailed amount of the materials, photocatalyst synthesis methods and characterization tools utilized in this study. The photocatalytic reaction process for the prepared photocatalysts is also discussed in this chapter.

3.1 Reagents and materials

All reagents and materials used were of analytical reagent grade, sourced from Sigma Aldrich, and were used as received. The following materials and reagents were utilized in this study: Titanium (IV) bis (ammonium lactato) dihydroxide (TALH) (50 wt% suspension in water), copper (II) acetate (CuAc, 99.99%), zinc acetate dehydrate (ZnAc, 99.99%), potassium iodide (KI, 99%) and gelatin were used as received without further purification.

3.2 Preparation of the photocatalysts

3.2.1 Preparation of Cu-TiO_2/ZnO nanocomposites

Cu-TiO_2 nanoparticles were synthesized by a sol–gel method. Initially, the desired amounts of CuAc were dissolved in 100 mL of deionized (DI) water with stirring. Subsequently, a stoichiometric amount of TALH was added dropwise into the solution with vigorous stirring. The solution was stirred and heated at 80 °C. Finally, gelatin was added to the solution, which was stirred and heated at 80 °C until a white-colored gel was obtained. The gel was calcined at 450 °C for 2 h at a heating rate of 5 °C/min. Different Cu doping levels were prepared by varying the amount of CuAc concentration. The samples were denoted as *x*% Cu-TiO_2, where *x* (1, 3, and 5) is the nominal weight percentage of Cu. For comparison, pure TiO_2 and ZnO were also prepared with the same procedures, and ZnAc was used as the ZnO precursor.

Afterward, the zinc oxide-coupled catalysts (Cu-TiO_2/ *x*% ZnO, where *x* represents the nominal mass ratio of ZnO to Cu-TiO_2) were prepared using the precipitation method. The desired amount of ZnAc was dispersed in 100 mL of DI water under vigorous stirring, until the solution became transparent. Appropriate quantities of Cu-TiO_2 nanopowders were dispersed in aqueous solution with ultrasonication and continuous stirring. During precipitation, suspension was allowed to settle for 24 h. The precipitate was filtered and washed with DI water repeatedly. The obtained paste was dried at 90 °C for 15 h and calcined at 450 °C for 2 h. A simplified schematic showing the two-step preparation of coupled photocatalyst is illustrated in Figure 3.1.

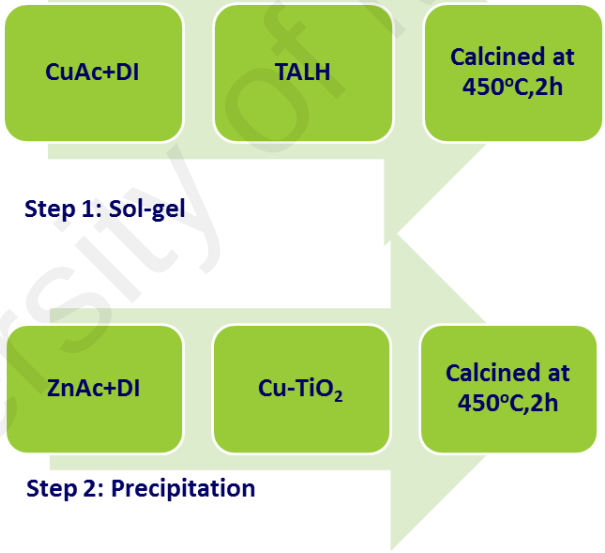

Figure 3.1: Schematic preparation of Cu-TiO_2/ZnO.

For comparison, a series of Cu-TiO_2/ *x*% ZnO photocatalysts with different mass ratios (10%, 30%, 50%, and 70%) were also prepared by changing the ZnO content. The weight of Ti, Cu, and Zn precursors for preparing 2 g TiO_2 and 0.5 g Cu-TiO_2 are presented in Table 3.1.

Table 3.1: The weight of Ti, Cu and Zn precursors used for preparing the nanocomposites.

Precursors	Weight (%)	Weight (g)
TALH	-	14.729
CuAc	1	0.057
	3	0.171
	5	0.285
ZnAC	10	0.113
	30	0.338
	50	0.563
	70	0.789

3.2.2 Preparation of Cu-I co-doped TiO_2

The hydrothermal method was utilized to synthesize the pure, mono-doped, and co-doped TiO_2 samples. About, 14.7 g TALH was added dropwise into 100 mL deionized DI water with vigorous stirring for 30 min. The metal and nonmetal doped TiO_2 solutions were prepared by dissolving stoichiometric amounts of metal and nonmetal precursors in the TiO_2 precursor solution. For the preparation of the Cu-TiO_2 and I-TiO_2 sols, appropriate amounts of CuAc and KI were dissolved in DI water before added to the TiO_2 sol. The Cu-I co-doped TiO_2 sample was formed by the incorporation of both Cu and I precursors in the TiO_2 sol. The final mixtures were transferred into a Teflon-lined stainless-steel autoclave and kept at 180 °C for 18 h. The resulting powders were subsequently centrifuged and then washed with water before drying at 80 °C for 15 h. Finally, the samples were calcined at different temperatures (350 °C, 450 °C, and 550 °C) in air for 2 h. A simplified schematic showing the step preparation of co-doped photocatalyst is illustrated in Figure 3.2.

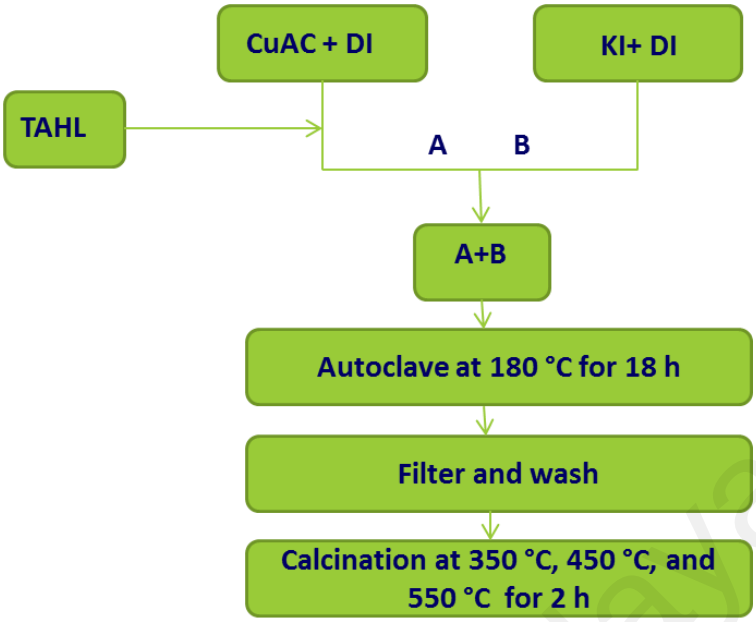

Figure 3.2: Schematic preparation of Cu-I-co-doped.

The 3 wt% of Cu was used in the samples according to the "optimum" concentration used in our previous study (Dorraj et al., 2017). Zhang et al. (2011) reported that 10 wt% of I provides optimum activity under visible light for the I-doped TiO_2. The weight of Ti, Cu, and I precursors for preparing 2g TiO_2 are presented in Table 3.2.

Table 3.2: The exact weight of Ti, Cu and I precursors used for preparing the Cu-I co- doped TiO_2.

Precursors	Weight (%)	Weight (g)
TALH	-	14.729
CuAc	3	0.171
KI	10	0.340

3.3 Characterization techniques

3.3.1 X-ray diffraction (XRD) measurements

The phase and crystallite size of all prepared samples were studied by X-ray diffraction (XRD, Siemens D5000; TX, USA) using monochromated high-intensity Cu

K (alpha) radiation (λ = 1.54060 Å) operated at 40 kV and 40 mA. Measurements were performed at a 2θ between 20–80° at a rate of 0.5°/min. The step time and step size of the scan were fixed at 2 s and 0.026°, respectively. The obtained XRD spectrum was then matched with a Powder Diffraction File (PDF) database maintained by the International Center for Diffraction Data (ICDD).

The fractional phase content for anatase (A) and rutile (R) in the samples can be calculated in Equation (3.1) and Equation (3.2) (Li et al., 2015):

$$A = \frac{K_A I_A}{K_A I_A + K_R I_R} \quad \text{(Equation 3.1)}$$

$$R = \frac{K_R I_R}{K_A I_A + K_R I_R} \quad \text{(Equation 3.2)}$$

$$K_A = 0.886, K_R = 1$$

where I_A (0 1 1) and I_R (1 1 0) are the integrated intensities of the main peaks of anatase and rutile, respectively.

3.3.2 Microscopy analyses

Field emission scanning electron microscopy (FESEM, Hitachi SU 8000; Tokyo, Japan), operating at 15kV, attached with energy dispersive X-ray spectroscopy (EDX, Bruker XFlash 6|100) was applied to study the morphology and elemental composition of the samples. The sample powders were mounted on glass slides or silicon wafer using a double-sided carbon tape and coated with gold before loaded in the FESEM for analysis. The transmission electron microscopy (TEM) and high-resolution TEM

images (HRTEM) were performed by a JOEL TEM 2010 instrument at 200 kV to investigate the particle size and lattice information of the samples. Gatan Digital Micrograph software was utilized for an accurate calculation of the lattice spacing. A small amount of sample was sonicated for a few minutes in ethanol and a small drop of the suspension was drop-casted on a copper grid. The grid was allowed to dry in air before being mounted on the sample holder for analyses.

3.3.3 Raman spectroscopy

The Raman spectra of all samples were collected using a confocal micro-Raman system (inVia, Renishaw) in a back-scattering configuration. The samples were excited by 532 nm DPSS laser at room temperature. A 50X objective (Leica) was utilized to focus the laser beam onto the sample and the collection efficiency of scattered photons from the sample was at maximum. The signal was collected by a charge-coupled linear array device and it was cooled to as low as −70 °C.

3.3.4 Diffuse reflectance UV-vis spectroscopy

Diffuse reflectance UV-vis spectroscopy of the catalysts was obtained by a Shimadzu 2450 UV-vis spectrophotometer between 200–800 nm. Barium sulfate was used as a standard reference.

The band gaps of the photocatalysts synthesized in this study were determined using the Tauc's equation (Equation 3.3), where α is the absorption coefficient and (hν) is the incident photon energy, and E_g is the band gap (Slav, 2011). The constant n accounts for the type of optical transition. For a direct transition, n=1/2 while for an indirect transition, n=2.

$$\alpha h\nu = A(h\nu - E_g)^n \qquad \text{(Equation 3.3)}$$

TiO_2 is an indirect semiconductor, while ZnO is a direct semiconductor, hence the band gap was measured as a plot of $(\alpha hv)^{1/2}$ or $(\alpha hv)^2$ against hv, respectively. The exact value of the band gap was determined by extrapolation of the liner region of a plot of $(\alpha hv)^{1/2}$ or $(\alpha hv)^2$ on the y-axis versus photon energy (hv) on the x-axis was taken as the band gap for TiO_2 and ZnO, respectively.

3.3.5 Photoluminescence (PL) spectroscopy

The photoluminescence (PL) emission spectra were recorded at room temperature with an InVia Raman microscope equipped with a confocal microscope with a "He-Cd laser" working at 325 nm excitation wavelength at 5 mW. The resulting luminescence is collected with two high numerical aperture lenses and is then spectrally dispersed by a SPEX model 750M monochrometer. The dispersed luminescence signal is detected with a photomultiplier tube (PMT) that can be used for detecting the light from near-UV to 1200 nm. The signals produced by the PMT are measured using a Stanford Research Systems SR830 lock-in amplifier, and data are recorded and processed by a computer.

3.3.6 Brunauer–Emmett–Teller (BET) measurement

The BET specific surface areas and pore size distribution of the photocatalysts were determined by the N_2 adsorption–desorption isotherms at 77 K using a Micrometrics ASAP 2020 surface area and porosity analyzer. Prior to the analysis, the photocatalyst samples were degassed in vacuum at 150 °C for an hour to remove moisture.

3.3.7 X-ray photoelectron spectroscopy (XPS)

The X-ray photoelectron spectroscopy (XPS) analyses were carried out in an ultrahigh vacuum chamber with a base pressure below 2.66×10^{-7} Pa at room temperature. The photoemission spectra were recorded by a PHI Quantera Versa Probe II instrument equipped with monochromatic focused Al Kα source. The pass energy and step size of high-resolution XPS scan were adjusted to 40 and 0.1 eV, respectively. The

curve fitting was performed using a non-linear least square Gaussian-Lorenzian function after subtraction of Shirley background. All binding energies (BE) were referenced to C 1s at 284.8 eV.

3.3.8 Inductively coupled plasma mass spectrometry (ICP-MS)

The accurate compositions of the samples in the co-doped sample were analyzed with the inductively coupled plasma mass spectrometry (ICP-MS 7500 Single Turbo System). Prior to analysis, 0.1 g co-doped sample was mixed with 8 mL nitric acid, 8 mL hydrochloric acid and 2 mL hydrofluoric acid. Then, the acid mixture was digested in a microwave oven (Milestone ETHOS) by heating at 250 °C for 15 min. The digested samples were diluted, and the concentrations of Cu and I were obtained by ICP-MS.

3.3.9 Electro-chemical impedance spectroscopy (EIS)

Electro-chemical impedance spectroscopy (EIS) measurements were performed in 0.1 M Na_2SO_4 aqueous solution as the electrolyte, whereas 150 W HALOID lamp was the visible light source. The working electrode was prepared by drop-casting a homogenous dispersion of the samples in ethanol on fluorine-doped tin oxide glass slides. The working electrode for the EIS was obtained after calcination at 400 °C for 2 h. A saturated calomel electrode and platinum wire were the reference and counter electrodes, respectively. The EIS measurements were performed over a frequency range between 0.1 and 100 KHz, with amplitude of 0.01 V around the open circuit potential.

3.4 Photocatalytic activity test

Photodegradation of 15 mg L^{-1} MO dye solutions was performed to investigate the photocatalytic activity of all samples under visible-light irradiation. Precisely 0.1 g of catalyst powder was dispersed into 100 mL aqueous MO solution for each experiment. The suspension was stirred in the dark for 1 h to reach the dye adsorption–desorption equilibrium on the photocatalyst surface. A 500 W Xenon lamp equipped with a UV

cut-off filter (λ>420 nm) was used as a visible light source. Meanwhile, the reactor temperature was controlled by a circulated water jacket to remove the lamp heat. Accordingly, 1 mL of the MO solution was filtered from the reactor with a 20 min time interval to analyze the reaction. The photocatalytic activity was investigated by measuring the intensity of the absorption peak of MO at 464 nm using a UV-vis spectrophotometer (Kwiatkowski et al., 2017). The degradation efficiency of MO was calculated using the following equation:

$$\text{Degradation } (\%) = \left(1 - {}^{C_t}/_{C_0}\right) \times 100\% \qquad \text{(Equation 3.4)}$$

where C_0 is the adsorption equilibrium concentration of the solution, and C_t is the concentration of solution at time t. In order to determine the photocatalytic degradation rates of MO, the first-order kinetics (Equation 3.5) were employed to fit the obtained data (Chen et al., 2017).

$$ln\, {}^{C_0}/_{C} = k(t) \qquad \text{(Equation 3.5)}$$

Where k is the apparent rate constant, C is the solution phase concentration and C_0 is the concentration at t=0. Figure 3.3 shows the schematic experimental set up for the photocatalytic degradation of MO aqueous solution.

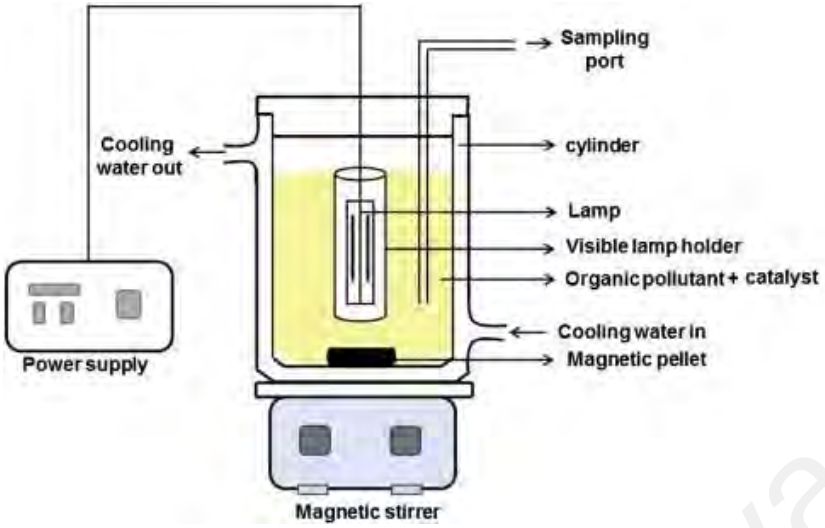

Figure 3.3: Schematic experimental setup for photocatalytic degradation of MO aqueous solution.

3.5 Recycling test

After each photocatalytic experiment, recycling experiments were carried out *via* centrifuging and washing the composite with ethanol for 1 h under magnetic stirring. Reusability of each photocatalyst was evaluated by using the same catalyst by repeating the degradation experiment of the same initial MO concentration.

3.6 Detection of Reactive Oxygen Species

Radical scavenger studies were carried out to investigate the active species involved in the photodegradation of dye. Three scavengers were selected, namely, *tert*–butyl alcohol TBA ($OH^{\bullet}$ radical scavenger), ammonium oxalate AO (hole scavenger) and benzoquinone BQ ($^{\bullet}O_2^-$ radical scavenger) (Li et al., 2017). All experiments were carried out in the photoreactor described in Section 3.4. 1 mL and 1 mM of TBA, AO and BQ were added into the photocatalytic system to examine the photocatalytic mechanism, respectively.

3.7 Hydroxyl radical (OH•) formation tests

The capability of the co-doped sample to form hydroxyl radicals (OH•) under visible-light irradiation was determined by the fluorescence method with terephthalic acid (TPA) as the probe molecule (Silva et al., 2017). The reaction between photogenerated OH• radicals and TPA produced the 2-hydroxyterephthalic acid (HTPA), a fluorescence-active molecule. Hence, HTPA fluorescence intensity was directly proportional to the OH• quantity formed on the surface of photocatalysts. In this experiment, 0.1 g of co-doped photocatalyst was placed in contact with 30 mL of TPA solution ($5x10^{-4}$ mol L^{-1}) prepared in aqueous NaOH ($2x10^{-3}$ mol L^{-1}). All experiments were carried out in the photoreactor described in Section 3.4. At regular intervals, the HTPA concentration was monitored by fluorescence measurements using a Shimadzu RF-5301PC spectrofluorophotomete. The fluorescence emission spectrum in the scanning light wavelength of 300–550 nm ($\lambda_{maximum}$ = 425 nm) was obtained using excitation wavelength of 315 nm.

CHAPTER 4: RESULTS AND INTERPRETATIONS

The photocatalysts were synthesized as described in chapter 3. The synthesized materials were characterized by various characterization techniques and are discussed in this chapter. The photodegradation results of MO by the photocatalysts together with a possible mechanism for the enhanced photocatalytic activity and catalyst recycling experiment are also discussed.

4.1 Enhanced visible light photocatalytic activity of copper-doped titanium dioxide–zinc oxide heterojunction for methyl orange degradation

Photocatalysts have been attracting significant attention as effective environment-friendly technology because of their wide spectral range for solar energy conversion into chemical energy. This technology is used to control and remove different types of organic pollutants in water. Among all the semiconductor-based photocatalysts, TiO_2 has been the ideal material because of its nontoxicity, high chemical stability, and oxidization feature (Jo et al. 2016). However, the high TiO_2 bandgap energy restricts its practical application in the ultraviolet region, which corresponds to only 4%–5% of the entire solar spectrum (Dorraj et al., 2017). Hence, numerous studies have developed visible light driven TiO_2-based photocatalyst by doping metal (Lee et al., 2016; Pham et al., 2015) and nonmetal (Khalid et al., 2012; Morikawa et al., 2001; Serpone, 2006; Yoshida et al., 2015) ions in the TiO_2 lattice. Transition metal-doped TiO_2 can be effectively used to improve the visible light induced photocatalytic performance. Incorporating 3d transition metal ions in the TiO_2 crystal lattice creates impurity states close to the valence band (VB) and conduction band (CB), thereby resulting in a remarkable energy gap narrowing toward the visible region (Shao, 2008; Wang et al., 2014). Guo and Du (2012) reported that Cu doping can broaden the adsorption edge of TiO_2 into the visible region by forming dopant states above the VB caused by the Cu-3d

orbital. Khalid et al. (2013) reported that doping TiO_2 with Cu could enhance the visible light response and photocatalytic activity during methyl orange (MO) photodegradation. Although an improved photocatalytic activity of the bulk-doped TiO_2 particles has been reported, adverse side effects could not be eliminated because many of the newly created interband energy states can also act as recombination centers, which increase the recombination rate of charge carriers and degrade the photocatalytic activity (Liu et al., 2012; Peng et al., 2009; Su et al., 2012).

In recent year, the coupling of two semiconductors based on the matching of band potentials in the form of a heterojunction is identified as an effective approach to enhance the separation efficiency of the photoinduced electrons and holes (Guo & Du, 2012). Gao and his coworkers (2016) reported the formation of $BiPO_4$/BiOBr heterostructured photocatalysts through a facile *in situ* chemical transformation. The heterostructures exhibit excellent photocatalytic activity and stability during rhodamine B degradation under visible light irradiation. Among the reported coupled semiconductor nanostructures, ZnO-based nanocomposites exhibit an efficient electron–hole pair separation in TiO_2 due to the high photocatalytic performance and similar photodegradation mechanisms (Ferrari-Lima et al., 2015; Tejasvi et al., 2015). For example, Zha et al. (2015) investigated a distinct TiO_2/ZnO heterostructure, which showed significantly improved photocatalytic performance compared to the pure TiO_2 and ZnO due to the efficient electron–hole pair separation and low recombination rates of the charge carrier. Hence, the visible spectral response ability of a transition metal-doped TiO_2 and the efficient spatial separation of electrons and holes by ZnO coupling may offer an alternative approach for the photocatalytic degradation of organic pollutants. Nevertheless, to the best of our knowledge, few works has been devoted to the photocatalytic behavior of a metal-doped semiconductor coupled with another band-edge semiconductor. Therefore, the study

using both two strategies to enhance the photocatalytic performance of TiO_2 is limited. In the present work, a stepwise approach for TiO_2 photocatalyst modification was introduced. The Cu-doped TiO_2 (Cu-TiO_2) was successfully coupled with ZnO at different mass ratios through the sol–gel method and subsequent precipitation. The structural, optical and morphological properties of the composite were also investigated. The visible light-driven photocatalytic activity of the Cu-TiO_2 coupled with ZnO nanoparticle (Cu-TiO_2/ZnO) heterojunction nanocomposite was utilized for the degradation of MO. The possible mechanism for the enhanced photocatalytic activity was also investigated.

4.1.1 PL spectra analysis

The PL measurement was performed to analyze the photogenerated carrier separation efficiency of the doped and coupled samples. Figure 4.1 shows the PL emission spectra of TiO_2 and x% Cu-TiO_2. The PL emission intensity of a semiconductor is proportional to the photo-induced electron–hole recombination rate. TiO_2 is a semiconductor with an indirect band gap, and it exhibits a broad visible luminescence spectrum, which is related with the transition of a trapped charge carriers in the oxygen vacancy to the TiO_2 VB (Tahir & Amin, 2015). The emission intensity of TiO_2 is significantly weakened in the x% Cu-TiO_2. This result indicates that the recombination of photogenerated charge carriers from the oxygen defects to the TiO_2 VB is effectively suppressed with Cu ion doping. The PL spectrum of the pure TiO_2 is not discussed because it is considerably broad, and reliable information is difficult to extract. Therefore, the focus is towards the Cu-TiO_2 spectra. The PL phenomenon is mainly associated with the optical recombination related with the defect level. Thus, this phenomenon cannot be attributed to the oxide band gap transitions.

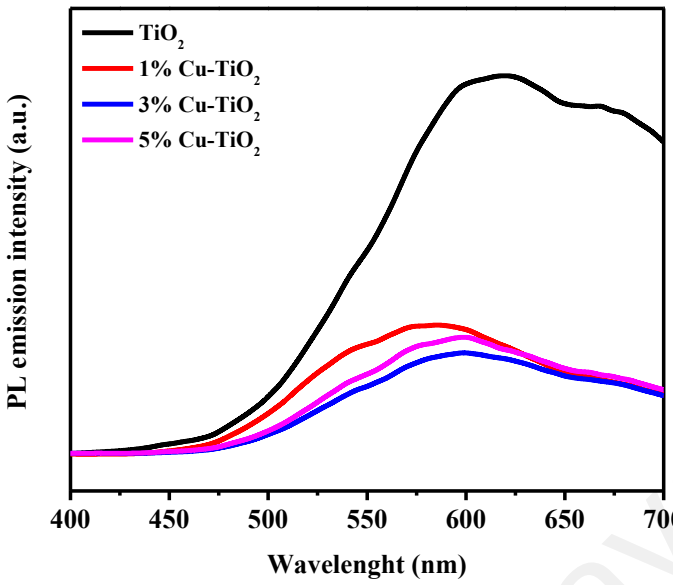

Figure 4.1: Room-temperature PL emission spectra of TiO_2, 1% Cu-TiO_2, 3% Cu-TiO_2, and 5% Cu-TiO_2 nanoparticles.

Figure 4.2a shows a typical fitting of the 3% Cu-TiO_2 PL spectra using the Gaussian distribution. These bands show a peak energy around 1.87 (E1), 2.09 (E2), and 2.29 eV (E3). Previous studies have revealed important modifications of the TiO_2 band under visible light caused by the incorporation of Cu in the TiO_2 lattice (Choudhury et al., 2013). The formation of energy levels from the oxygen defects and middle-gap levels of Cu (3d) introduced below the Ti (3d) CB and above the O (2p) VB of TiO_2 were reported as an acceptor level (Yan et al., 2016). An optical transition between the Cu (3d) and O defect levels of the Cu-TiO_2 system was also observed. This optical transition could be correlated with the PL band around 1.9 eV (E1), which is close to the reported value (1.9 eV) of the optical transition attributed to the transition metal impurity state and O defect level (Al Saqri et al., 2017). The PL peak (E2) around 2.1 eV is attributed to the recombination of the CB electrons and vacancies at the Cu (3d) levels (Jaiswal et al., 2015). Another emission at approximately 2.3 eV (E3) is also

observed and attributed to the transition from the oxygen vacancies with one trapped electron to the TiO_2 VB (Tahir & Amin, 2015).

Based on these results, a structural model we proposed (Figure 4.2b) for the optical recombination due to the presence of defects between the VB and CB of Cu-TiO_2. The 3% Cu-TiO_2 sample shows the lowest PL intensity, which indicated the lowest recombination rate. Figure 4.1 displays that the charge recombination centers may also increase if the copper dopant amount exceeds than the optimum concentration (Liu et al., 2012).

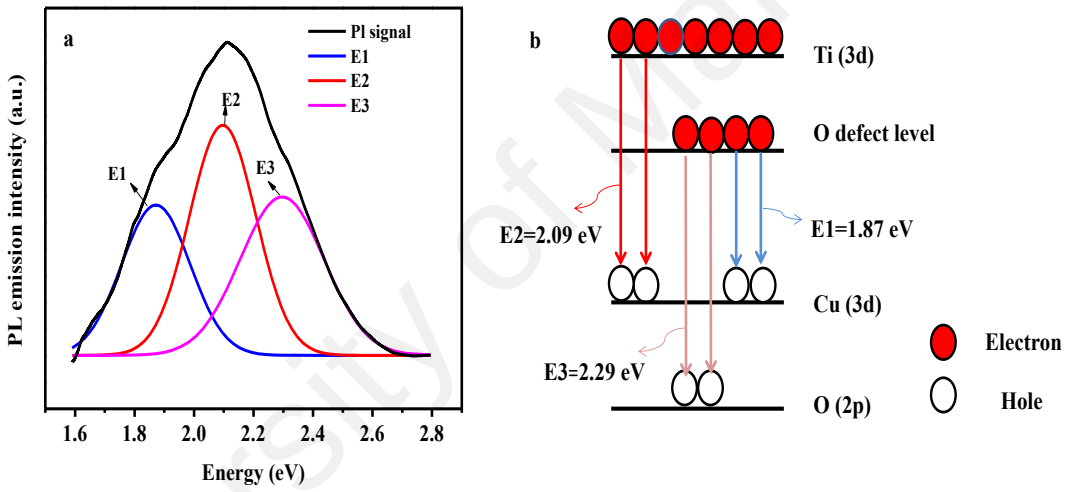

Figure 4.2: Room-temperature PL emission spectra of (a) Typical Gaussian fitting of PL spectra of the 3% Cu-TiO_2 (b) Proposed schematic diagram of optical recombinations in the presence of defects in the 3% Cu-TiO_2.

Hence, among the doped nanocomposite photocatalyst samples, the 3% Cu-TiO_2 was selected to couple with ZnO. As shown in Figure 4.3a, the 3% Cu-TiO_2/30% ZnO nanocomposite sample exhibits the lowest PL intensity. This observation suggests that the optimal loading of ZnO with 3% Cu-TiO_2 could decrease the recombination of photoexcited electrons and holes, thereby indicating that the heterojunction formation can effectively suppress the irradiative recombination (Yan et al., 2014). Furthermore,

Figure 4.3b compares the PL emission intensity of the optimal amount of doping and coupling. The insignificant PL intensity of 3% Cu-TiO_2/30% ZnO nanocomposite suggests that the 3% Cu–TiO_2/30% ZnO heterojunction will facilitate the photocatalytic activity during the organic pollutant degradation.

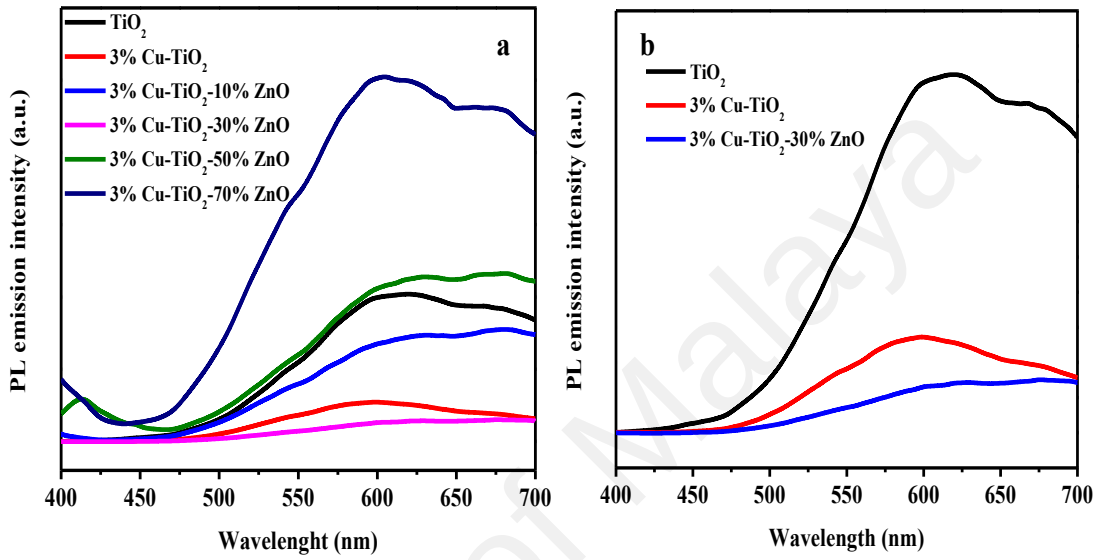

Figure 4.3: Room-temperature PL emission spectra of (a) PL emission spectra of TiO_2, 3% Cu-TiO_2 nanoparticles, 3% Cu-TiO_2/10% ZnO, 3% Cu-TiO_2/30% ZnO, 3% Cu-TiO_2/50% ZnO, and 3% Cu-TiO_2/70% ZnO nanocomposite (b) PL emission spectra of TiO_2, 3% Cu- TiO_2 nanoparticles, and 3% Cu-TiO_2/30% ZnO nanocomposite.

4.1.2 XRD analysis

Figure 4.4a shows the XRD patterns of TiO_2 and Cu (1 wt%, 3 wt%, and 5 wt%)-doped TiO_2 nanoparticles. Figure 4.4(b) illustrates the XRD profiles of the crystal structures of pure TiO_2, ZnO nanoparticles, and 3% Cu-TiO_2-*x*% ZnO nanocomposites. For the pure TiO_2, doped, and coupled samples, the XRD patterns exclusively show peaks with high intensities corresponding to the (011), (112), (020), (015), (121), (024), (116), (220), and (125) crystal planes of anatase TiO_2 (COD 96-900-8214). Evidently, the XRD patterns show no trace of any copper metal, oxide, or binary titanium copper phase. Therefore, the Cu atoms are doped in the crystal lattice of TiO_2 in all samples

because of the relatively small differences of their respective ionic radius (Bensouici et al., 2017).

As shown in Figure 4.4b, the coupled nanocomposites consist of both anatase TiO_2 and wurtzite ZnO. Ten characteristic peaks marked with the Miller indices ((010), (002), (011), (012), (110), (013), (020), (112), (012), and (022)) are well indexed to the standard hexagonal structure (COD 96-230-0114) of ZnO. This result reveals that the ZnO nanoparticle exists in the wurtzite phase (COD 96-230-0114). In addition to the characteristic peaks of TiO_2 and ZnO, the absence of impurity peaks proves that no extra phases were generated during the Cu-TiO_2-ZnO synthesis. Furthermore, with the increase of the Zn/Ti mass ratio from 1:9 to 7:3, the characteristic peaks of anatase TiO_2 gradually decreased, whereas those of wurtzite ZnO gradually increased. These XRD results further confirm the successful preparation of the coupled bicomponent nanocomposites of the TiO_2 anatase and ZnO wurtzite phases.

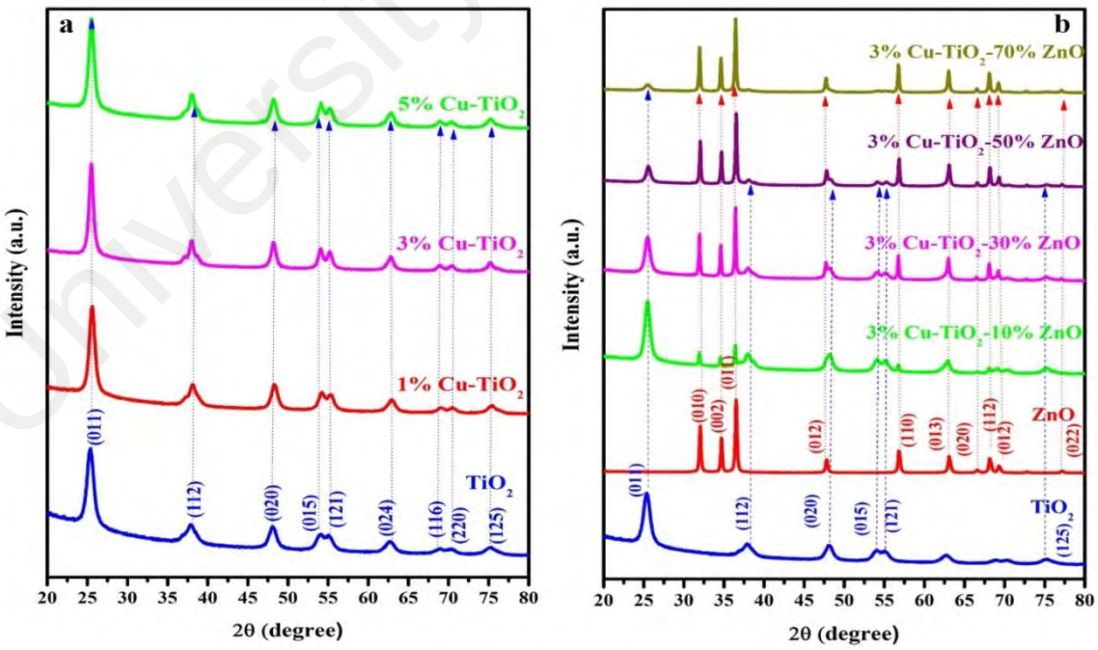

Figure 4.4: XRD patterns of (a) TiO_2, 1% Cu-TiO_2, 3% Cu-TiO_2 and, 5% Cu-TiO_2 nanoparticles (b) TiO_2, ZnO, 3% Cu-TiO_2/10% ZnO,3% Cu-TiO_2/30% ZnO, 3% Cu-TiO_2/50% ZnO, 3% Cu-TiO_2/70% ZnO nanocomposite.

The mean crystallite sizes of TiO_2 and ZnO could be deduced from the full width at half-maximum of the most intense peaks using the Scherrer's equation (Prasannalakshmi & Shanmugam, 2017). The inferred mean crystallite sizes of TiO_2 are around 14 ± 2 nm for the pure TiO_2, 1% Cu-TiO_2, 3% Cu-TiO_2, and 5% Cu-TiO_2. This result is in accordance with previous study (Bensouici et al., 2017), which indicated that the crystallite size of TiO_2 is barely influenced by the variation in Cu doping concentration. The ZnO sizes are 42.7, 45.8, 49.4, and 52.4 nm for the 3% Cu-TiO_2/10% ZnO, 3% Cu-TiO_2/30% ZnO, 3% Cu-TiO_2/50% ZnO, and 3% Cu-TiO_2/70% ZnO nanocomposites, respectively.

4.1.3 XPS analysis

The chemical states of each element in the 3% Cu-TiO_2/ZnO nanocomposite with different Zn/Ti ratios were investigated by XPS and are shown in Figures 4.5A–D. The a, b, c, and d spectra represent the 3% Cu-TiO_2/10% ZnO, 3% Cu-TiO_2/30% ZnO, 3% Cu-TiO_2/50% ZnO, and 3% Cu-TiO_2/70% ZnO nanocomposites, respectively. Moreover, the spectra corresponding to the pure TiO_2 and 3% Cu-TiO_2 are included for comparison.

As shown in Figure 4.5A, all ZnO coupled samples display a similar Zn 2p spectrum. The two major characteristic peaks at binding energies of 1021.4 and 1044.2 eV could be attributed to the Zn $2p_{3/2}$ and Zn $2p_{1/2}$ states, respectively. These results indicate that the Zn^{2+} ions are not incorporated in the TiO_2 lattice; instead, they exist as a separate ZnO phase because no other Zn 2p peaks are observed in the XPS spectra (Zha et al., 2015). Evidently, the peak intensity is the only major difference among the four spectra, which could be attributed to the different ZnO contents in the samples.

The Ti 2p core-level photoelectron spectrum is shown in Figure 4.5B. In each spectrum, the two main peaks are attributed to the Ti $2p_{3/2}$ and Ti $2p_{1/2}$ states, which are

located at around 458.1 and 463.8 eV, respectively. The Ti $2p_{3/2}$ and Ti $2p_{1/2}$ spin-orbit splitting photoelectrons of pure TiO_2 are located at 458.6 and 464.6 eV (Ullah et al., 2014; Wang et al., 2014), respectively. After doping with Cu, the binding energy shifts to lower energies compared to that of the pure TiO_2, as shown in Figure 4.3B. These low binding energy shifts showed that the structure of the local state of titanium atoms changed with the doping with Cu dopant because of the formation of Cu–O–Ti bonds in the crystal lattice of TiO_2 (Zhou et al., 2016). In addition, the peak intensity of the Ti 2p spectra remarkably decreases with increasing Zn/Ti mass ratios.

As shown in Figure 4.5C, the Cu-TiO_2 sample and four ZnO-modified samples show a typical Cu 2p XPS spectra with characteristic Cu $2p_{3/2}$ and Cu $2p_{1/2}$ peaks at 932.5 and 952.5 eV, respectively. This result is consistent with the literature data on the Cu^{+2} ions (Yan et al., 2016; Zhou et al., 2016).

Figure 4.5D shows the XPS spectra of the O 1s region from various samples. The curve fittings of the O 1s spectra were also obtained using a combined Gaussian distribution of variable proportions (Yang et al., 2015). The spectra of all ZnO-modified samples could be deconvoluted into three different near-Gaussian subpeaks centered at 529.5± 0.3, 531± 0.1, and 531.8± 0.1eV (Figure 4.5D). The peaks located at 529.5± 0.3 and 531.3± 0.1 eV (Kotsis & Staemmler, 2006) are assigned to the O–Ti and Zn–O bonds of metal oxides. The peak at the highest energy level (531.8± 0.1 eV) can be attributed to the adsorbed oxygen from the oxide defects or hydroxyl groups (Zhang et al., 2014). Similar to the Ti 2p binding energies, the peak position of the O 1s core levels is also slightly shifted toward lower binding energy compared to that of the O 1s binding energy in pure TiO_2, which is located at 530 eV (Zhou et al., 2016).

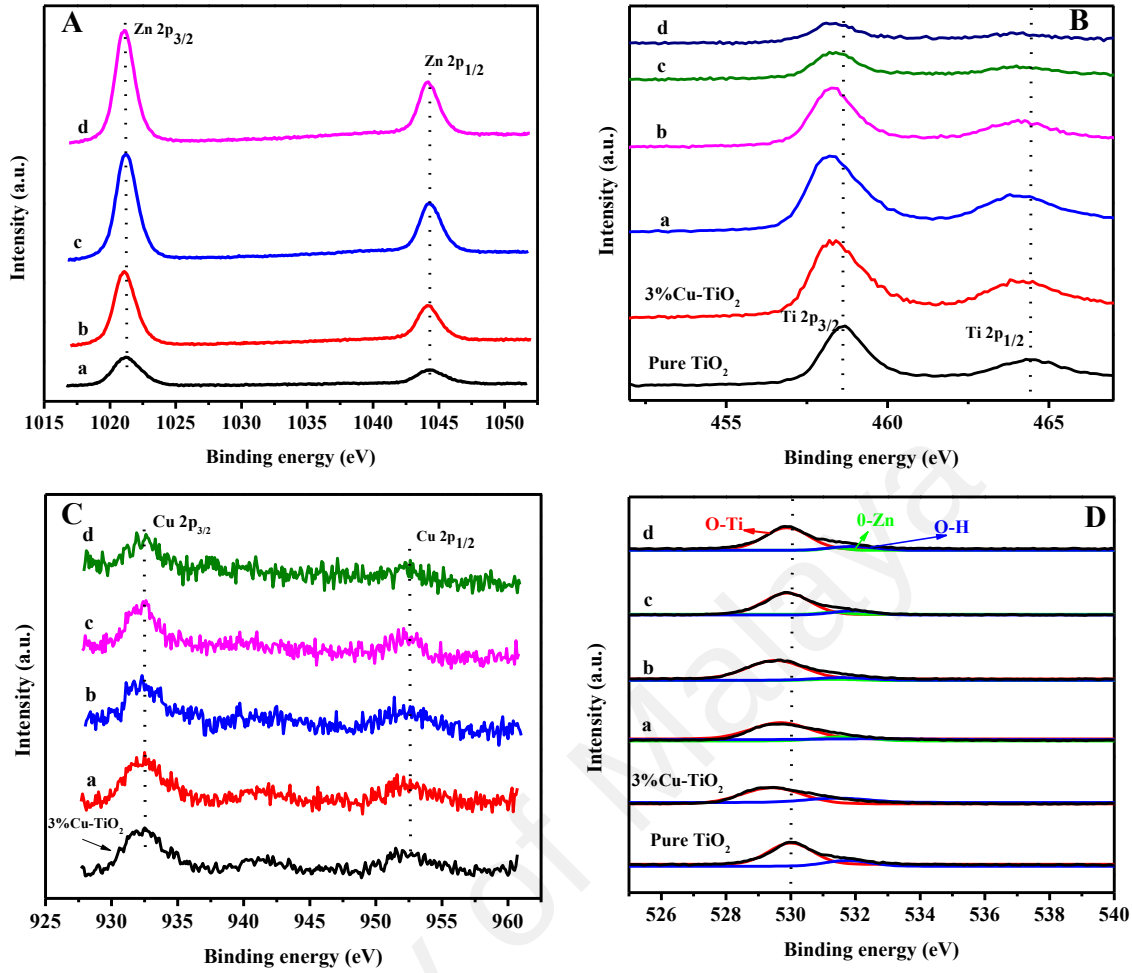

Figure 4.5: (A) Zn 2p, (B) Ti 2p, (C) Cu 2p and (D) O 1s XPS spectra of the samples: (a) 3% Cu-TiO_2/10% ZnO, (b) 3% Cu-TiO_2/30% ZnO, (c) 3% Cu-TiO_2/50% ZnO, and (d) 3% Cu-TiO_2/70% ZnO nanocomposites.

4.1.4 Morphological analysis

The morphology of the optimized 3% Cu-TiO_2/30%ZnO nanocomposite was investigated by FESEM and the result is presented in Figure 4.6. The nanocomposites show agglomerated uniformly shaped particles; the agglomeration may have occurred due to the interaction of the small crystallites (Tahir & Amin, 2015).

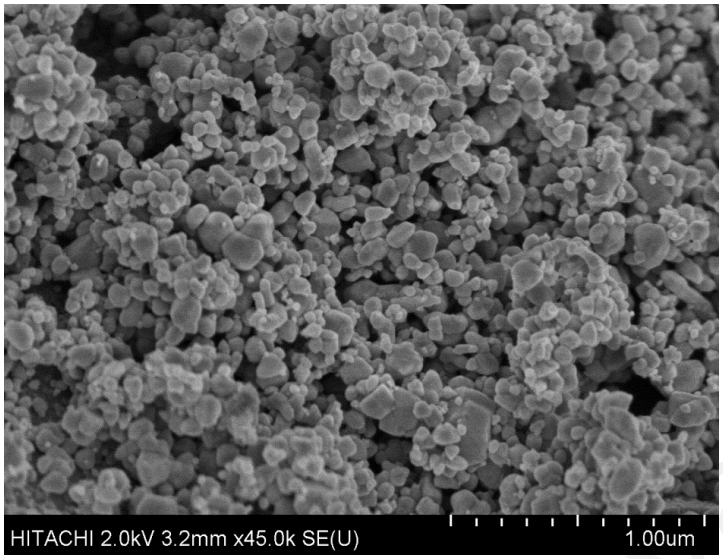

Figure 4.6: FESEM image of 3% Cu-TiO_2/30% ZnO nanocomposite.

The TEM images of 3% Cu-TiO_2 and 3% Cu-TiO_2/30% ZnO nanostructures are shown in Figures 4.7a and 4.7b, respectively. The TEM image of 3% Cu-TiO_2 revealed the presence of spherical particles with uniform sizes between 25–35 nm (Figure 4.7a). The nanoparticles show an interparticle mesoporous structure, possibly due to the growth and aggregation of small particles. When ZnO is added, the Cu-TiO_2 nanoparticles with small sizes are decorated on the surface of ZnO with particle size between 80–90 nm; this result indicates the formation of 3% Cu-TiO_2/30% ZnO heterostructures during the synthesis (Figure 4.7b). The corresponding HRTEM image in Figure 4.7c reveals that this novel nanocomposite is polycrystalline in nature. Moreover, the lattice fringes with a *d* spacing of 0.35 and 0.24 correspond well to the (011) and (011) planes of the tetragonal TiO_2 and hexagonal ZnO phases, respectively.

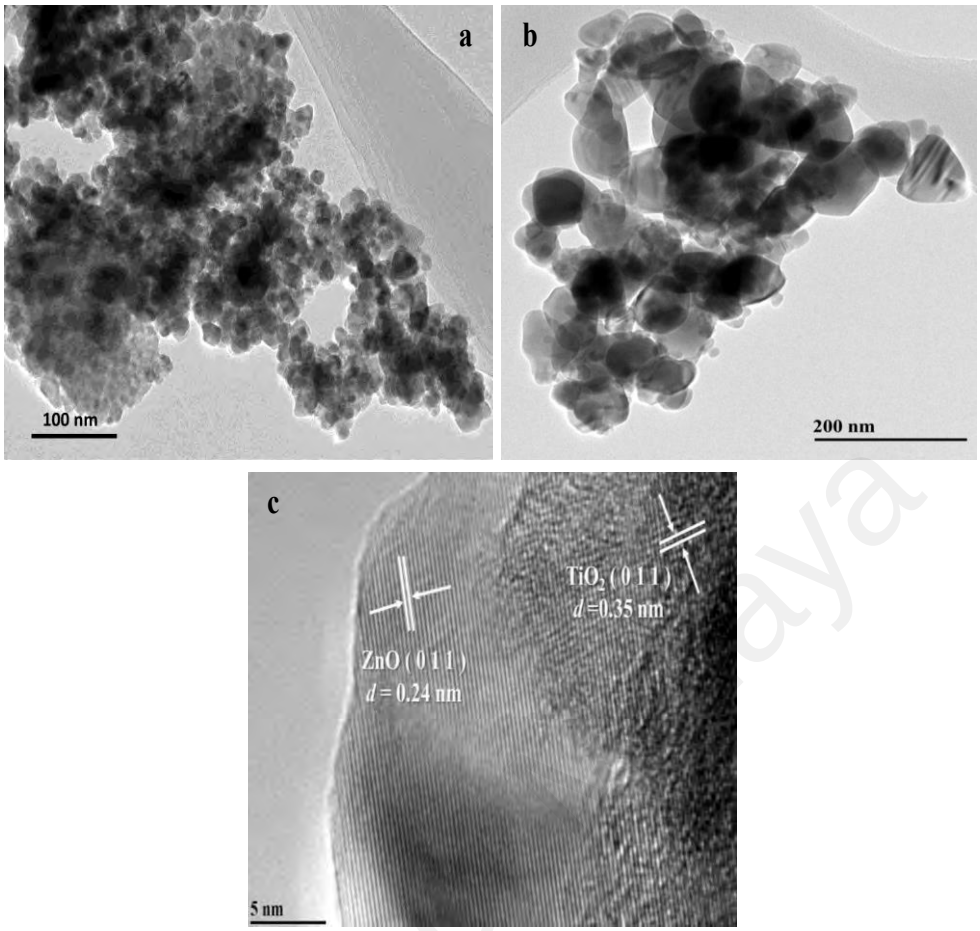

Figure 4.7: (a) TEM image of 3%Cu-TiO_2 nanoparticle, (b) TEM, and (c) HR-TEM images of the 3% Cu-TiO_2/30% ZnO nanocomposite.

The EDX was performed to analyze the chemical constituents of the prepared samples. Figure 4.8a shows the EDX spectrum of the 3% Cu-TiO_2 nanocrystals, which indicates the presence of Ti, Cu, and O in the 3% Cu-TiO_2 sample. Zn is detected in the 3% Cu-TiO_2/30% ZnO sample (Figure 4.8b). The elemental compositions of the 3% Cu-TiO_2 and 3% Cu-TiO_2/30% ZnO nanocomposites are presented in Table 4.1. The structural integrity of the two components and the distinct structure of the binary composites strongly suggested that these nanocomposites could be an effective photocatalyst for MO photodegradation with improved photocatalytic activity and stability.

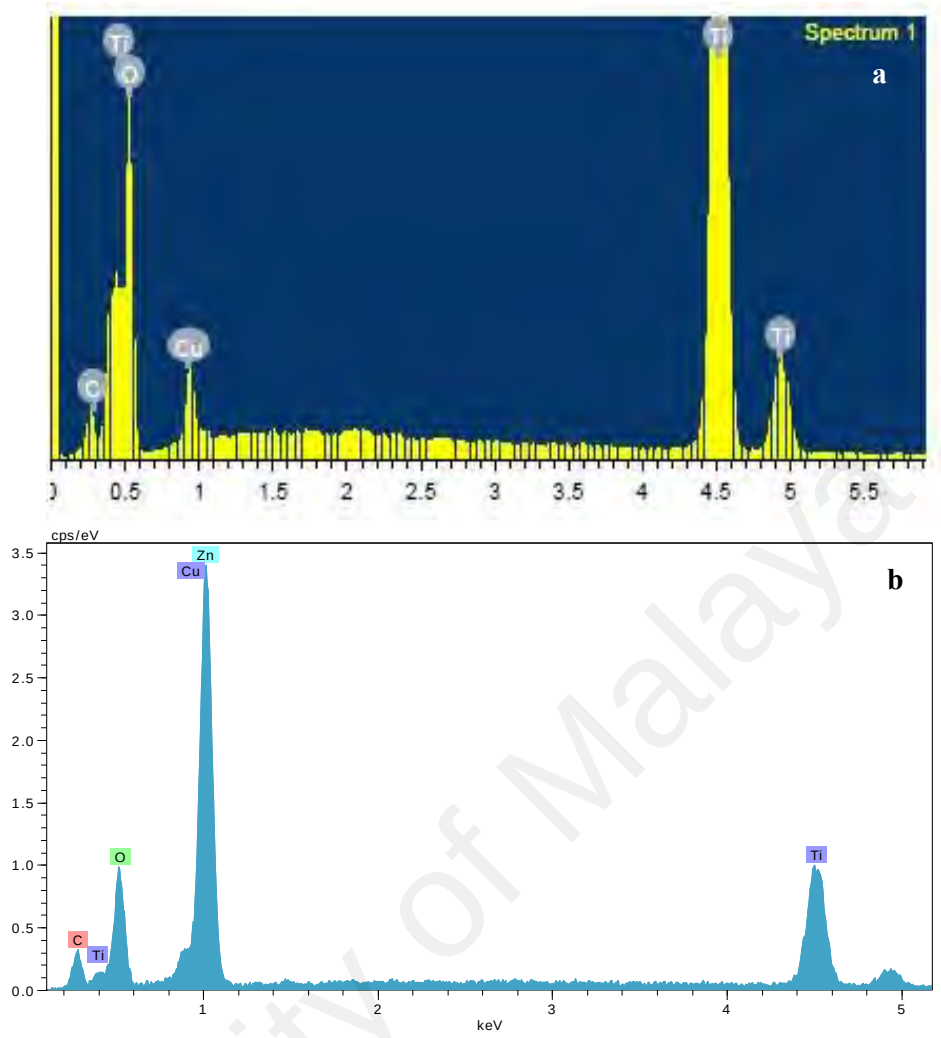

Figure 4.8: EDX spectrum images for (a) 3%Cu-TiO_2, and (b) 3% Cu-TiO_2/30%ZnO samples.

Table 4.1: Elemental compositions of the as-prepared 3%Cu-TiO_2 and 3%Cu-TiO_2/30%ZnO samples.

Sample		C	O	Ti	Cu	Zn
Cu-TiO_2	**Wt%**	2.25	42.75	48.26	6.47	-
	Atomic%	5.27	66.96	25.24	2.55	-
Cu-TiO_2-ZnO	**Wt%**	9.31	17.53	21.39	1.61	50.17
	Atomic%	24.92	35.23	14.36	0.81	24.68

4.1.5 Diffuse Reflectance UV-vis spectroscopy

Figure 4.9 shows the absorption spectra of the pure TiO_2, ZnO, and Cu–TiO_2 nanoparticles with different Cu doping contents and 3% Cu–TiO_2/30% ZnO

nanocomposites with different zinc oxide contents. The spectrum of pure TiO_2 shows an absorption edge at around 350 nm. However, no apparent absorption is observed in the visible light region.

After Cu doping, two strong absorption peaks are observed at around 450 and 750 nm. The absorption at around 450 nm is due to the electronic transition from the Cu 3d states to the CB of TiO_2 while the absorption at 750 nm is due to the electronic transition from the VB of TiO_2 to the Cu-3d states (Jaiswal et al., 2015). The absorption intensity is further increased by increasing the doping amount of Cu, which is in good agreement with the literature (Aguilar et al., 2013; Pham et al., 2015).

The light absorption of the TiO_2 spectra shows no significant change with ZnO introduction. These optical properties supported the HR-TEM results (Figure 4.7c), which show the coupling of ZnO on the TiO_2 surface; nevertheless, the TiO_2 band structures exhibited no change, although Cu doping in the TiO_2 lattice could generate impurity states in the TiO_2 band gap (Aguilar et al., 2013). However, the high ZnO contents (50% and 70% ZnO) decreases the absorption in the visible region. The strongest optical absorption at the visible light region is obtained in the 3% Cu-TiO_2/30% ZnO nanocomposite sample, which may lead to the generation of many electron–hole pairs and high photocatalytic activity of the nanocomposite.

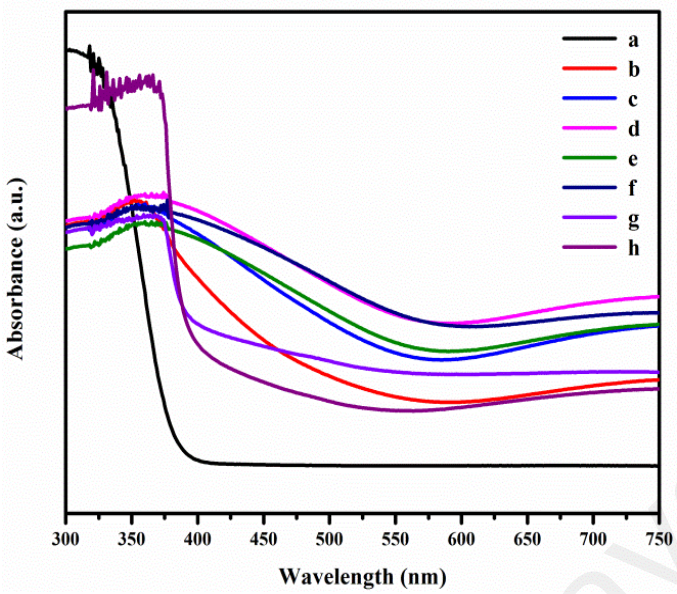

Figure 4.9: UV-vis absorption spectra of (a) TiO_2, (b) 1% Cu-TiO_2, (c) 3% Cu-TiO_2 (d) 5% Cu-TiO_2 nanoparticles, (e) 3% Cu-TiO_2/10% ZnO, (f) 3% Cu-TiO_2/30% ZnO, (g) 3% Cu-TiO_2/50% ZnO, and (h) 3% Cu-TiO_2/70% ZnO nanocomposite.

4.1.6 BET surface area measurements

The N_2 adsorption–desorption isotherms and pore-size distributions of the pure TiO_2 and 3% Cu-TiO_2 and heterostructured Cu-TiO_2/ZnO photocatalyst samples with different Ti/Zn mass ratios are presented in Figures 4.10a-f. The corresponding specific surface areas, pore volumes, and average pore sizes are summarized in Table 4.2. All samples show a type IV isotherm according to the IUPAC classification, thereby implying the presence of mesoporous structures (Hussein et al., 2013; Li et al., 2014). Copper (3% Cu–TiO_2) incorporation exerts no influence on the surface area of TiO_2 (45.19 m^2/g). The ZnO (10% and 30%) incorporation slightly decreases the surface to 42.72 and 39.45 m^2/g, respectively. Furthermore, at the Ti/Zn mass ratio of 50% and 70%, the surface area is significantly small at 15.70 and 13.17 m^2/g, respectively. In addition, the average pore size and total pore volume decreases with increasing ZnO content. A ZnO excess may block the pores of the heterostructured photocatalyst samples.

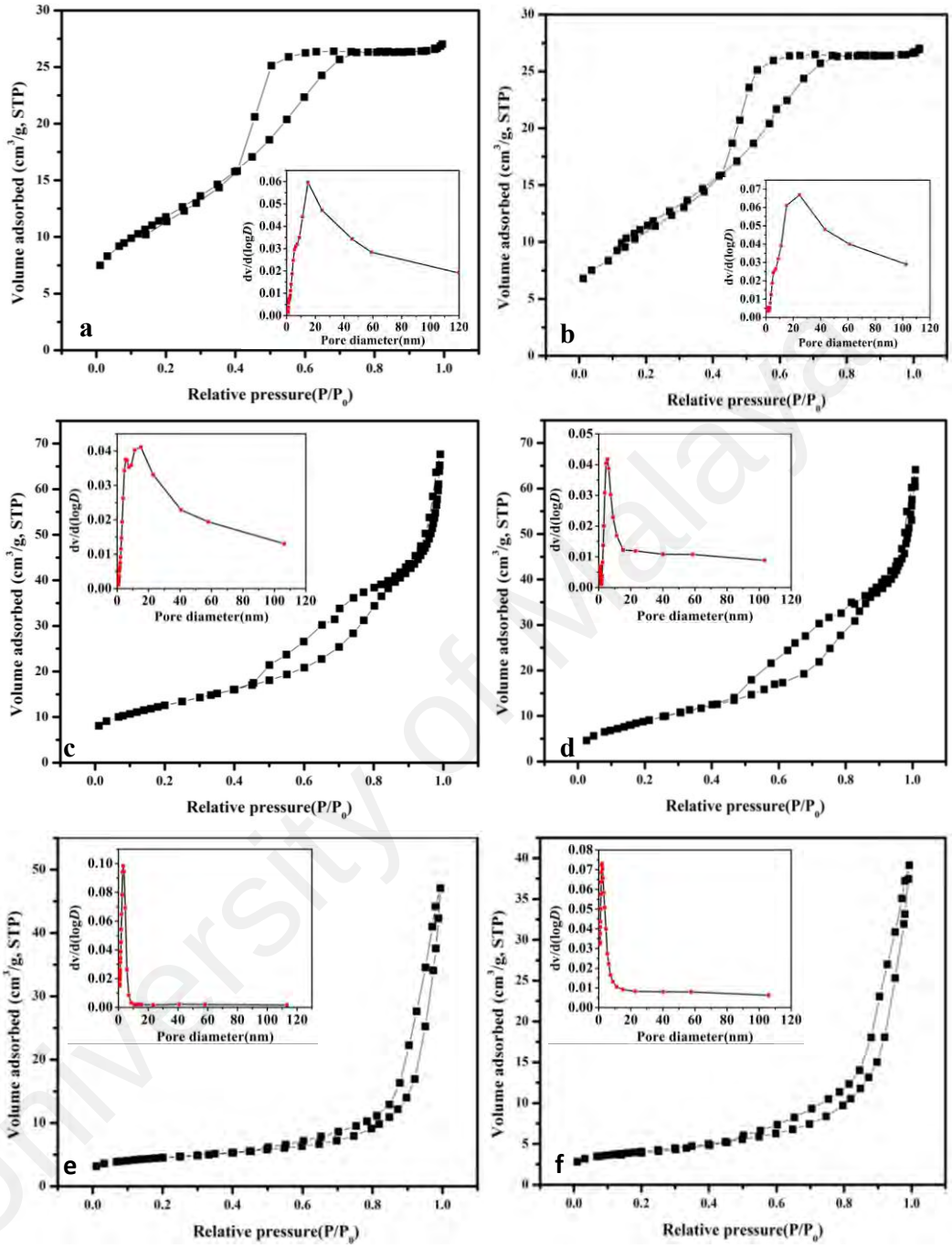

Figure 4.10: N_2 adsorption/desorption isotherms and pore-size distributions of (a) TiO_2, (b) 3%Cu-TiO_2, (c) 3%Cu-TiO_2/10%ZnO, (d) 3%Cu-TiO_2/30%ZnO,(e) 3%Cu-TiO_2/50%ZnO, and (f) 3%Cu-TiO_2/70%ZnO samples.

Table 4.2: The surface parameters of various samples from BET measurements.

Samples	BET surface area (m^2/g)	Pore size (nm)	Pore volume (cm^3/g)
TiO_2	45.19	17.00	0.072
3% Cu-TiO_2	45.97	18.40	0.0605
3% Cu-TiO_2/10%ZnO	42.72	13.50	0.0565
3% Cu-TiO_2/30%ZnO	39.45	9.20	0.0476
3% Cu-TiO_2/50%ZnO	15.70	5.20	0.0452
3% Cu-TiO_2/70%ZnO	13.17	4.00	0.041

4.1.7 Photocatalytic activity

Figure 4.11a demonstrates the photodegradation activity of all ZnO nanocomposite catalysts in the decomposition of MO dye in aqueous solution under visible light irradiation. As shown in Figure 4.11a, the MO concentration shows no significant changes prior to the visible light irradiation. However, during the 60-min visible light irradiation, the photocatalytic activity declines in the order of 3% Cu-TiO_2/30% ZnO >3 % Cu-TiO_2/10% ZnO >3% Cu-TiO_2/50% ZnO >3% Cu-TiO_2/70% ZnO. All the nanocomposite samples show higher activity than that of the pure TiO_2, but only the 3% Cu-TiO_2/10% ZnO and 3% Cu-TiO_2/30% ZnO nanocomposites show better activity than that of 3% Cu-TiO_2. Comparison of the photocatalytic activity of the pure TiO_2, 3% Cu-TiO_2, and 3% Cu-TiO_2/30% ZnO is shown in Figure 4.11b. This result showed that the 3% Cu-TiO_2-30% ZnO presents higher photocatalytic activity than that of the bare TiO_2 and 3% Cu-TiO_2 from the start (20 min) until the end of irradiation (60 min). The bare TiO_2 shows negligible visible light activity because of its wide band gap, whereas the introduction of ZnO into 3% Cu-TiO_2 improves the photocatalytic activity of the coupled nanocomposite. Notably, the photocatalytic activities of TiO_2 and 3% Cu-TiO_2 were also unchanged in the dark.

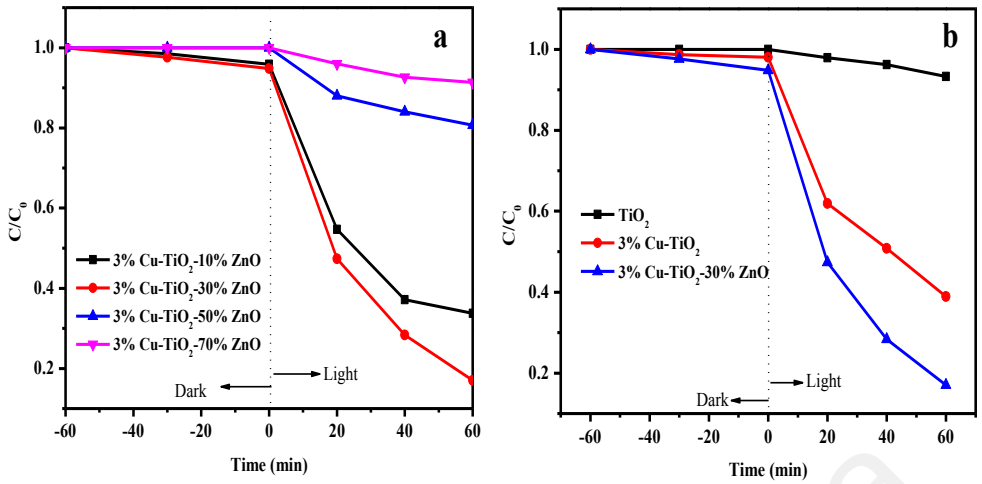

Figure 4.11: (a) Photo-degradation activity of MO by 3% Cu-TiO_2/10% ZnO, 3% Cu-TiO_2/30% ZnO, 3% Cu-TiO_2/50% ZnO, and 3% Cu-TiO_2/70% ZnO nanocomposites (b) Comparison of the photocatalytic activity of TiO_2, 3% Cu-TiO_2 nanoparticles, and 3% Cu-TiO_2-30% ZnO nanocomposite.

The degradation efficiency of MO reaches 83% and 61% in the presence of 3% Cu-TiO_2/30% ZnO nanocomposite and 3% Cu-TiO_2 nanoparticles after 60 min of irradiation time, respectively (Figure 4.12). This result suggests that the 3% Cu-TiO_2/30% ZnO nanocomposite exhibits excellent photocatalytic performance during organic pollutant degradation.

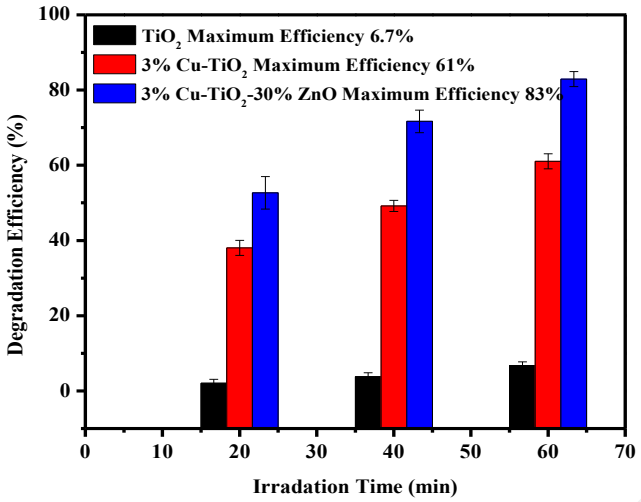

Figure 4.12: Degradation efficiency of TiO_2, 3%Cu-TiO_2 nanoparticles, and 3% Cu-TiO_2/30% ZnO nanocomposites on the photodegradation of MO with time.

The degradation kinetics of MO was also studied under visible light irradiation. Figure 4.13 shows a linear relationship between ln (C_0/C) and reaction time, which indicated that the degradation kinetics of MO follows a pseudo-first-order rate law. The apparent rate constants are 0.0011 (± 5.037 × 10^{-5}), 0.0166 (± 0.00121), and 0.0306 (± 0.00121) min^{-1} for TiO_2, 3% Cu-TiO_2, and 3% Cu-TiO_2/30% ZnO, respectively. The decreasing order of the rate constants is as follows: 3% Cu-TiO_2/30% ZnO > 3% Cu-TiO_2 > TiO_2. The photocatalytic activity of the 3% Cu-TiO_2/30% ZnO nanocomposite is approximately 2-fold higher than that of 3% Cu-TiO_2 nanoparticles and 28-fold higher than that of bare TiO_2.

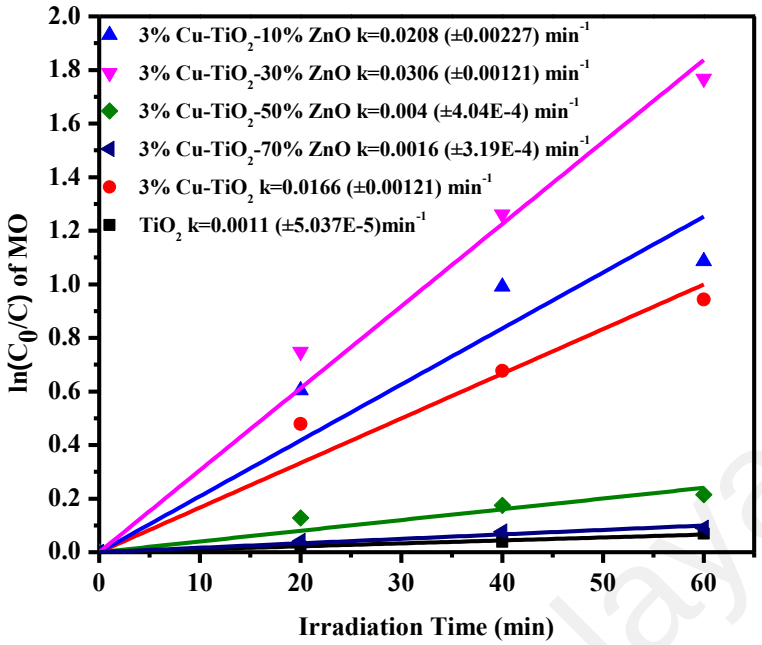

Figure 4.13: Plot of ln(C_0/C) vs. time of MO degradation for the TiO_2, 3% Cu-TiO_2 nanoparticles, 3% Cu-TiO_2/10% ZnO, 3% Cu-TiO_2/30% ZnO, 3% Cu-TiO_2/50% ZnO, and 3% Cu-TiO_2/70% ZnO nanocomposites.

Analyses showed that the samples with larger surface areas (3% Cu-TiO_2 and 3% Cu-TiO_2/10% ZnO) show no remarkable photocatalytic performance, which suggested that the total surface area of the material exerts no significant influence on the photocatalytic performance (Yang et al., 2016). The PL and UV–vis spectroscopic results demonstrated that the 3% Cu-TiO_2/30% ZnO sample possesses the lowest PL intensity and strongest optical absorption at the visible light region compared to the other samples. The low PL intensity of 3% Cu-TiO_2/30% ZnO nanocomposite could have resulted in enhanced photocatalytic activity, which can be ascribed to the effective charge separation of the photogenerated carriers. Thus, the 3% Cu- TiO_2/30% ZnO sample exhibited the highest photocatalytic activity.

To examine the stability and reusability of the 3% Cu-TiO_2/30% ZnO nanocomposite as a photocatalyst, recycling runs for MO photodegradation under visible light irradiation were also performed. As shown in Figure 4.14a, the photocatalytic behavior

of 3% Cu-TiO_2/30% ZnO nanocomposite shows a slight decrease in activity over three cycles. The degradation efficiency of the nanocomposites during MO photodegradation after the first, second, and third cycles is 79.3%, 75%, and 68.4%, respectively (Figure 4.14b). These results indicate that the 3% Cu-TiO_2-30% nanocomposite photocatalyst shows only a slight decrease in the photocatalytic activity during the three runs. Thus, the nanocomposite is stable and activated during the organic dye photodegradation process. These properties are remarkably important in industrial applications.

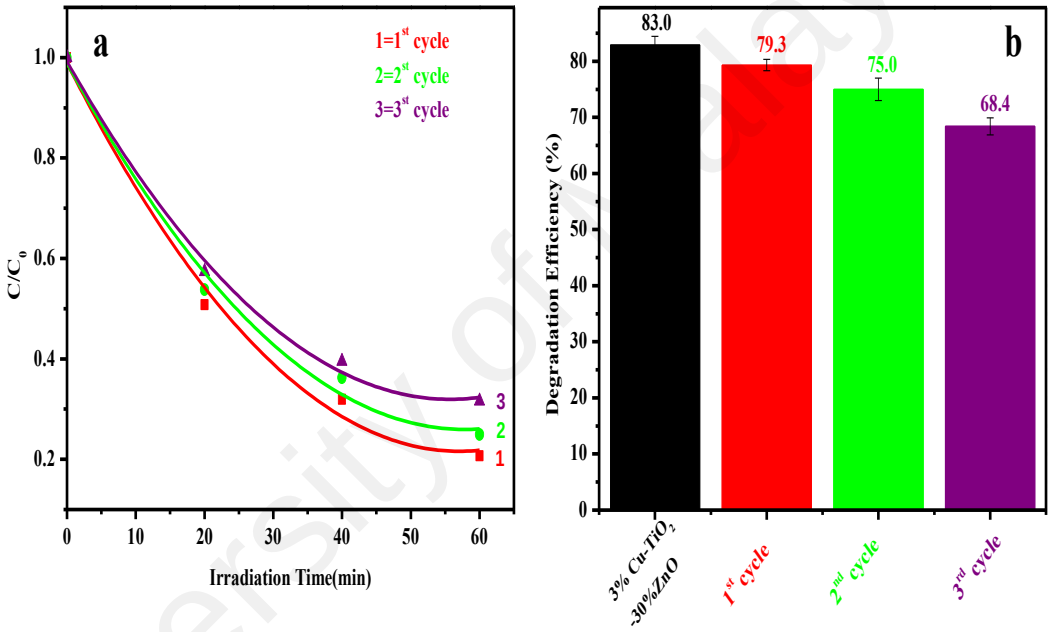

Figure 4.14: (a) Recyclability of the photocatalytic decomposition of MO for 3% Cu-TiO_2/30% ZnO nanocomposite under visible light, and (b) Percent degradation efficiency of 3% Cu-TiO_2/30% ZnO nanocomposite with increasing number of catalytic cycle.

4.1.8 Detection of reactive oxidative species

To investigate the possible photodegradation mechanisms, the different reactive species formed during organic pollutant degradation were confirmed by the radical and hole trapping experiments. The three radical scavengers, namely, *tert*-butyl alcohol (TBA,1 mM), ammonium oxalate (AO, 1 mM) and benzoquinone (BQ, 1 mM), were

utilized to trap the photogenerated hydroxyl radical ($OH^{\bullet}$), hole (h^{+}) and superoxide anion radical ($^{\bullet}O_2^{-}$), respectively (Tan et al., 2017; Zheng et al., 2015). As shown in Figure 4.15, the MO degradation efficiency of 3% Cu-TiO_2/30% ZnO is slightly inhibited upon the BQ addition. This result implies that the presence of the $^{\bullet}O_2^{-}$ anion radical is insignificant during the MO decomposition under visible light irradiation. By contrast, the photodegradation rates of MO are distinctly suppressed in the presence of the TBA or AO, which indicates that the $OH^{\bullet}$ and h^{+} are the major active species in the photocatalytic reaction pathways.

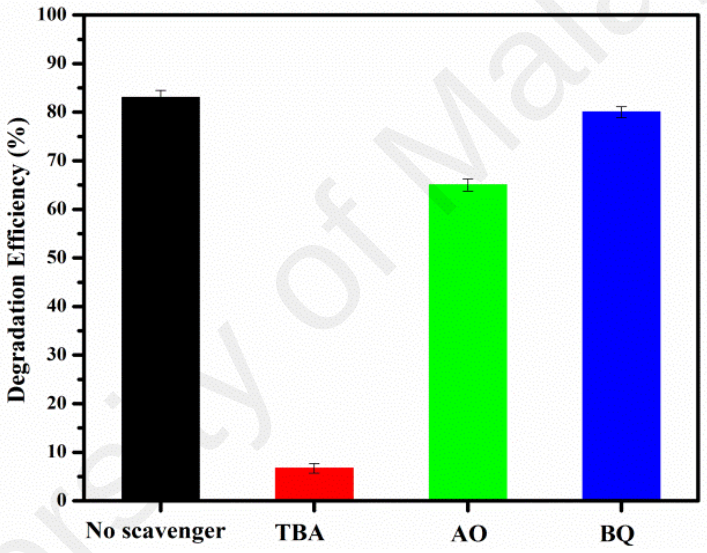

Figure 4.15: The effect of different scavengers on the photocatalytic degradation of MO over 3% Cu-TiO_2/30% ZnO nanocomposite under visible light illumination (TBA: tert-butyl alcohol; AQ: ammonium oxalate; BQ: benzoquinone).

4.1.9 Possible photocatalytic mechanism

To describe the mechanisms of enhanced photocatalytic activity of the Cu-TiO_2/ZnO nanocomposites under visible light irradiation, the corresponding potentials of the CB and VB of TiO_2 and ZnO semiconductors were estimated using the following equations (Jiang et al., 2016):

$$E_{CB} = X - E_0 - 0.5E_g \quad \text{(Equation 4.1)}$$

$$E_{VB} = E_{CB} + E_g \quad \text{(Equation 4.2)}$$

where X is the electronegativity of the semiconductor obtained from the geometric mean of the electronegativity of its constituent atoms (X values for TiO_2 and ZnO are 5.8101 and 6.3246, respectively (Tan et al., 2017; Zheng et al., 2015), and E_0 is the energy of free electrons on the hydrogen scale (4.5 eV). The experimental optical band gap energies of TiO_2 and ZnO were determined from the plots of $(\alpha hv)^n$ vs. hv (Figures 4.16a and b) and estimated as 3.2 and 3.3 eV, respectively. The n value depends on the electronic transition of the semiconductor ($n_{indirect}$= 1/2; n_{direct}= 2), where the n value is 1/2 and 2, respectively. Therefore, the E_C potentials of TiO_2 and ZnO are −0.29 and 0.17 eV, and the E_V potentials are 2.91 and 3.47eV, respectively.

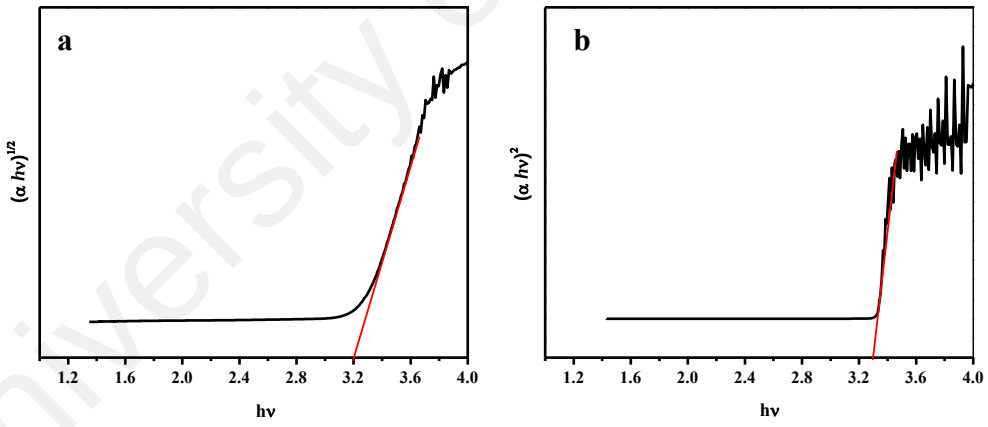

Figure 4.16: Tauc plot obtained from UV-vis spectra for (a) TiO_2 and (b) ZnO.

Based on the results, the photocatalytic degradation mechanism of MO on Cu-TiO_2/ZnO nanocomposite is proposed and presented in Figure 4.18. The VB and CB of pure TiO_2 comprise of the Ti (3d) and O (2p) states, respectively. When Cu ions are doped into the TiO_2 lattice, the isolated levels are formed above the uppermost part of the VB because of the Cu-3d orbital, which shifts the VB maximum to high energy

values; consequently, the band gap decreases (Chang & Liu, 2014). The Cu-TiO_2 band gap energy was obtained by extrapolating the Tauc plot of $(\alpha h\nu)^{1/2}$ to the $h\nu$ axis (Figure 4.17), and the value is close to the reported values (Aguilar et al., 2013; Jaiswal et al., 2015). Thus, under visible light irradiation, Cu-TiO_2 could be excited to produce electrons in the CB and holes in the VB simultaneously because of its visible light response.

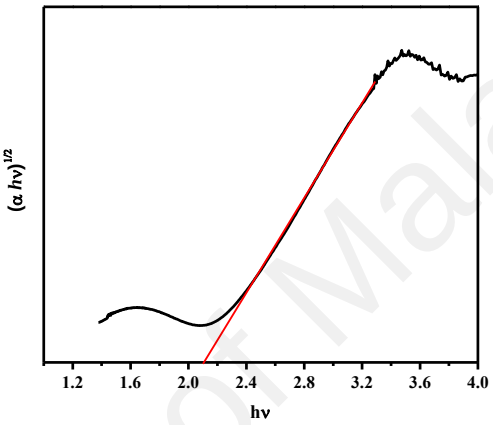

Figure 4.17: Tauc plot obtained from UV-vis spectra for 3%Cu-TiO_2.

On the contrary, ZnO hardly generates electron–hotel pairs due to the large band gap energy (3.3 eV). Given that the CB potential of TiO_2 (−0.29 eV) is more negative than that of ZnO (0.17 eV), the photogenerated electrons easily migrate from the CB of TiO_2 to the CB of ZnO. The photogenerated holes tend to exist in the VB of TiO_2. This behavior efficiently inhibits the recombination of electron and holes, thereby enhancing the photocatalytic activity of Cu-TiO_2/ZnO heterojunction photocatalyst. The photoinduced electrons injected in the CB of ZnO could not combine with O_2 to generate $^{\bullet}O_2^-$ because the CB potential of ZnO is more positive than that of the $O_2/^{\bullet}O_2^-$ redox couple (−0.33 eV/vs. NHE) (Jiang et al., 2012), which also accounts for the minor reactive species of the $^{\bullet}O_2^-$ in the trapping experiment (Figure 4.15). Furthermore, the holes generated from the VB of TiO_2 could oxidize OH^- and H_2O to produce $OH^{\bullet}$

because of the higher VB potential of TiO_2 than those of the $OH^{\bullet}/OH^{-}$ (+2.38 eV/vs. NHE) and $OH^{\bullet}/H_2O$ (+2.72 eV/vs. NHE) (Mousavi & Habibi-Yangjeh, 2016). This result suggests that the holes (h^{+}) and hydroxyl radicals ($OH^{\bullet}$) are the main reactive species involved in MO photodegradation. In addition, this result was confirmed by the former active species trapping experiments (Figure 4.15). Hence, the heterostructured semiconductors could effectively decrease the charge recombination and subsequently enhance the photocatalytic activity of the Cu-TiO_2/ZnO system.

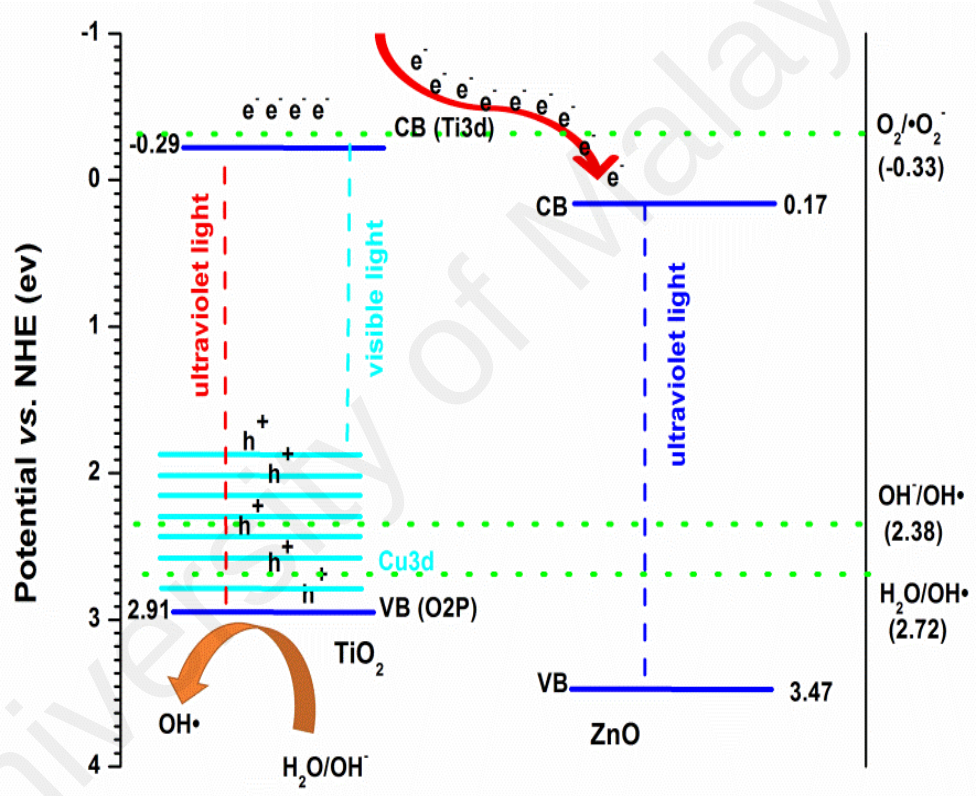

Figure 4.18: Schematic diagram of the proposed photocatalytic mechanism and the photogenerated charge-transfer process in Cu-TiO_2/ZnO heterostructured nanocomposites.

4.2 Improved visible light photocatalytic activity of TiO_2 co-doped with copper and iodine

TiO_2 has received considerable attention as an ideal photocatalytic material for the degradation of organic contaminants from wastewater or gas phase due to its high photoactivity, good photostability, cost effectiveness, and environmental friendliness (Jaiswal et al., 2015; Wang et al., 2016). Unfortunately, the poor capability of TiO_2 to absorb visible light as the main part of solar spectrum has limited its large-scale industrial applications (Zheng et al., 2016). For increased utilization of sunlight, various modifications have been made to the crystal structure of TiO_2-based materials, such as metal doping or nonmetal element doping (Ganesh, 2017; Hu et al., 2017), coupling (Low et al., 2017), and co-catalyst modification (Wang et al., 2017) for the enhanced absorption of sunlight. Among them, ion doping (either metal or nonmetal) is considered as a simple and effective modification method that has been undertaken by several research groups to extend the light absorption from UV to the visible region (Akple et al., 2015) .

In general, the dopant ions in the TiO_2 lattice introduce mid-gap energy states at the top of the valence band or at the bottom of the conduction band of TiO_2, which extends its absorption band edge from the UV to the visible-light region (He et al., 2017; Kong et al., 2017; Yu et al., 2016; Zhang et al., 2017; Zhou et al., 2014). These as-produced impurity energy levels can also function as a trapping center for the effective separation of the photogenerated electron–hole pairs, thus leading to increased photocatalytic activity (Wu et al., 2013). However, these dopant ions must be utilized in small quantities to prevent subsequent recombination of electrons and holes. Low concentration doping causes only a slight red shift of the optical absorption edge to the visible-light region, which is insufficient for the effective utilization of visible solar light (Jaiswal et al., 2015; Jaiswal et al., 2012). Considering the increased doping

concentration, the impurity levels act as electron–hole pair recombination sites that cause a negative effect on the photocatalytic activity (Bensouici et al., 2017; Dong et al., 2015). In other words, extending the absorption edge to the visible region at the same time to prevent electron–hole recombination is a challenging task.

Recently, co-doping with two different types of ions has become a highly useful approach to improve the visible light-driven photocatalytic activity of TiO_2. In such system, the synergic combination of different types of dopants not only enhances the absorption of visible light but also decreases the photogenerated charge carrier recombination (Jaiswal et al., 2016; Zheng et al., 2016). The N and C nonmetal dopants in TiO_2 have been widely utilized as co-dopants with various metals, hence forming combinations such as Fe–N (Su et al., 2011), W–N (Zheng et al., 2016), Cr–N (Li et al., 2011), Cu–N (Jaiswal et al., 2015), Co–B (Jaiswal et al., 2016), Cr–C (Li et al., 2017), and Nd–C (Wu et al., 2013).

Among the various nonmetals, I is the least studied co-dopant in the presence of metal dopants. In contrast to other nonmetal dopants, I^{5+} is an efficient substituent in the TiO_2 lattice due to its similar ionic radii with Ti^{4+} (Wang et al., 2016). From the density functional theory of iodine doped TiO_2, it can be concluded that substituted iodine could induce defects in the TiO_2 lattice and subsequently improve photocatalytic activity under the visible-light spectrum (Long et al., 2009). In addition, Tojo et al. (2008) reported that the I^{5+} ions in the TiO_2 lattice are trapping sites for electrons upon reduction to I^- ions. This phenomenon contributes to the efficient electron–hole pair separation. Moreover, iodine dopant atoms have been preferred to be located close to the TiO_2 surface, hence the surface doped I^{5+} functions as a trap site for the photogenerated electron and accelerates the electron transfer process to the catalyst

surface, thus increasing the photocatalytic activity (Liu et al., et al., 2009; Tojo et al., 2008).

Few efforts have focused on the co-doped transition metals with I e.g., I-Zr-co-doped TiO_2 (Song et al., 2011), which have resulted in superior photocatalytic activity compared to the mono-doped and un-doped TiO_2 for methyl orange (MO) degradation. Recently, Jaiswal et al. (2015) reported a significant narrowing of the TiO_2 band gap into the visible region due to the incorporation of Cu^{2+} ions in the TiO_2 lattice. Moreover, a theoretical study on the effect of Cu doping on the photocatalytic activity of TiO_2 demonstrated that the doping of the Cu^{2+} ions in TiO_2 lattice results in the inter-band gap states, which are considered responsible for the improved visible-light photoactivity of doped TiO_2 (Assadi & Hanaor, 2016). Furthermore, the energy levels formed by Cu^{2+} act as hole-trapping sites, thereby decreasing the rate of electron–hole pair recombination (Dorraj et al., 2017). Therefore it is possible to achieve a highly efficient visible light-driven photo-catalyst by the co-doping of Cu and I in the TiO_2 lattice from the synergic effects of metal and nonmetal dopants described earlier.

To the best of our knowledge, the Cu and I co-doped TiO_2 was synthesized for the first time via the hydrothermal method in this study. The effect of calcination temperature on the catalytic activity and the synergism of the Cu and I co-dopants were subsequently investigated in the photo-degradation of MO.

4.2.1 XRD analysis

Figure 4.19 shows the XRD patterns of the mono-doped Cu and I, TiO_2 samples calcined at 350 °C, together with the Cu and I co-doped TiO_2 calcined at various temperatures (350–550 °C). The undoped, mono-doped and co-doped TiO_2 samples consist of mainly two different phases, namely, the anatase (main peak: $2\theta_{(011)} = 25.5°$) and rutile (main peak: $2\theta_{(110)} = 27.5°$). Evidently, the XRD patterns showed no traces of

the Cu or I species. This result indicates that the Cu and I ions substituted the Ti^{4+} and are incorporated into the TiO_2 lattice, owing to the similar ionic radii of Cu^{2+} and I^{5+} with Ti^{4+} (Bagwasi et al., 2012; Hanaor & Sorrell, 2011).

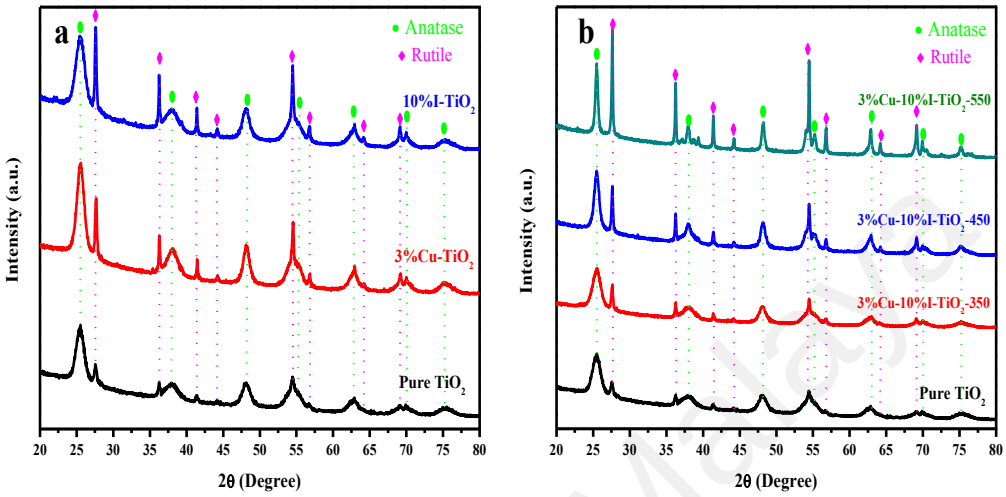

Figure 4.19: XRD patterns of (a) pure TiO_2, 3% Cu-TiO_2 and 10% I-TiO_2 (b) 3%Cu-10% I-TiO_2 at different calcination temperatures.

The phase compositions of the samples are summarized in Table 4.3. The rutile peak intensity increases with the dopant incorporation in the lattice (Figure 4.19a), thus demonstrating the presence of the dopant ion in the TiO_2 lattice that is responsible for the phase transformation from the anatase to the rutile phase (Hanaor & Sorrell, 2011). This phenomenon is so effective in I mono-doping (Figure 4.19a and Table 4.3). Unlike the single ion doped TiO_2, the phase content of the pure TiO_2 is almost preserved after co-doping in 3% Cu-10% I-TiO_2 for the sample at 350 °C (Table 4.3). This result is in close agreement with other studies, which indicates that the interaction between both elements from co-doping may inhibit the phase transition of the anatase to the rutile phase through the decrease of oxygen vacancies (Jaiswal et al., 2016).

When the calcination temperature increases, the anatase phase gradually transforms to the rutile phase (Figure 4.19b and Table 4.3). Then, the portion of the anatase phase

decreases dramatically while the rutile phase increases. This is in close agreement with the literature, where the increase in the calcination temperature increases the rutile phase but decreases the composition of the anatase phase (Kordouli et al., 2015).

Table 4.3: The characteristics of the prepared samples including phase content and crystallite size.

Sample	Phase contents (%)		Crystal size (nm)	
	A	R	A011	R110
Tio_2-350	87	13	6.8	29
3%Cu-TiO_2-350	82.2	17.8	7.3	32.6
10%I-TiO_2-350	76.8	23.2	6.2	33
3%Cu-10%I-TiO_2-350	86	14	6.7	31
3%Cu-10%I-TiO_2.450	80	20	10.5	37
3%Cu-10%I-TiO_2-550	55	45	19.5	43.4

The X-ray diffraction patterns of the anatase and rutile phases in the co-doped samples display broad peaks related to the smaller size of the nanoparticles at lower calcination temperature; whereas the sharp peaks indicate the large size of the nanoparticles at higher calcination temperatures (Figure 4.19b). The average particle sizes of anatase and rutile were calculated at each temperature by using the Debye–Scherrer equation, from the main peaks of the two crystallographic forms (Table 4.3). These values show that the crystallite size of the anatase phase increases from 6.7 nm to 19.5 nm, together with the increase in crystallite size of the rutile phase from 31 nm to 43.4 nm, in the co-doped samples at temperature between 350 °C to 550 °C.

At a calcination temperature of 350 °C (Figure 4.19a), the mono-doped TiO_2 shows an almost unchanged crystallite size of anatase approximately 6 nm (Table 4.3). In contrast, the rutile crystallite size increases as narrow reflections are observed in the rutile phase.

4.2.2 Raman analysis

Raman spectroscopy was utilized to study the crystalline structure of the photocatalyst samples, as shown in Figure 4.20. All samples show prominent fundamental bands for the anatase phase at 143 (Eg), 197 (Eg), 395 (B1g), 517 (A2g), and 637 (Eg) cm^{-1}, together with a peak of approximately 442 (Eg) cm^{-1} corresponding to the rutile phase (Jaiswal et al., 2016). The Raman peak intensity of the rutile phase increases slightly after doping with Cu or I (Figure 4.20a). This finding indicates an increased formation of the rutile phase, which is in line with the results of XRD. The same trend was observed for the rutile phase in the co-doped samples at increased temperatures (Figure 4.20b). The Raman spectroscopic investigations confirm that the hydrothermally prepared samples of undoped TiO_2, mono-doped, and co-doped TiO_2 are of high purity and crystallinity. These results are in agreement with the XRD measurements, and confirm the successful doping of Cu and I into the TiO_2 lattice.

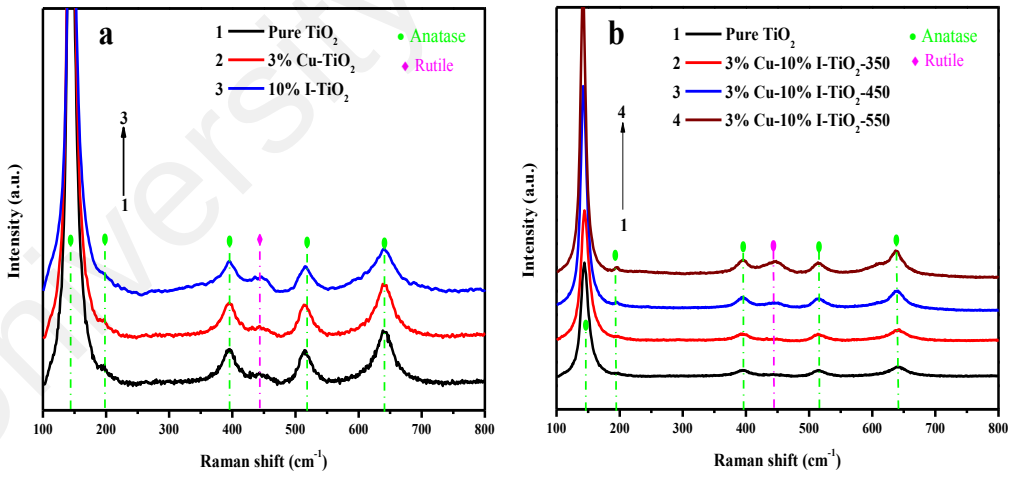

Figure 4.20: Raman spectra of (a) pure TiO_2, 3% Cu-TiO_2 and 10% I-TiO_2 (b) 3% Cu-10% I-TiO_2 at different calcination temperatures.

4.2.3 Morphological analysis

The morphologies of the co-doped samples after thermal treatment at 350 °C, 450 °C and 550 °C were investigated by FESEM (Figure 4.21). The anatase nanoparticles are quasi-spherical, whereas the rutile particles are large and elongated. The rutile morphology changed from rod-shaped at 350 °C to brick-shaped at 450 °C and 550 °C. The size of the anatase-rutile particle grows larger as the rutile fraction in the co-doped sample increases. Calcination inevitably causes an increase in the size of particles but a decrease in the surface area.

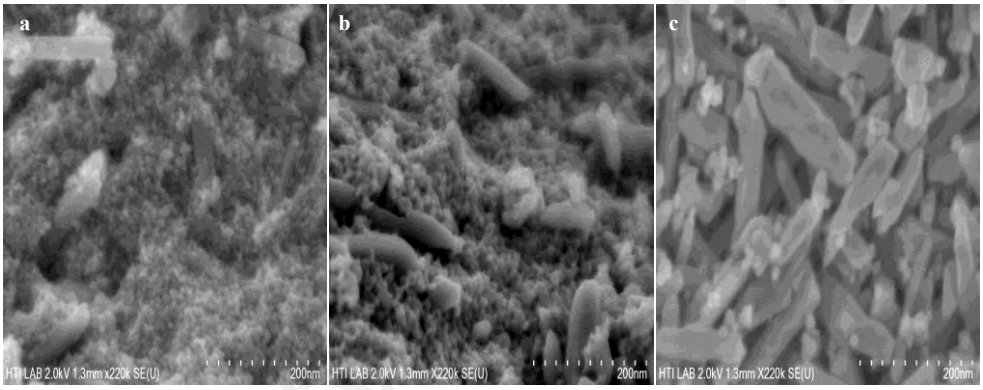

Figure 4.21: FESEM images of (a) 3% Cu-10% I-TiO_2 at 350 °C, (b) 3% Cu-10% I-TiO_2-450 °C, and (c) 3% Cu-10% I-TiO_2-550 °C.

The composition of the co-doped sample at 350 °C was further studied by EDX. Figure 4.22 confirms the presence of Ti, O, Cu and I in the co-doped nanoparticles. The EDX elemental analysis of the co-doped sample is presented in the inset of Figure 4.22. To precisely assess the final concentration of the Cu and I in the co-doped sample, the amount of dopants were quantified by ICP-MS. The estimated weight percentages of Cu and I in the co-doped sample are 2.17 and 8.89, respectively. The Cu and I contents measured by ICP are slightly lower compared to the theoretical values, which suggest that the Cu and I dopants migrated to the crystalline structures of the TiO_2.

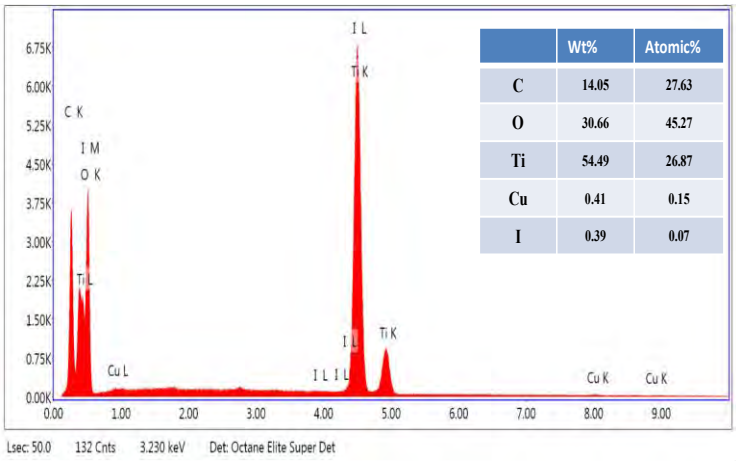

	Wt%	Atomic%
C	14.05	27.63
O	30.66	45.27
Ti	54.49	26.87
Cu	0.41	0.15
I	0.39	0.07

Figure 4.22: EDX spectrum of 3% Cu-10% I-TiO_2 at 350 °C.

Moreover, the elemental distribution in the co-doped TiO_2 calcined at 350 °C was examined by EDX elemental mapping analysis (Figure 4.23). All four components, namely Ti, O, Cu, and I, were identified and homogeneously distributed in the samples. The colored points are allocated to Cu and I components which confirms that both metal and nonmetal dopants are well dispersed at the macroscopic scale, in the titanium framework.

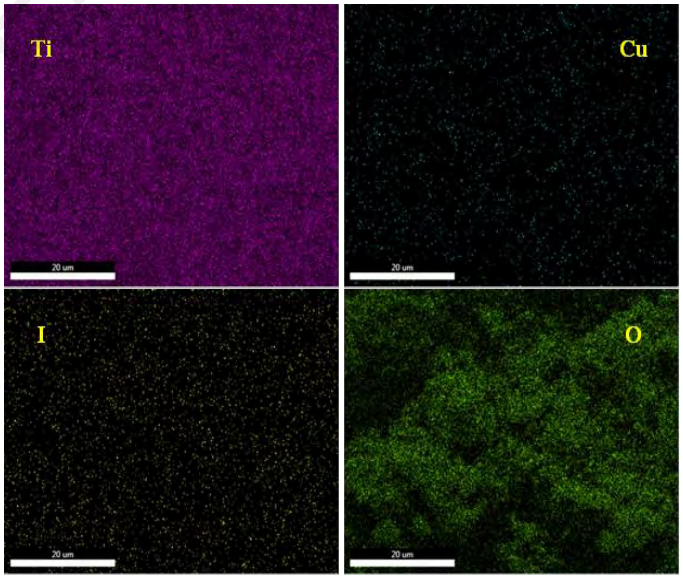

Figure 4.23: Elemental mapping of 3% Cu-10% I-codoped TiO_2 powder obtained by EDS analysis at 350 °C.

The particle size and morphology of the co-doped samples after thermal treatment at 350 °C were evaluated by TEM, as shown in Figure 4.24. Mixtures of spherical and rod-shaped nanoparticles are observed in TEM. The diameter of the spherical particles is between 5 and 8 nm; moreover, the nanorods are around 42 nm in width and 200 nm in length. The HRTEM image of the selected area (in red) in Figure 4.24a is depicted in Figure 4.24b. The image demonstrates that the spherical nanoparticles are the anatase phase [lattice spacing = 0.35 nm, corresponding to the (011) plane] while the nanorods are in the rutile phase [lattice spacing = 0.32 nm, corresponding to the (110) plane].

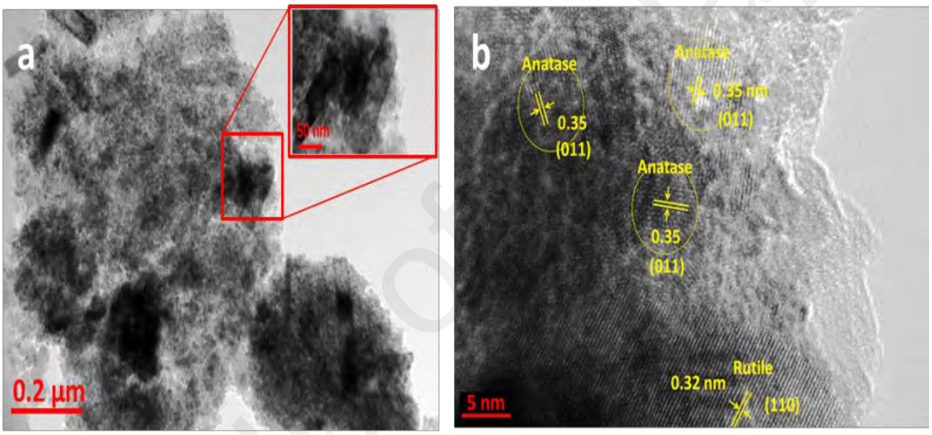

Figure 4.24: TEM image (a) and HRTEM image (b) of the 3% Cu-10% I-co-doped TiO_2 powder at 350 °C.

4.2.4 BET surface area measurements

Figure 4.25 shows a type IV N_2 adsorption–desorption isotherm for all six samples, which is a characteristic of a mesoporous material. The isotherms of the co-doped samples calcined at 450 °C and 550 °C have a similar shape and converge at a higher relative pressure compared with those of the mono-doped and pure TiO_2 calcined at 350 °C.

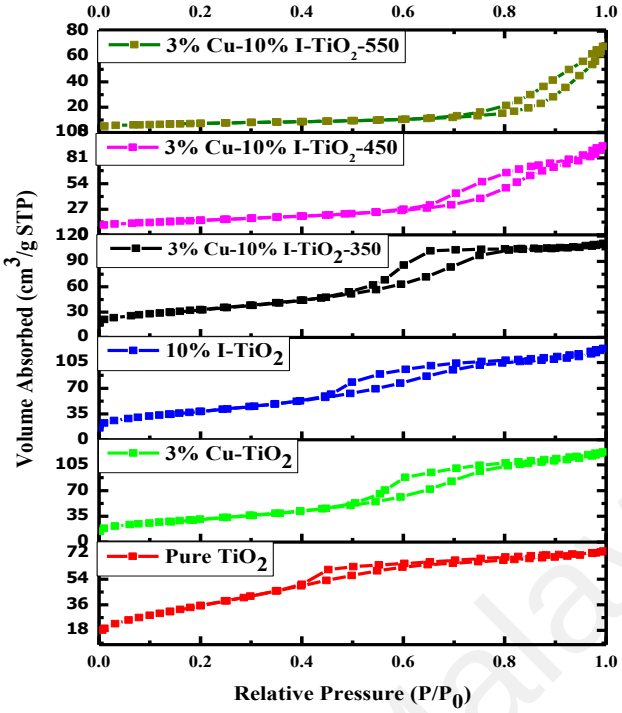

Figure 4.25: Nitrogen adsorption–desorption isotherms for the prepared TiO_2 catalysts.

Correspondingly, the calculated pore sizes of the samples with higher portion of the anatase phase are smaller than those of the higher portion of the rutile phase (Table 4.4) because the inter-particle spacing between the agglomerated anatase TiO_2 nanoparticles is smaller than those of nanorods with a higher portion of the rutile phase. Thus, the loss of small pores is responsible for the decreased surface area (Song et al., 2010). Moreover, Table 4.4 compares the specific surface areas of various TiO_2 catalysts from the BET measurements. The surface areas of the samples with the higher portion of anatase (pure TiO_2, 3% Cu-TiO_2, 10% I-TiO_2 and 3% Cu-10% I-TiO_2 calcined at 350 °C) are similar (around 135 m^2 g^{-1}) and at least twice larger than those samples with the higher portion of the rutile phase (3% Cu-10% I-TiO_2 calcined at 450 °C and 550 °C). The increase in the crystallite size and decrease in the surface area with increasing temperature are broadly reported in metal oxide nanoparticles, particularly TiO_2 (Amano et al., 2016). This similar trend is also observed here and proved by the XRD results.

Table 4.4: BET specific surface area, pore size and band gap of the prepared samples.

Sample	BET (m^2/g)	Pore size (nm)	Band gap (ev)
Tio_2-350	132.0	5.4	3.10
3%Cu-TiO_2-350	131.5	6.7	2.60
10%I-TiO_2-350	133.0	5.4	2.90
3%Cu-10%I-TiO_2-350	135.6	5.7	2.58
3%Cu-10%I-TiO_2-450	54.3	10.5	2.56
3%Cu-10%I-TiO_2-550	25.0	16.8	2.50

4.2.5 Diffuse Reflectance UV-vis spectroscopy

Figure 4.26 displays the diffuse reflectance UV-vis absorption spectra for the pure TiO_2, I-TiO_2, and Cu-TiO_2 calcined at 350 °C and Cu-I-TiO_2 samples at different temperatures (350 °C, 450 °C, and 550 °C). As can be seen, the absorption edge of pure TiO_2 sample is extended to the visible region. On the contrary, the mixed-phase TiO_2 nanocomposite absorbs greater portion of the visible light compared to the pure anatase phase. This finding indicates that the existence of the rutile significantly improves the absorption of visible light (Liu et al., 2016). Compared to the pure TiO_2, the absorption band edge shifts toward longer wavelengths with the incorporation of I into the TiO_2 lattice. This result is consistent with the theoretical calculation for iodine doped TiO_2 reported by Long et al. (2009), who claimed that the redshift in the absorption edge is due to the mixing of the I 5p with Ti 3d states, along with the movement of the O 2p states to high energy due to I^{5+} doping.

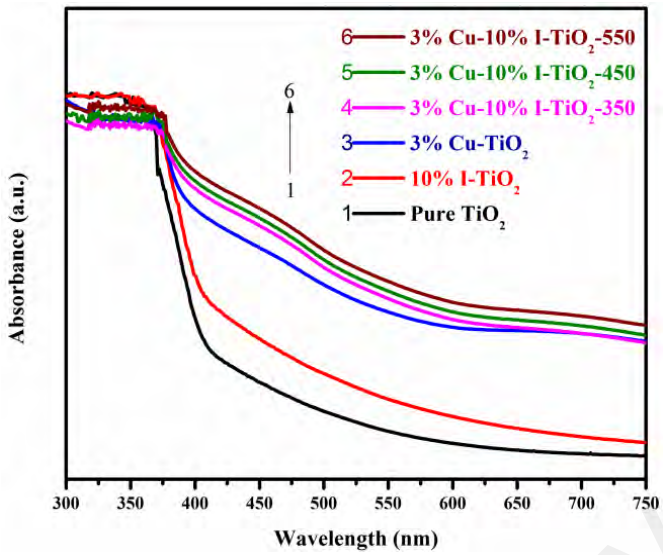

Figure 4.26: The UV-vis diffuse reflectance spectra of the prepared TiO_2 catalysts.

The Cu-doped TiO_2 revealed a notable red-shift relative to the I-doped sample. The reason for this significant band edge shift in the Cu-doped TiO_2 was described in detail in our previous work (Dorraj et al., 2017). Briefly, a high redshift in the optical absorption edges in copper doped TiO_2 was caused by the formation of *d* sub-band states above the valence band (VB) of TiO_2 from the incorporation of Cu^{2+} ions in the titanium lattice.

Upon co-doping with Cu and I, the absorption curve of the (Cu, I)-co-doped TiO_2 did not affect the optical property compared to the Cu-doped TiO_2 sample. This result suggests that the effect of copper is predominant in the co-doped composites. Almost the same amount of redshift is observed in the absorption edge of the UV-vis spectra for the co-doped TiO_2 samples at different calcination temperatures. The slight increase in the absorption edge of the co-doped samples can be attributed to a high rutile portion with increasing calcination temperatures. The rutile phase is the main reason for the large redshifted absorption bands in the visible-light region (Amano et al., 2016; Li et

al., 2009). Accordingly, the optical features of the co-doped TiO_2 suggestes that such photocatalyst might be activated by visible light.

The band gap values of all samples were calculated from the plot of $(\alpha hv)^{1/2}$ versus hv, as shown in Figure 4.27a-b, as summarized in Table 4.4. Small band gap energy could be achieved due to the extension of the photo-active range to the visible spectrum for the mono-doped and co-doped TiO_2 samples.

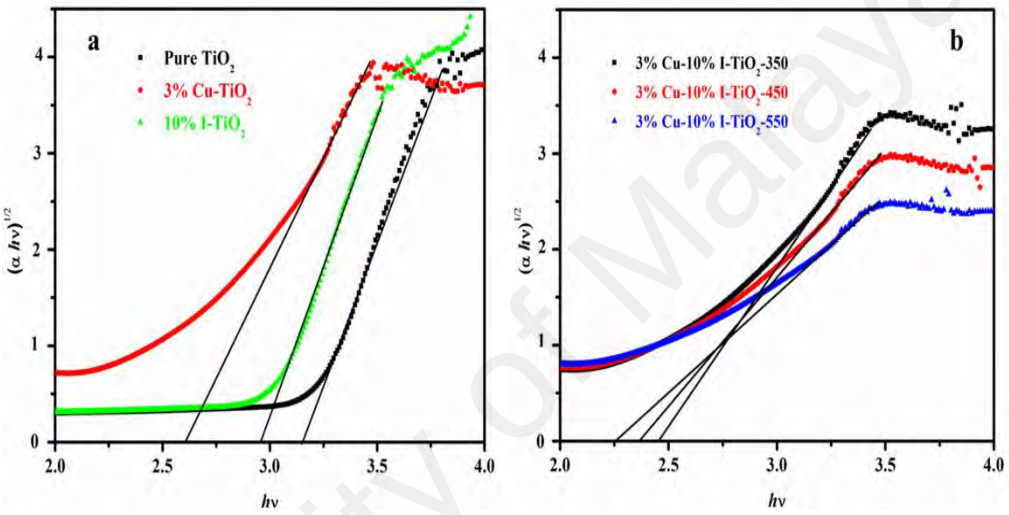

Figure 4.27: The plot of $(\alpha hv)^{1/2}$ vs. hv for the energy band gap of the prepared TiO_2 catalysts.

4.2.6 PL spectra analysis

Figure 4.28 shows the PL spectra of pure, mono-doped, and co-doped TiO_2 samples, where the spectral emissions of the samples occur at similar wavelengths but have different intensities. Compared to the pure TiO_2, the Cu- or I-doped TiO_2 showed a decrease in the emission intensity. Furthermore, the intensity was further decreased in the Cu-I-co-doped TiO_2 at 350 °C. This indicates that doping and co-doping at 350 °C suppresses the charge recombination via charge trapping in the doped Cu^{2+} and I^{5+} sites (Chang & Liu, 2014; Tojo et al., 2008). The Cu^{2+} doping close to the top of the VB is

sufficient to trap holes, whereas the I^{5+} ions close to the conduction band minimum can act as electron trapping center in the TiO_2 lattice. This phenomenon decreases the recombination process and favors the separation of the photogenerated electron–hole pairs. However, the PL intensity of the co-doped sample sharply increases with the calcination temperature. This result is consistent with previous report that suggest that the increased amount of rutile phase increases the probability of a fast recombination rate (Cai et al., 2015). Hence, the PL result implies that co-doping at 350 °C can effectively separate the charge carriers, which is beneficial to the improvement of photocatalytic activity.

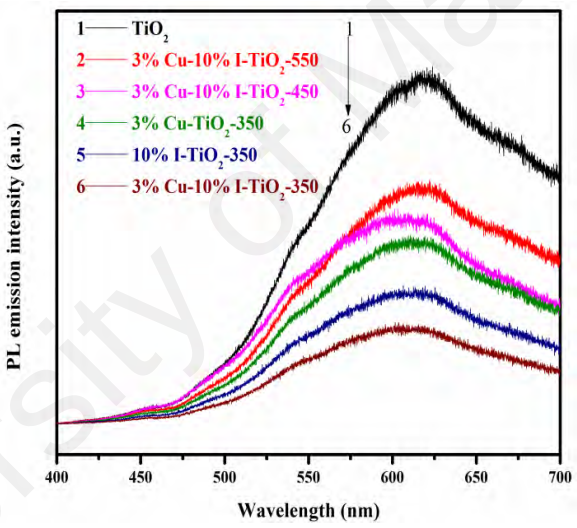

Figure 4.28: Photoluminescence emission spectra of the prepared TiO_2 catalysts.

4.2.7 XPS analysis

XPS was applied to investigate the chemical states of the Ti, O, Cu, and I of the photocatalysts. Figure 4.29a shows the high-resolution XPS spectra of the Ti 2p of the samples. In each spectrum, two main peaks exist in the Ti 2p energy region. The binding energies of Ti $2p_{3/2}$ and Ti $2p_{1/2}$ for pure TiO_2 are approximately 458.7 and 464.5 eV, respectively. These values are similar to the literature values of Ti^{4+} in pure

TiO_2 (Jaiswal et al., 2015). Compared to the pure TiO_2, the binding energies of Ti $2p_{3/2}$ and Ti $2p_{1/2}$ for the mono-doped samples (3% Cu-TiO_2 and 10% I-TiO_2) are shifted to smaller values. This finding suggests that some of the Ti^{4+} was reduced to Ti^{3+} due to the substitution of Ti^{4+} by the doped Cu^{2+} and I^{5+} (Jaiswal et al., 2015; Li et al., 2014; Zhang et al., 2011). This phenomenon could induce defects in the TiO_2 lattice, which could result in the reduction of Ti^{4+} to Ti^{3+} and the formation of oxygen vacancies. The formation of Ti^{3+} in the Cu and I doped TiO_2 was also observed by Jaiswal et al. (2015) and Zhang et al. (2011), and they attributed it to the incorporation of Cu and I into the TiO_2 lattice. However, the Ti 2p binding energy shifts back to 458.7eV for the co-doped sample. This result indicates that I doping actually inhibits the reduction of Ti^{4+}.

The high-resolution O 1s spectra of the samples in Figure 4.29b can be deconvoluted into two peaks. The main peak at around 529.8 eV is due to the lattice oxygen of TiO_2, and the other peak at around 530.8 eV is assigned to the superficial oxygen of the hydroxyl species (Zhang et al., 2011). The binding energy of the O 1s peak for the mono-doped samples is lower than that of pure TiO_2.

The high-resolution Cu 2p XPS spectra of 3% Cu-TiO_2 and 3% Cu-10% I-TiO_2 catalysts suggest that only Cu^{2+} is present with the corresponding peaks at around 932.4 and 952 eV (Figure 4.29c). From the results of XRD and Raman spectra, Cu^{2+} ions could substitute the Ti^{4+} ions to form the Ti–O–Cu bond in the TiO_2. Similar results were reported by other researchers (Dorraj et al., 2017; Zhou et al., 2016). In addition, I doping does not show a distinct influence on the chemical state of Cu.

Figure 4.29d of the I 3d core level shows a broad peak that can be deconvoluted into two peaks centered at 620.6 and 622.7 eV for the I-mono-doped TiO_2 and Cu-I-co-doped TiO_2, respectively. The former peak is attributed to I^-, and the latter peak confirms the presence of I^{5+}. Thus, the presence of I^{5+}/I^- pairs suggests that I^{5+} ions

could replace Ti^{4+} to form the I–O–Ti bond, which is in accordance with the XRD and Raman results. These results are in good agreement with previous studies on I-TiO_2 (Tojo et al., 2008; Zhang et al., 2011). Notably, the 3% Cu-10% I-TiO_2 sample has a higher I^- concentration compared to the 10% I-TiO_2 sample. This finding implies that the Cu^{2+} incorporated into the TiO_2 lattice may induce the reduction of I^{5+} ions to a low multi-valence I^- state in the TiO_2 lattice. The efficient electron scavenging by these multi-valence iodine ions (I^{5+}/I^-) contributed to the effective electron–hole separation of the (Li et al., 2014; Tojo et al., 2008), as confirmed by the PL result. Moreover, the chemical state of I was unaffected by the Cu doping.

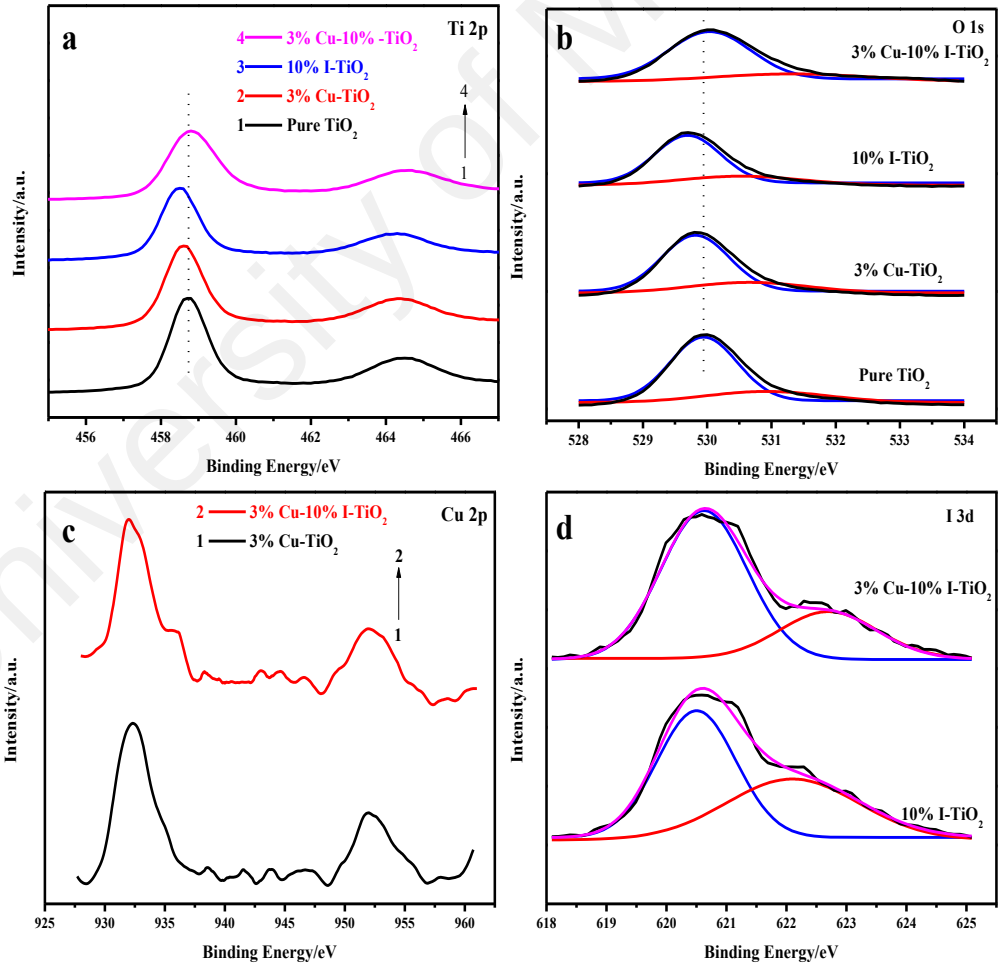

Figure 4.29: Ti 2p (a), O 1s (b), Cu 2p (c) and I 3d (d) XPS spectra of 3% Cu-10% I-co-doped TiO_2.

4.2.8 EIS analysis

The Nyquist plots confirmed the advantage of co-doped TiO_2 over mono-doped and pure TiO_2 samples in the charge separation efficiency and photoinduced electron transfer. Figure 4.30 shows that the smallest arc radius of the co-doped TiO_2 compared with those of the mono-doped and pure TiO_2. This finding indicates an efficient photogenerated electron–hole separation and fast interfacial photogenerated electron transfer of the co-doped TiO_2 under visible irradiation (Tojo et al., 2008).

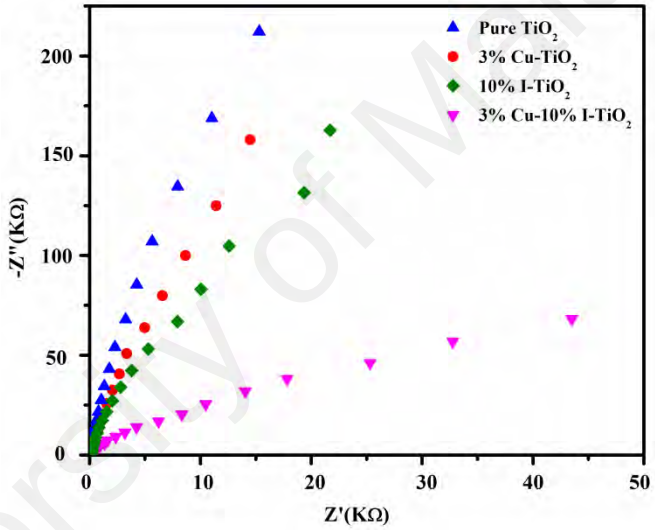

Figure 4.30: EIS Nyquist plots of the as-prepared samples under visible light irradiation.

4.2.9 Photocatalytic activity

The photocatalytic activity of 3% Cu-10% I-TiO_2 was compared with those of mono-doped (3% Cu-TiO_2 and 10% I-doped TiO_2) and undoped-TiO_2 under visible-light irradiation for the photodegradation of MO dyes. As shown in Figure 4.31, no clear degradation of MO occurs in the absence of visible light, which confirms that MO degradation is due to light absorption. Under visible-light irradiation, co-doped TiO_2 shows higher catalytic activity compared to the other samples. After 1 h, the co-doped-

TiO_2 degrades 80% of MO, which is higher than those of 3% Cu-TiO_2 (62%), 10% I-TiO_2 (64%), and pure TiO_2 (4.6%).

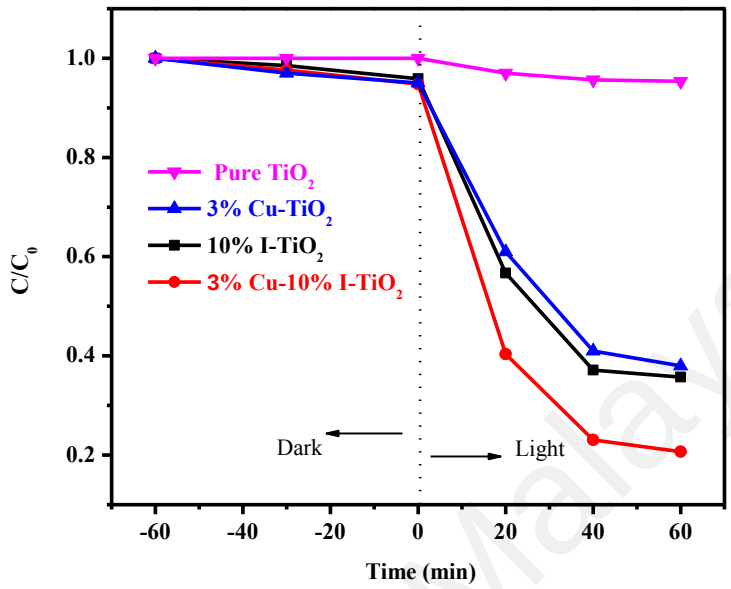

Figure 4.31: Photodegradation of MO by the as-prepared products under visible light irradiation.

To study the degradation kinetics of the samples, the experimental data points in Figure 4.32a were fitted to the pseudo first-order kinetic model by a linear method which can be described by the following equation:

$$\ln\left({}^{C_0}/_{C}\right) = kt$$

where k is the rate constant of degradation, and t is the degradation time. The fitted curves are presented in Figure 4.32a.

Furthermore, Figure 4.32b displays that the k value (0.030 min^{-1}) of the co-doped sample is around 1.67 and 1.5 larger than those of the Cu mono-doped TiO_2 (0.018 min^{-1}) and I mono-doped TiO_2 (0.020 min^{-1}), respectively. Accordingly, the results

specified that the I and Cu co-doped TiO_2 obtained higher photo-catalytic activity than those of the mono-doped samples.

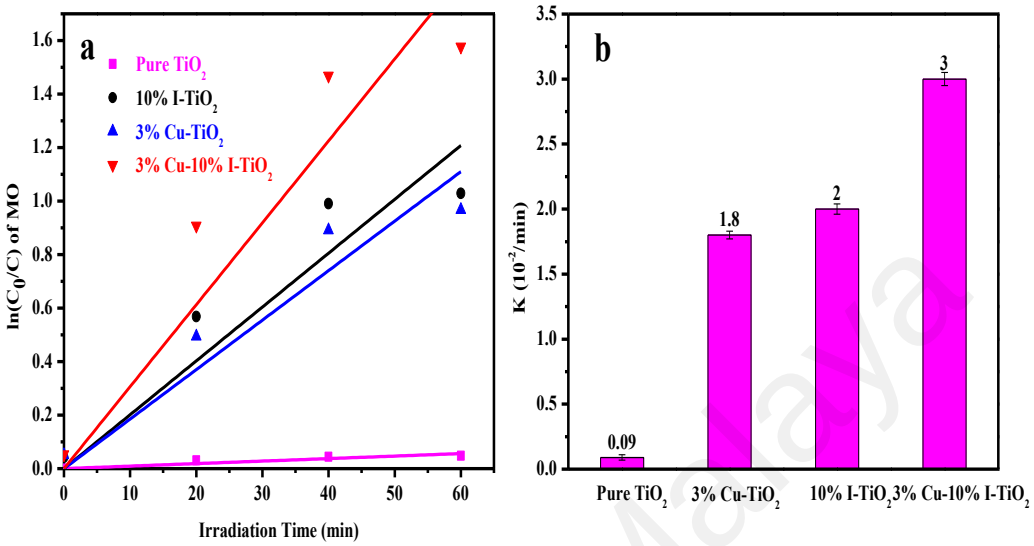

Figure 4.32: (a) The pseudo first order reaction kinetics and (b) Apparent rate constants of the prepared samples for MO degradation.

As shown in Figure 4.33, continuous photocatalytic activity was measured and showed no significant loss in activity even after four runs, which indicates that the co-doped sample possessed excellent photocatalytic stability.

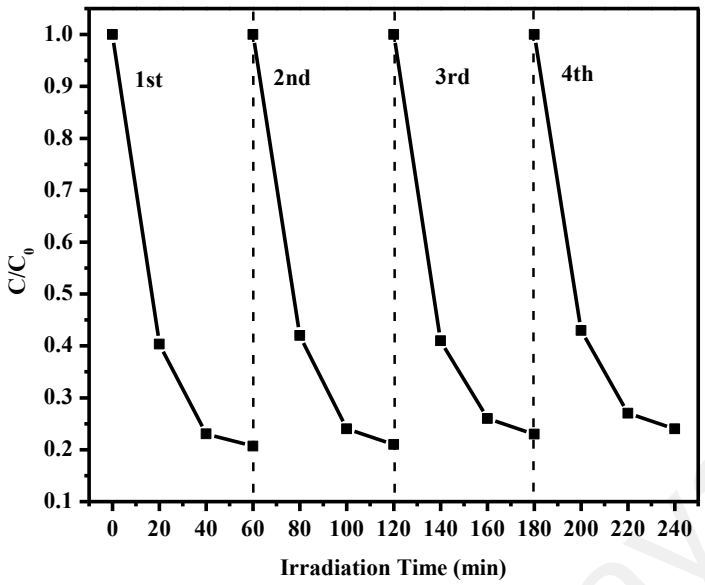

Figure 4.33: Cycling runs for the photocatalytic MO degradation in the presence of 3% Cu-10% I-co-doped TiO_2 photocatalyst.

4.2.10 Possible photocatalytic mechanism

The three main factors that control the photocatalytic activity are: (1) visible-light absorption capability, (2) recombination of photogenerated charge carriers, and (3) surface area of the photocatalyst. The surface areas of all samples were almost the same. In the present case, surface area factor did not affect the activity of the TiO_2, although it should not be ignored. The significant band gap narrowing of Cu-doped TiO_2, was due to the energy levels formed by Cu above the valence band maximum (VBM) and the shift to upper energy responsible for greater photocatalytic activity in Cu-doped TiO_2 compared to the pure TiO_2. The photocatalytic efficiency was boosted by the co-doping of I in Cu-TiO_2. No significant variation was observed in the band gap of Cu-I-TiO_2 compared to the Cu-TiO_2 from the UV spectra. Therefore, the enhanced photocatalytic activity was due to the decreased recombination (as confirmed by the PL and EIS results) caused by the formation of multi-valence I^{5+}/I^{-} below the conduction band minimum that served as trapping centers for the photogenerated electrons to decrease

the recombination rate. Moreover, the intermediate energy levels of Cu^{2+} located above the VBM can act as hole-trapping sites. Therefore, the combined effects of both Cu^{2+} and (I^{5+}/I^{-}) dopants for enhanced charge separation could effectively decrease recombination in the co-doped sample.

In addition, all the photocatalyst samples prepared in the current study contained an anatase-rutile phase. Thus, clearly distinguishing the effect of anatase-rutile dual phase in nano-structured TiO_2 is necessary. Several researchers demonstrated that the energy levels of the conduction band and valence band in rutile TiO_2 are higher than that of the anatase TiO_2. This phenomenon allows the transfer of photo-induced electrons from the rutile phase to the anatase phase and holes in the opposite direction (Lavanya et al., 2017; Wang et al., 2016). This phenomenon facilitates an effective electron–hole separation. However, only a slight variation of the crystalline structure was found in this study for the pure, mono-doped and co-doped samples at 350 °C. Thus, the variation of photocatalytic activity of different samples cannot be attributed to the crystalline structure. By decreasing the charge carrier recombination in the co-doped sample, e^{-} and h^{+} pairs can diffuse to the surface of the photocatalyst, react with the hydroxyl groups, and adsorb oxygen and water, thereby causing the OH• radicals to be highly reactive. Figure 4.34 displays the schematic illustration of the proposed mechanism for the enhanced photocatalytic activity of the co-doped sample.

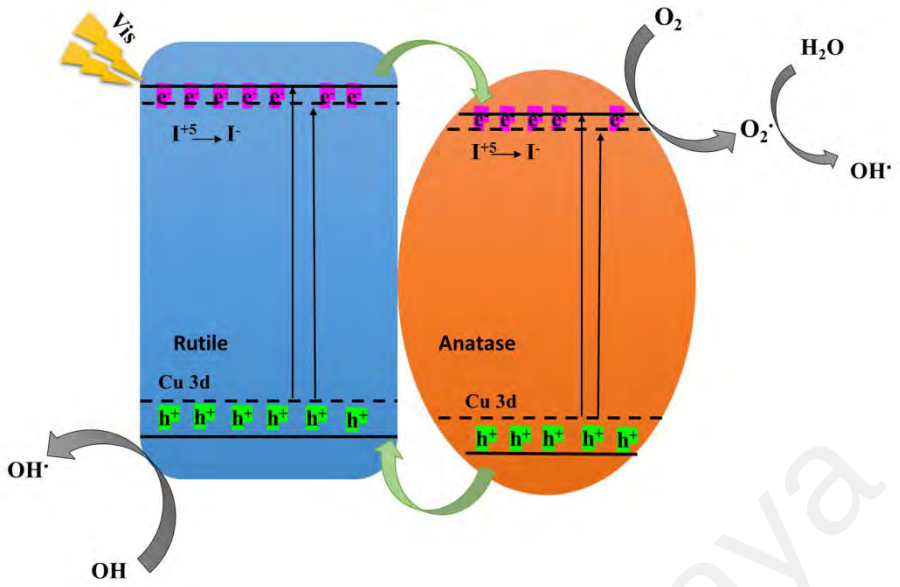

Figure 4.34: Schematic of photoelectron transfer pathway for 3%Cu-10%I-co-doped TiO_2 for MO degradation.

The OH• radicals have been known as the primary reactive species responsible for organic pollutant degradation. As mentioned in Section 3.5, the reaction between the OH• radical and TPA generates a fluorescent-active product, HTPA, which is easily monitored by PL spectroscopy. The fluorescence intensity of HTPA corresponds to the amount of OH• radicals produced on the photocatalysts surface. The fluorescence spectra of HTPA for the co-doped sample under visible-light irradiation are presented in Figure 4.35. The fluorescence intensity increases with the irradiation time. This finding indicates that OH• is produced during the photocatalytic degradation under visible-light irradiation. However, no variation is detected in the fluorescence intensity in the absence of visible-light irradiation. This finding confirms that the fluorescence intensity is due to the reaction between the TPA and OH• generated during the photocatalytic process. In general, the enhanced OH• formation rate is related to effective electron–hole separation. Therefore, a positive relationship exists between the photocatalytic degradation and the formation rate of OH• radicals (Nosaka & Nosaka , 2016).

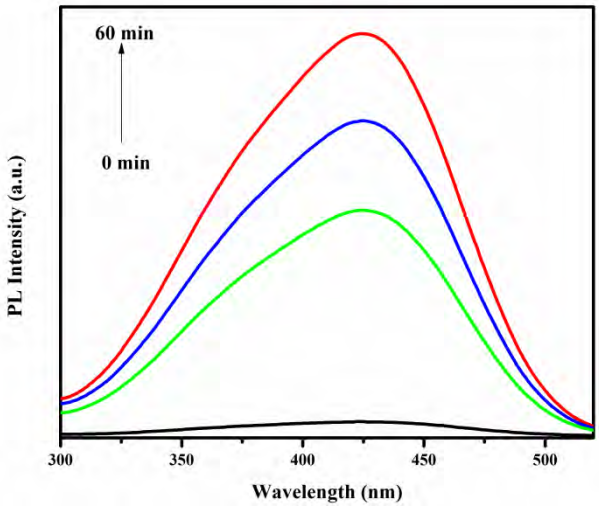

Figure 4.35: Fluorescence spectral changes measured during illumination of 3% Cu-10% I-codoped TiO_2 sample in a basic solution of terephthalic acid.

CHAPTER 5: GENERAL CONCLUSION AND FUTURE WORK

5.1 Conclusion

In general, the research study was a success. The subsequent conclusions and recommendations are drawn according to the research aims, and the results achieved in the study:

1. Cu-TiO_2/ZnO heterostructured nanocomposites were prepared by a sol–gel method. The nanocomposites exhibited significantly high visible-light-driven photocatalytic activity during the MO degradation. The photocatalytic activity of the nanocomposite was 2-and 28-fold higher than those of the Cu-TiO_2 and TiO_2 nanoparticles during MO degradation, respectively. The excellent photocatalytic activity of the nanocomposites was attributed to the formation of heterojunction between the two coupled semiconductors. This results indicates that the Cu-TiO_2/ZnO heterojunction photocatalyst could generate many electron–hole pairs under visible light irradiation and result in higher photocatalytic performance. The lower recombination rate of the photogenerated electron–hole pairs can be described by a hypothesized mechanism based on the heterojunction between the TiO_2 and ZnO. Finally, the 3% Cu-TiO_2/30% ZnO nanocomposites exhibited considerable photoactivity after three successive runs. The novel nanocomposites could offer prospective applications in environmental photocatalytic processes.
2. Cu and I co-doped TiO_2 photocatalysts were synthesized with different calcination temperatures through a hydrothermal method and tested for the degradation of MO under visible light. The Cu and I co-dopants inhibited the TiO_2-phase transformation from the anatase phase to the rutile phase. XPS and ICP-MS analyses revealed that Cu^{2+} and I^{5+} were doped into the TiO_2

lattice. The degradation of MO dye at 350 °C under visible-light irradiation shifted to Cu and I co-doped TiO_2 at a faster rate compared to those of the mono-doped and undoped TiO_2. This phenomenon was mainly attributed to high visible-light absorption caused by Cu^{2+} energy levels. Meanwhile, effective charge separation was obtained by multi-valence I^{5+}/I^{-}. The presence of Cu^{2+} species prompted the reduction of I^{5+} to a lower multi-valence state I^{-} in the TiO_2 lattice. The I^{5+}/I^{-} caused significant separation of the electron–hole pairs in the co-doped sample. Furthermore, the co-doped TiO_2 catalysts exhibited excellent stability under visible-light irradiation, and may thus serve as efficient photocatalysts for environmental remediation.

5.2 Recommendation for future studies

The findings of the present research work are directive towards several areas which merit further studies, some of which are listed below:

1. In this thesis, the photocatalytic activities of the synthesized catalysts propose that electrons were trapped to inhibit the recombination of electrons and holes process. Theoretical studies such as density functional theory (DFT) can be performed to discover this phenomenon.
2. The interaction between adsorbed species to the surface and mechanisms of MO dye adsorption on the catalysts surface should be explored.
3. To discover the effect of various operational parameters such as catalyst amount, solution pH, light intensity and MO concentration in the photodegradation of MO.
4. The prepared photocatalysts were successfully employed in synthetic dye solutions, real industrial dye effluent may be used to evaluate the performance of the different photocatalysts.

5. Evaluation of the prepared photocatalysts for reduction/oxidation of inorganic compounds such as NO, CO, Cr (IV), etc. and also for the degradation of other organic compounds apart from the dyes.

REFERENCES

Agorku, E. S., Mamba, B. B., Pandey, A. C., & Mishra, A. K. (2014). Sulfur/Gadolinium-Codoped TiO_2 nanoparticles for enhanced visible-light photocatalytic performance. *Journal of Nanomaterials*, *2014*, 4.

Aguilar, T., Navas, J., Alcántara, R., Fernández-Lorenzo, C., Gallardo, J. J., Blanco, G., & Martín-Calleja, J. (2013). A route for the synthesis of Cu-doped TiO_2 nanoparticles with a very low band gap. *Chemical Physics Letters*, *571*, 49–53.

Akple, M. S., Low, J., Liu, S., Cheng, B., Yu, J., & Ho, W. (2016). Fabrication and enhanced CO_2 reduction performance of N-self-doped TiO_2 microsheet photocatalyst by bi-cocatalyst modification. *Journal of CO_2 Utilization*, *16*, 442–449.

Akple, M. S., Low, J., Qin, Z., Wageh, S., Al-Ghamdi, A. A., Yu, J., & Liu, S. (2015). Nitrogen-doped TiO_2 microsheets with enhanced visible light photocatalytic activity for CO_2 reduction. *Cuihua Xuebao/Chinese Journal of Catalysis*, *36*(12), 2127–2134.

Al Saqri, N. A., Mondal, A., Felix, J. F., Gobato, Y. G., Gordo, V. O., Albalawi, H., Henini, M. (2017). Investigation of defects in indium doped TiO_2 thin films using electrical and optical techniques. *Journal of Alloys and Compounds*, *698*, 883–891.

Aljawfi, R. N., Vij, A., Chae, K. H., Dalela, S., Alvi, P. A., AL-Maghrabi, M. A., & Kumar, S. (2018). Effects of rapid thermal annealing on the local environment, electronic structure and magnetic properties of Mn doped TiO_2 thin films. *Applied Surface Science*, *445*, 287–297.

Amano, F., Nakata, M., Yamamoto, A., & Tanaka, T. (2016). Rutile titanium dioxide prepared by hydrogen reduction of Degussa P25 for highly efficient photocatalytic hydrogen evolution. *Catal. Sci. Technol.*, *6*(14), 5693–5699.

Ambrus, Z., Balázs, N., Alapi, T., Wittmann, G., Sipos, P., Dombi, A., & Mogyorósi, K. (2008). Synthesis, structure and photocatalytic properties of Fe (III)-doped TiO_2 prepared from TiCl 3. *Applied Catalysis B: Environmental*, *81*(1), 27–37.

Aritani, H., Tanaka, T., Akasaka, N., Funabiki, T., Yoshida, S., Gotoh, H., & Okamoto, Y. (1997). Reduction of NO over TiO_2-Supported Cu Catalysts: 2. Structure of Active Cu Species Studied by CuK-Edge XAFS. *Journal of Catalysis*, *168*(2), 412–420.

Assadi, M. H. N., & Hanaor, D. A. H. (2016). The effects of copper doping on photocatalytic activity at (101) planes of anatase TiO_2: A theoretical study. *Applied Surface Science*, *387*, 682–689.

Bagwasi, S., Tian, B., Chen, F., & Zhang, J. (2012). Synthesis, characterization and application of iodine modified titanium dioxide in phototcatalytical reactions under visible light irradiation. *Applied Surface Science*, *258*(8), 3927–3935.

Bai, S., Li, H., Guan, Y., & Jiang, S. (2011). The enhanced photocatalytic activity of

CdS/TiO_2 nanocomposites by controlling CdS dispersion on TiO_2 nanotubes. *Applied Surface Science*, *257*(15), 6406–6409.

Bando, K. K., Sayama, K., Kusama, H., Okabe, K., & Arakawa, H. (1997). In-situ FT-IR study on CO_2 hydrogenation over Cu catalysts supported on SiO_2, Al_2O_3, and TiO_2. *Applied Catalysis A: General*, *165*(1–2), 391–409.

Bensouici, F., Bououdina, M., Dakhel, A. A., Tala-Ighil, R., Tounane, M., Iratni, A., Cai, W. (2017). Optical, structural and photocatalysis properties of Cu-doped TiO_2 thin films. *Applied Surface Science*, *395*, 110–116.

Bessekhouad, Y., Chaoui, N., Trzpit, M., Ghazzal, N., Robert, D., & Weber, J. V. (2006). UV–vis versus visible degradation of Acid Orange II in a coupled CdS/ TiO_2 semiconductors suspension. *Journal of Photochemistry and Photobiology A: Chemistry*, *183*(1), 218–224.

Bickley, R. I., Gonzalez-Carreno, T., Lees, J. S., Palmisano, L., & Tilley, R. J. D. (1991). A structural investigation of titanium dioxide photocatalysts. *Journal of Solid State Chemistry*, *92*(1), 178–190.

Binas, V., Venieri, D., Kotzias, D., & Kiriakidis, G. (2017). Modified TiO_2 based photocatalysts for improved air and health quality. *Journal of Materiomics*, *3*(1), 3–16.

Bingham, S., & Daoud, W. A. (2011). Recent advances in making nano-sized TiO_2 visible-light active through rare-earth metal doping. *Journal of Materials Chemistry*, *21*(7), 2041–2050.

Blomquist, W., Cunniff, S., Fox, P., Furukawa, D., Garcia, M., Gritzuk, M., Price, K. (2012). Desalination and water Purification technology roadmap: A report of the executive committee. In *Desalination: Solutions and Roadmap for an Improved Water Supply*. Nova Science Publishers, Inc, USA.

Boccuzzi, F., & Chiorino, A. (1997). Preparation , Characterization , and Activity of Cu / TiO_2 Catalysts, *139*, 129–139.

Boumaza, S., Bellal, B., Boudjemaa, A., & Trari, M. (2016). Photodegradation of orange G by the hetero-junction x%Bi_2S_3/TiO_2 under solar light. *Solar Energy*, *139*, 444–451.

Cai, H., Chen, X., Li, Q., He, B., & Tang, Q. (2013). Enhanced photocatalytic activity from Gd, la codoped TiO_2 nanotube array photocatalysts under visible-light irradiation. *Applied Surface Science*, *284*, 837–842.

Cai, J., Xin, W., Liu, G., Lin, D., & Zhu, D. (2015). Effect of calcination temperature on structural properties and photocatalytic activity of Mn-C-codoped TiO_2, *19*(2), 401–407.

Cao, F., Xin, S., Guo, Y., & Wan, L. (2011). Nano-current-collectors as high-rate anode materials in lithium-ion, *Physical Chemistry Chemical Physics*, *13*, 2014–2020.

Cargnello, M., Gordon, T. R., & Murray, C. B. (2014). Solution-phase synthesis of

titanium dioxide nanoparticles and nanocrystals. *Chemical Reviews*, *114*(19), 9319–9345.

Chang, S., & Liu, W. (2014). The roles of surface-doped metal ions (V, Mn, Fe, Cu, Ce, and W) in the interfacial behavior of TiO_2 photocatalysts. *Applied Catalysis B: Environmental*, *156–157*, 466–475.

Chen, X., Wu, Z., Liu, D., & Gao, Z. (2017). Preparation of ZnO photocatalyst for the efficient and rapid photocatalytic degradation of azo dyes. *Nanoscale Research Letters*, *12*(1), 143.

Chen, Z., Li, Y., Guo, M., Xu, F., Wang, P., Du, Y., & Na, P. (2016). One-pot synthesis of Mn-doped TiO_2 grown on graphene and the mechanism for removal of Cr(VI) and Cr(III). *Journal of Hazardous Materials*, *310*, 188–198.

Cheng, X. Q., Ma, C. Y., Yi, X. Y., Yuan, F., Xie, Y., Hu, J. M., Zhang, Q. Y. (2016). Structural, morphological, optical and photocatalytic properties of Gd-doped TiO_2 films. *Thin Solid Films*, *615*, 13–18.

Chong, M. N., Jin, B., Chow, C. W. K., & Saint, C. (2010). Recent developments in photocatalytic water treatment technology: a review. *Water Research*, *44*(10), 2997–3027.

Choudhury, B., Dey, M., & Choudhury, A. (2013). Defect generation, d-d transition, and band gap reduction in Cu-doped TiO_2 nanoparticles. *International Nano Letters*, *3*(1), 25.

Colmenares, J. C., Luque, R., Campelo, J. M., Colmenares, F., Karpiński, Z., & Romero, A. A. (2009). Nanostructured photocatalysts and their applications in the photocatalytic transformation of lignocellulosic biomass: an overview. *Materials*, *2*(4), 2228–2258.

Colo´n, G., Maicu, M., Hidalgo, M. C., & Navı´o, J. A. (2006). Cu-doped TiO_2 systems with improved photocatalytic activity, *Physical Chemistry Chemical Physics*, *67*, 41–51.

Cozzoli, P. D., Comparelli, R., Fanizza, E., Curri, M. L., & Agostiano, A. (2003). Photocatalytic activity of organic-capped anatase TiO_2 nanocrystals in homogeneous organic solutions. *Materials Science and Engineering: C*, *23*(6), 707–713.

Crişan, M., Răileanu, M., Drăgan, N., Crişan, D., Ianculescu, A., Niţoi, I., Stan, C. (2015). Sol–gel iron-doped TiO_2 nanopowders with photocatalytic activity. *Applied Catalysis A: General*, *504*, 130–142.

Daghrir, R., Drogui, P., & Robert, D. (2013). Modified TiO_2 for environmental photocatalytic applications: A review. *Industrial and Engineering Chemistry Research*, *52*(10), 3581–3599.

Dashora, A., Patel, N., Kothari, D. C., Ahuja, B. L., & Miotello, A. (2014). Solar Energy Materials & Solar Cells Formation of an intermediate band in the energy gap of TiO_2 by Cu – N-codoping : First principles study and experimental

evidence. *Solar Energy Materials and Solar Cells*, *125*, 120–126.

de Correa, C. M., Odriozola, J. A., & Centeno, M. A. (2006). Synthesis and characterization of xerogel titania modified with Pd and Ni. *Journal of Molecular Catalysis A: Chemical*, *253*(1), 252–260.

Demirci, S., Dikici, T., Yurddaskal, M., Gultekin, S., Toparli, M., & Celik, E. (2016). Synthesis and characterization of Ag doped TiO_2 heterojunction films and their photocatalytic performances. *Applied Surface Science*, *390*, 591–601.

Dong, H., Zeng, G., Tang, L., Fan, C., Zhang, C., He, X., & He, Y. (2015). An overview on limitations of TiO_2-based particles for photocatalytic degradation of organic pollutants and the corresponding countermeasures. *Water Research*, *79*, 128–146.

Dong, S., Feng, J., Fan, M., Pi, Y., Hu, L., Han, X., Sun, J. (2015). Recent developments in heterogeneous photocatalytic water treatment using visible light-responsive photocatalysts: a review. *RSC Advances.*, *5*(19), 14610–14630.

Dorraj, M., Alizadeh, M., Sairi, N. A., Basirun, W. J., Goh, B. T., Woi, P. M., & Alias, Y. (2017). Enhanced visible light photocatalytic activity of copper-doped titanium oxide–zinc oxide heterojunction for methyl orange degradation. *Applied Surface Science*, *414*, 251–261.

Dozzi, M. V., Saccomanni, A., & Selli, E. (2012). Cr (VI) photocatalytic reduction: effects of simultaneous organics oxidation and of gold nanoparticles photodeposition on TiO_2. *Journal of Hazardous Materials*, *211*, 188–195.

El-Maghraby, E. M., Nakamura, Y., & Rengakuji, S. (2008). Composite TiO_2–SnO_2 nanostructured films prepared by spin-coating with high photocatalytic performance. *Catalysis Communications*, *9*(14), 2357–2360.

Epling, G. A., & Lin, C. (2002). Photoassisted bleaching of dyes utilizing TiO_2 and visible light. *Chemosphere*, *46*(4), 561–570.

Farbod, M., & Kajbafvala, M. (2013). Effect of nanoparticle surface modification on the adsorption-enhanced photocatalysis of Gd/TiO_2 nanocomposite. *Powder Technology*, *239*, 434–440.

Farhadi, A., Mohammadi, M. R., & Ghorbani, M. (2017). On the assessment of photocatalytic activity and charge carrier mechanism of TiO_2@SnO_2 core-shell nanoparticles for water decontamination. *Journal of Photochemistry and Photobiology A: Chemistry*, *338*, 171–177.

Ferrari-Lima, A. M., De Souza, R. P., Mendes, S. S., Marques, R. G., Gimenes, M. L., & Fernandes-Machado, N. R. C. (2015). Photodegradation of benzene, toluene and xylenes under visible light applying N-doped mixed TiO_2 and ZnO catalysts. *Catalysis Today*, *241*, 40–46.

Flörke, M., Schneider, C., & McDonald, R. I. (2018). Water competition between cities and agriculture driven by climate change and urban growth. *Nature Sustainability*, *1*(1), 51.

Frank, S. N., & Bard, A. J. (1977). Semiconductor Electrodes Photoassisted Oxidations and Photoelectrosynthesis at Polycrystalline TiO_2 Electrodes. *Journal of the American Chemical Society*, *99*(14), 4667–4675.

Fujishima, A., & Honda, K. (1972). Electrochemical Photolysis of Water at a Semiconductor Electrode. *Nature*, *238*(5358), 37–38.

Fujishima, A., Zhang, X., & Tryk, D. A. (2007). Heterogeneous photocatalysis: from water photolysis to applications in environmental cleanup. *International Journal of Hydrogen Energy*, *32*(14), 2664–2672.

Ganesh, I. (2017). Effects of phosphorus-doping on energy band-gap, structural, surface, and photocatalytic characteristics of emulsion-based sol-gel derived TiO_2 nano-powder. *Applied Surface Science*, *414*, 277–291.

Gao, M., Zhang, D., Pu, X., Ma, H., Su, C., Gao, X., & Dou, J. (2016). Surface decoration of BiOBr with $BiPO_4$ nanoparticles to build heterostructure photocatalysts with enhanced visible-light photocatalytic activity. *Separation and Purification Technology*, *170*, 183–189.

George, S., Pokhrel, S., Ji, Z., Henderson, B. L., Xia, T., Li, L., Mädler, L. (2011). Role of Fe doping in tuning the band gap of TiO_2 for the photo-oxidation-induced cytotoxicity paradigm. *Journal of the American Chemical Society*, *133*(29), 11270–11278.

Gholami, M., Nassehinia, H. R., Jonidi-Jafari, A., Nasseri, S., & Esrafili, A. (2014). Comparison of Benzene & Toluene removal from synthetic polluted air with use of Nano photocatalyticTiO_2/ZNO process. *Journal of Environmental Health Science and Engineering*, *12*(1), 45.

Gober, P. (2018). Human Dimensions of Water Security. In *Building Resilience for Uncertain Water Futures* (pp. 13–36). Springer, USA.

Guo, M., & Du, J. (2012). First-principles study of electronic structures and optical properties of Cu, Ag, and Au-doped anatase TiO_2. *Physica B: Condensed Matter*, *407*(6), 1003–1007.

Gupta, S. M., & Tripathi, M. (2011). A review of TiO_2 nanoparticles. *Chinese Science Bulletin*, *56*(16), 1639.

Hamadanian, M., Reisi-Vanani, A., & Majedi, A. (2010). Synthesis, characterization and effect of calcination temperature on phase transformation and photocatalytic activity of Cu,S-codoped TiO_2 nanoparticles. *Applied Surface Science*, *256*(6), 1837–1844.

Hamden, Z., Ferreira, D. P., Ferreira, L. F. V., & Bouattour, S. (2014). Li–Y doped and codoped TiO_2 thin films: Enhancement of photocatalytic activity under visible light irradiation. *Ceramics International*, *40*(2), 3227–3235.

Han, T., Fan, T., Chow, S.-K., & Zhang, D. (2010). Biogenic N–P-codoped TiO_2: synthesis, characterization and photocatalytic properties. *Bioresource Technology*, *101*(17), 6829–6835.

Hanaor, D. A. H., & Sorrell, C. C. (2011). Review of the anatase to rutile phase transformation. *Journal of Materials Science*, *46*(4), 855–874.

He, D., Li, Y., Wang, I., Wu, J., Yang, Y., & An, Q. (2017). Carbon wrapped and doped TiO_2 mesoporous nanostructure with efficient visible-light photocatalysis for NO removal. *Applied Surface Science*, *391*, 318–325.

Heinlaan, M., Ivask, A., Blinova, I., Dubourguier, H.-C., & Kahru, A. (2008). Toxicity of nanosized and bulk ZnO, CuO and TiO_2 to bacteria Vibrio fischeri and crustaceans Daphnia magna and Thamnocephalus platyurus. *Chemosphere*, *71*(7), 1308–1316.

Hernández-Alonso, M. D., Fresno, F., Suárez, S., & Coronado, J. M. (2009). Development of alternative photocatalysts to TiO_2: challenges and opportunities. *Energy & Environmental Science*, *2*(12), 1231–1257.

Hoffman, A. J., Carraway, E. R., & Hoffmann, M. R. (1994). Photocatalytic production of H_2O_2 and organic peroxides on quantum-sized semiconductor colloids. *Environmental Science & Technology*, *28*(5), 776–785.

Hoffmann, M. R., Martin, S. T., Choi, W., & Bahnemann, D. W. (1995). Environmental applications of semiconductor photocatalysis. *Chemical Reviews*, *95*(1), 69–96.

Hojamberdiev, M., Zhu, G., Sujaridworakun, P., Jinawath, S., Liu, P., & Zhou, J.-P. (2012). Visible-light-driven N–F-codoped TiO_2 powders derived from different ammonium oxofluorotitanate precursors. *Powder Technology*, *218*, 140–148.

Hsiao, M.-T., Chen, S.-F., Shieh, D.-B., & Yeh, C.-S. (2006). One-pot synthesis of hollow Au_3Cu1 spherical-like and biomineral botallackite Cu_2 (OH_3Cl flowerlike architectures exhibiting antimicrobial activity. *The Journal of Physical Chemistry B*, *110*(1), 205–210.

Hsieh, C.-T., Fan, W.-S., Chen, W.-Y., & Lin, J.-Y. (2009). Adsorption and visible-light-derived photocatalytic kinetics of organic dye on Co-doped titania nanotubes prepared by hydrothermal synthesis. *Separation and Purification Technology*, *67*(3), 312–318.

Hu, Y., Tsai, H. L., & Huang, C. L. (2003). Effect of brookite phase on the anatase-rutile transition in titania nanoparticles. *Journal of the European Ceramic Society*, *23*(5), 691–696.

Hu, Z., Xu, T., & Fang, B. (2017). Photocatalytic degradation of vehicle exhaust using Fe-doped TiO_2 loaded on activated carbon. *Applied Surface Science*, *420*, 34–42.

Huang, Y., Hu, H., Wang, S., Balogun, M.-S., Ji, H., & Tong, Y. (2017). Low concentration nitric acid facilitate rapid electron–hole separation in vacancy-rich bismuth oxyiodide for photo-thermo-synergistic oxidation of formaldehyde. *Applied Catalysis B: Environmental*, *218*, 700–708.

Huixian, S. H. I., Zhang, T., & Hongliang, W. (2011). Preparation and photocatalytic activity of La^{3+} and Eu^{3+} co-doped TiO_2 nanoparticles: photo-assisted degradation of methylene blue. *Journal of Rare Earths*, *29*(8), 746–752.

Huo, Y., Yang, X., Zhu, J., & Li, H. (2011). Highly active and stable CdS–TiO_2 visible photocatalyst prepared by in situ sulfurization under supercritical conditions. *Applied Catalysis B: Environmental*, *106*(1), 69–75.

Hussein, A. M., Mahoney, L., Peng, R., Kibombo, H., Wu, C.-M., Koodali, R. T., & Shende, R. (2013). Mesoporous coupled ZnO/TiO_2 photocatalyst nanocomposites for hydrogen generation. *Journal of Renewable and Sustainable Energy*, *5*(3), 33118.

Ibhadon, A., & Fitzpatrick, P. (2013). Heterogeneous Photocatalysis: Recent Advances and Applications. *Catalysts*, *3*(1), 189–218.

Ilieva, M., Nakova, A., & Tsakova, V. (2012). TiO_2/WO_3 hybrid structures produced through a sacrificial polymer layer technique for pollutant photo-and photoelectrooxidation under ultraviolet and visible light illumination. *Journal of Applied Electrochemistry*, *42*(2), 121–129.

Jaiswal, R., Bharambe, J., Patel, N., Dashora, A., Kothari, D. C., & Miotello, A. (2015). Copper and Nitrogen co-doped TiO_2 photocatalyst with enhanced optical absorption and catalytic activity. *Applied Catalysis B: Environmental*, *168–169*, 333–341.

Jaiswal, R., Patel, N., Dashora, A., Fernandes, R., Yadav, M., Edla, R., Miotello, A. (2016). Efficient Co-B-codoped TiO_2 photocatalyst for degradation of organic water pollutant under visible light. *Applied Catalysis B: Environmental*, *183*, 242–253.

Jaiswal, R., Patel, N., Kothari, D. C., & Miotello, A. (2012). Applied Catalysis B : Environmental Improved visible light photocatalytic activity of TiO_2 co-doped with Vanadium and Nitrogen. *Applied Catalysis B, Environmental,126*, 47–54.

Jensen, O., & Wu, H. (2018). Urban water security indicators: Development and pilot. *Environmental Science & Policy*, *83*, 33–45.

Ji, J., Xu, Y., Huang, H., He, M., Liu, S., Liu, G., … Zhan, Y. (2017). Mesoporous TiO_2 under VUV irradiation: Enhanced photocatalytic oxidation for VOCs degradation at room temperature. *Chemical Engineering Journal*, *327*, 490–499.

Jiang, D., Zhou, T., Sun, Q., Yu, Y., Shi, G., & Jin, L. (2011). Enhanced Visible-Light-Induced Photoelectrocatalytic Degradation of Methyl Orange by CdS Sensitized TiO_2 Nanotube Arrays Electrode. *Chinese Journal of Chemistry*, *29*(11), 2505–2510.

Jiang, J., Li, H., & Zhang, L. (2012). New insight into daylight photocatalysis of AgBr@Ag: synergistic effect between semiconductor photocatalysis and plasmonic photocatalysis. *Chemistry–A European Journal*, *18*(20), 6360–6369.

Jiang, P., Xiang, W., Kuang, J., Liu, W., & Cao, W. (2015). Effect of cobalt doping on the electronic, optical and photocatalytic properties of TiO_2. *Solid State Sciences*, *46*, 27–32.

Jiang, Y., Liu, P., Liu, Y., Liu, X., Li, F., Ni, L., Huo, P. (2016). Construction of

amorphous Ta_2O_5/g-C_3N_4 nanosheet hybrids with superior visible-light photoactivities for organic dye degradation and mechanism insight. *Separation and Purification Technology*, *170*, 10–21.

Jimmy, C. Y., Wu, L., Lin, J., Li, P., & Li, Q. (2003). Microemulsion-mediated solvothermal synthesis of nanosized CdS-sensitized TiO_2 crystalline photocatalyst. *Chemical Communications*, (13), 1552–1553.

Jing, L., Li, S., Song, S., Xue, L., & Fu, H. (2008). Investigation on the electron transfer between anatase and rutile in nano-sized TiO_2 by means of surface photovoltage technique and its effects on the photocatalytic activity. *Solar Energy Materials and Solar Cells*, *92*(9), 1030–1036.

Jo, W.-K., Adinaveen, T., Vijaya, J. J., & Sagaya Selvam, N. C. (2016). Synthesis of MoS_2 nanosheet supported Z-scheme TiO_2/g-C_3N_4 photocatalysts for the enhanced photocatalytic degradation of organic water pollutants. *RSC Advances*, *6*(13), 10487–10497.

Joshi, M. M., Labhsetwar, N. K., Mangrulkar, P. A., Tijare, S. N., Kamble, S. P., & Rayalu, S. S. (2009). Visible light induced photoreduction of methyl orange by N-doped mesoporous titania. *Applied Catalysis A: General*, *357*(1), 26–33.

Kaur, P., Kushwaha, J. P., & Sangal, V. K. (2018). Electrocatalytic oxidative treatment of real textile wastewater in continuous reactor: Degradation pathway and disposability study. *Journal of Hazardous Materials*, *346*, 242–252.

Kerkez-Kuyumcu, Ö., Kibar, E., Dayıoğlu, K., Gedik, F., Akın, A. N., & Özkara-Aydınoğlu, Ş. (2015). A comparative study for removal of different dyes over M/TiO_2 (M= Cu, Ni, Co, Fe, Mn and Cr) photocatalysts under visible light irradiation. *Journal of Photochemistry and Photobiology A: Chemistry*, *311*, 176–185.

Kesieme, U. K., Milne, N., Aral, H., Cheng, C. Y., & Duke, M. (2013). Economic analysis of desalination technologies in the context of carbon pricing, and opportunities for membrane distillation. *Desalination*, *323*, 66–74.

Kessler, V. G. (2013). Aqueous route to TiO_2-based nanomaterials using pH-neutral carboxylate precursors. *Journal of Sol-Gel Science and Technology*, *68*(3), 464–470.

Khalid, N. R., Ahmed, E., Hong, Z., Ahmad, M., Zhang, Y., & Khalid, S. (2013). Cu-doped TiO_2 nanoparticles/graphene composites for efficient visible-light photocatalysis. *Ceramics International*, *39*(6), 7107–7113.

Khalid, N. R., Ahmed, E., Hong, Z., Zhang, Y., & Ahmad, M. (2012). Nitrogen doped TiO_2 nanoparticles decorated on graphene sheets for photocatalysis applications. *Current Applied Physics*, *12*(6), 1485–1492.

Khalid, S., Murtaza, B., Shaheen, I., Ahmad, I., Ullah, M. I., Abbas, T., Imran, M. (2018). Assessment and public perception of drinking water quality and safety in district Vehari, Punjab, Pakistan. *Journal of Cleaner Production*, *181*, 224–234.

Khan, H., Rigamonti, M. G., Patience, G. S., & Boffito, D. C. (2017). Spray Dried TiO_2 /WO_3 Heterostructure for Photocatalytic Applications with Residual Activity in the Dark. *Applied Catalysis B: Environmental*.

Khan, R., & Kim, T.-J. (2009). Preparation and application of visible-light-responsive Ni-doped and SnO_2-coupled TiO_2 nanocomposite photocatalysts. *Journal of Hazardous Materials*, *163*(2), 1179–1184.

Khan, S., He, X., Khan, J. A., Khan, H. M., Boccelli, D. L., & Dionysiou, D. D. (2017). Kinetics and mechanism of sulfate radical-and hydroxyl radical-induced degradation of highly chlorinated pesticide lindane in UV/peroxymonosulfate system. *Chemical Engineering Journal*, *318*, 135–142.

Kisch, H., Zang, L., Lange, C., Maier, W. F., Antonius, C., & Meissner, D. (1998). Modified, amorphous titania—a hybrid semiconductor for detoxification and current generation by visible light. *Angewandte Chemie International Edition*, *37*(21), 3034–3036.

Kment, S., Kmentova, H., Kluson, P., Krysa, J., Hubicka, Z., Cirkva, V., Jastrabik, L. (2010). Notes on the photo-induced characteristics of transition metal-doped and undoped titanium dioxide thin films. *Journal of Colloid and Interface Science*, *348*(1), 198–205.

Kong, L., Wang, C., Wan, F., Zheng, H., & Zhang, X. (2017). Synergistic effect of surface self-doping and Fe species-grafting for enhanced photocatalytic activity of TiO_2 under visible-light. *Applied Surface Science*, *396*, 26–35.

Kordouli, E., Dracopoulos, V., Vaimakis, T., Bourikas, K., Lycourghiotis, A., & Kordulis, C. (2015). Comparative study of phase transition and textural changes upon calcination of two commercial titania samples: A pure anatase and a mixed anatase-rutile. *Journal of Solid State Chemistry*, *232*, 42–49.

Kotsis, K., & Staemmler, V. (2006). Ab initio calculations of the O1s XPS spectra of ZnO and Zn oxo compounds. *Physical Chemistry Chemical Physics : PCCP*, *8*(13), 1490–8.

Kuvarega, A. T., Krause, R. W. M., & Mamba, B. B. (2011). Nitrogen/palladium-codoped TiO_2 for efficient visible light photocatalytic dye degradation. *The Journal of Physical Chemistry C*, *115*(45), 22110–22120.

Kwiatkowski, M., Chassagnon, R., Geoffroy, N., Herbst, F., Heintz, O., Bezverkhyy, I., & Skompska, M. (2017). Enhancement of visible light photoelectrocatalytic activity of ZnO (core)/TiO_2 (shell) composite by N-doping and decorating with Au nanoparticles. *Electrochimica Acta*, *246*, 213–225.

Lan, X., Wang, L., Zhang, B., Tian, B., & Zhang, J. (2014). Preparation of lanthanum and boron co-doped TiO_2 by modified sol–gel method and study their photocatalytic activity. *Catalysis Today*, *224*, 163–170.

Lavanya, T., Dutta, M., Ramaprabhu, S., & Satheesh, K. (2017). Superior photocatalytic performance of graphene wrapped anatase/rutile mixed phase TiO_2 nanofibers synthesized by a simple and facile route. *Journal of Environmental Chemical*

Engineering, *5*(1), 494–503.

Lee, C.-G., Javed, H., Zhang, D., Kim, J.-H., Westerhoff, P., Li, Q., & Alvarez, P. J. J. (2018). Porous electrospun fibers embedding TiO_2 for adsorption and photocatalytic degradation of water pollutants. *Environmental Science & Technology*.

Lee, G.-J., Anandan, S., Masten, S. J., & Wu, J. J. (2016). Photocatalytic hydrogen evolution from water splitting using Cu doped ZnS microspheres under visible light irradiation. *Renewable Energy*, *89*, 18–26.

Lee, J. Y., & Jo, W.-K. (2016). Heterojunction-based two-dimensional N-doped TiO_2/WO_3 composite architectures for photocatalytic treatment of hazardous organic vapor. *Journal of Hazardous Materials*, *314*, 22–31.

Leung, D. Y. C., Fu, X., Wang, C., Ni, M., Leung, M. K. H., Wang, X., & Fu, X. (2010). Hydrogen Production over Titania-Based Photocatalysts. *ChemSusChem*, *3*(6), 681–694.

Li, G., Dimitrijevic, N. M., Chen, L., Rajh, T., & Gray, K. a. (2008). Role of Surface/Interfacial Cu^{2+} Sites in the Photocatalytic Activity of Coupled CuO− TiO_2 Nanocomposites. *The Journal of Physical Chemistry C*, *112*(48), 19040–19044.

Li, G., Richter, C. P., Milot, R. L., Cai, L., Schmuttenmaer, C. A., Crabtree, R. H., Batista, V. S. (2009). Synergistic effect between anatase and rutile TiO_2 nanoparticles in dye-sensitized solar cells. *Dalton Transactions*, (45), 10078–10085.

Li, H., Shen, X., Liu, Y., Wang, L., Lei, J., & Zhang, J. (2015). Facile phase control for hydrothermal synthesis of anatase-rutile TiO_2 with enhanced photocatalytic activity. *Journal of Alloys and Compounds*, *646*, 380–386.

Li, H., Zhang, W., Guan, L. X., Li, F., & Yao, M. M. (2015). Visible light active TiO_2-ZnO composite films by cerium and fluorine codoping for photocatalytic decontamination. *Materials Science in Semiconductor Processing*, *40*, 310–318.

Li, H., Zhou, Y., Du, G., Huang, Y., & Ji, Z. (2018). Effects of Piezoelectric Potential of ZnO on Resistive Switching Characteristics of Flexible ZnO/TiO_2 Heterojunction Cells. *Journal of Electronic Materials*, *47*(3), 1762–1767.

Li, J., Jia, S., Sui, G., Du, L., & Li, B. (2017). Preparation of hollow Nd/TiO_2 sub-microspheres with enhanced visible-light photocatalytic activity. *RSC Advances*, *7*(55), 34857–34865.

Li, N., Han, R., & Lu, X. (2018). Bibliometric analysis of research trends on solid waste reuse and recycling during 1992–2016. *Resources, Conservation and Recycling*, *130*, 109–117.

Li, W., Liang, R., Hu, A., Huang, Z., & Zhou, Y. N. (2014). Generation of oxygen vacancies in visible light activated one-dimensional iodine TiO_2 photocatalysts. *RSC Advances*, *4*(70), 36959.

Li, X., Shi, J., Chen, H., Wan, R., Leng, C., Chen, S., & Lei, Y. (2017). A DFT study on the modification mechanism of (Cr, C) co-doping for the electronic and optical properties of anatase TiO_2. *Computational Materials Science*, *129*, 295–303.

Li, Y., Wang, W., Qiu, X., Song, L., Meyer, H. M., Paranthaman, M. P., Gu, B. (2011). Comparing Cr, and N only doping with (Cr, N)-codoping for enhancing visible light reactivity of TiO_2. *Applied Catalysis B: Environmental*, *110*, 148–153.

Li, Z., Cong, S., & Xu, Y. (2014). Brookite vs anatase TiO_2 in the photocatalytic activity for organic degradation in water. *ACS Catalysis*, *4*(9), 3273–3280.

Liang, H., Jia, Z., Zhang, H., Wang, X., & Wang, J. (2017). Photocatalysis oxidation activity regulation of Ag/TiO_2 composites evaluated by the selective oxidation of Rhodamine B. *Applied Surface Science*, *422*, 1–10.

Lim, M., Zhou, Y., Wood, B., Guo, Y., Wang, L., Rudolph, V., & Lu, G. (2008). Fluorine and carbon codoped macroporous titania microspheres: highly effective photocatalyst for the destruction of airborne styrene under visible light. *The Journal of Physical Chemistry C*, *112*(49), 19655–19661.

Liu, G., Sun, C., Yan, X., Cheng, L., Chen, Z., Wang, X., Cheng, H.-M. (2009). Iodine doped anatase TiO_2 photocatalyst with ultra-long visible light response: correlation between geometric/electronic structures and mechanisms. *Journal of Materials Chemistry*, *19*(18), 2822–2829.

Liu, G., Wang, X., Chen, Z., Cheng, H.-M., & Lu, G. Q. M. (2009). The role of crystal phase in determining photocatalytic activity of nitrogen doped TiO_2. *Journal of Colloid and Interface Science*, *329*(2), 331–338.

Liu, H., Liu, G., Xie, G., Zhang, M., Hou, Z., & He, Z. (2011). Gd^{3+}, N-codoped trititanate nanotubes: Preparation, characterization and photocatalytic activity. *Applied Surface Science*, *257*(8), 3728–3732.

Liu, K., Zhang, Z., Lu, N., & Dong, B. (2018). In Situ Generation of Copper Species Nanocrystals in TiO_2 Electrospun Nanofibers: A Multi-hetero-junction Photocatalyst for Highly Efficient Water Reduction. *ACS Sustainable Chemistry & Engineering*, *6*(2), 1934–1940.

Liu, R., Wang, P., Wang, X., Yu, H., & Yu, J. (2012). UV- and visible-light photocatalytic activity of simultaneously deposited and doped $Ag/Ag(I)\text{-}TiO_2$ photocatalyst. *Journal of Physical Chemistry C*, *116*(33), 17721–17728.

Liu, R., Yin, Z., Leng, Y., Hang, W., & Huang, B. (2018). Direct and comprehensive analysis of dyes based on integrated molecular and structural information via laser desorption laser postionization mass spectrometry. *Talanta*, *176*, 116–123.

Liu, S., Guo, E., Yin, L., Yu, J. C., Yu, J. G., Zhao, J. C., Do, Y. R. (2012). Tailored visible-light driven anatase TiO_2 photocatalysts based on controllable metal ion doping and ordered mesoporous structure. *Journal of Materials Chemistry*, *22*(11),

Liu, X., Li, Y., Deng, D., Chen, N., Xing, X., & Wang, Y. (2016a). A one-step nonaqueous sol–gel route to mixed-phase TiO_2 with enhanced photocatalytic

degradation of Rhodamine B under visible light. *CrystEngComm*, *18*(11), 1964–1975.

Liu, Z., Fang, P., Wang, S., Gao, Y., Chen, F., Zheng, F., Dai, Y. (2012). Photocatalytic degradation of gaseous benzene with CdS-sensitized TiO_2 film coated on fiberglass cloth. *Journal of Molecular Catalysis A: Chemical*, *363*, 159–165.

Long, R., Dai, Y., & Huang, B. (2009). Structural and electronic properties of iodine-doped anatase and rutile TiO_2. *Computational Materials Science*, *45*(2), 223–228.

López, R., Gómez, R., & Llanos, M. E. (2009). Photophysical and photocatalytic properties of nanosized copper-doped titania sol–gel catalysts. *Catalysis Today*, *148*(1), 103–108.

Low, J., Cheng, B., & Yu, J. (2017). Surface modification and enhanced photocatalytic CO_2 reduction performance of TiO_2: a review. *Applied Surface Science*, *392*, 658–686.

Lu, D., Zhao, B., Fang, P., Zhai, S., Li, D., Chen, Z., Qi, N. (2015). Applied Surface Science Facile one-pot fabrication and high photocatalytic performance of vanadium doped TiO_2 -based nanosheets for visible-light-driven degradation of RhB or Cr(VI). *Applied Surface Science*, *359*, 435–448.

Luo, B., Li, Z., & Xu, Y. (2015). The positive effect of anatase and rutile on the brookite-photocatalyzed degradation of phenol. *RSC Advance.*, *5*(128), 105999–106004.

Mahmoodi, N. M., & Arami, M. (2009). Degradation and toxicity reduction of textile wastewater using immobilized titania nanophotocatalysis. *Journal of Photochemistry and Photobiology B: Biology*, *94*(1), 20–24.

Meng, A., Zhu, B., Zhong, B., Zhang, L., & Cheng, B. (2017). Direct Z-scheme TiO_2/CdS hierarchical photocatalyst for enhanced photocatalytic H_2-production activity. *Applied Surface Science*, *422*, 518–527.

Miller, C. J., Wadley, S., & Waite, T. D. (2017). Fenton, photo-Fenton and Fenton-like processes. *Advanced Oxidation Processes for Water Treatment: Fundamentals and Applications*, 297.

Miyauchi, M., Nakajima, A., Watanabe, T., & Hashimoto, K. (2002). Photoinduced hydrophilic conversion of TiO_2/WO_3 layered thin films. *Chemistry of Materials*, *14*(11), 4714–4720.

Mogal, S. I., Gandhi, V. G., Mishra, M., Tripathi, S., Shripathi, T., Joshi, P. A., & Shah, D. O. (2014). Single-step synthesis of silver-doped titanium dioxide: Influence of silver on structural, textural, and photocatalytic properties. *Industrial and Engineering Chemistry Research*, *53*(14), 5749–5758.

Mohamed, M. M., Othman, I., & Mohamed, R. M. (2007). Synthesis and characterization of MnOx/TiO_2 nanoparticles for photocatalytic oxidation of indigo carmine dye. *Journal of Photochemistry and Photobiology A: Chemistry*, *191*(2), 153–161.

Moradi, H., Eshaghi, A., Hosseini, S. R., & Ghani, K. (2016). Fabrication of Fe-doped TiO_2 nanoparticles and investigation of photocatalytic decolorization of reactive red 198 under visible light irradiation. *Ultrasonics Sonochemistry*, *32*, 314–319.

Moradi, V., Jun, M. B. G., Blackburn, A., & Herring, R. A. (2018). Significant improvement in visible light photocatalytic activity of Fe doped TiO_2 using an acid treatment process. *Applied Surface Science*, *427*, 791–799.

Morikawa, T., Asahi, R., Ohwaki, T., Aoki, K., & Taga, Y. (2001). Band-gap narrowing of titanium dioxide by nitrogen doping. *Japanese Journal of Applied Physics*, *40*(6A), L561.

Mousavi, M., & Habibi-Yangjeh, A. (2016). Magnetically separable ternary g-C_3N_4/Fe_3O_4/BiOI nanocomposites: Novel visible-light-driven photocatalysts based on graphitic carbon nitride. *Journal of Colloid and Interface Science*, *465*, 83–92.

Murugesan, K., Dhamija, A., Nam, I.-H., Kim, Y.-M., & Chang, Y.-S. (2007). Decolourization of reactive black 5 by laccase: optimization by response surface methodology. *Dyes and Pigments*, *75*(1), 176–184.

Ncibi, M. C., Mahjoub, B., & Seffen, M. (2007). Kinetic and equilibrium studies of methylene blue biosorption by Posidonia oceanica (L.) fibres. *Journal of Hazardous Materials*, *139*(2), 280–285.

Neamen, D. A. (2012). *Semiconductor Physics and Devices: Basic Principles*. McGraw-Hill Education, USA.

Nicholls, D. (1974). Electronic Spectra of Transition-metal Complexes. In *Complexes and First-Row Transition Elements* (pp. 73–99). Springer, USA.

Niu, X., Yu, J., Wang, L., Fu, C., Wang, J., Wang, L.,Yang, J. (2017). Enhanced photocatalytic performance of TiO_2 nanotube based heterojunction photocatalyst via the coupling of graphene and FTO. *Applied Surface Science*, *413*, 7–15.

Nolan, N., Seery, M., & Pillai, S. (2009). Spectroscopic Investigation of the Anatase-to-Rutile Transformation of Sol− Gel-Synthesized TiO_2 Photocatalysts. *The Journal of Physical Chemistry C*, *113*, 1615–16157.

Nosaka, Y., & Nosaka, A. Y. (2017). Generation and detection of reactive oxygen species in photocatalysis. *Chemical Reviews*, *117*(17), 11302–11336.

O'Regan, B., & Gratzel, M. (1991). A Low-Cost, High-Efficiency Solar-Cell Based on Dye-Sensitized Colloidal TiO_2 Films. *Nature*, *353*(6346), 737–740.

Ola, O., & Maroto-Valer, M. M. (2015). Review of material design and reactor engineering on TiO_2 photocatalysis for CO_2 reduction. *Journal of Photochemistry and Photobiology C: Photochemistry Reviews*, *24*, 16–42.

Ola, O., & Maroto-Valer, M. M. (2015). Transition metal oxide based TiO_2 nanoparticles for visible light induced CO_2 photoreduction. *Applied Catalysis A: General*, *502*, 114–121.

Ouyang, J., Chang, M., & Li, X. (2012). CdS-sensitized ZnO nanorod arrays coated with TiO2 layer for visible light photoelectrocatalysis. *Journal of Materials Science*, *47*(9), 4187–4193.

Pajot, B., & Clerjaud, B. (2012). *Optical Absorption of Impurities and Defects in Semiconducting Crystals: Electronic Absorption of Deep Centres and Vibrational Spectra* (Vol. 169). Springer Science & Business Media, USA.

Pelaez, M., Nolan, N. T., Pillai, S. C., Seery, M. K., Falaras, P., Kontos, A. G., Dionysiou, D. D. (2012). A review on the visible light active titanium dioxide photocatalysts for environmental applications. *Applied Catalysis B: Environmental*, *125*, 331–349.

Peng, B., Meng, X., Tang, F., Ren, X., Chen, D., & Ren, J. (2009). General synthesis and optical properties of monodisperse multifunctional metal-ion-doped TiO_2 hollow particles. *The Journal of Physical Chemistry C*, *113*(47), 20240–20245.

Pham, T.-T., Nguyen-Huy, C., Lee, H.-J., Nguyen-Phan, T.-D., Son, T. H., Kim, C.-K., & Shin, E. W. (2015). Cu-doped TiO_2/reduced graphene oxide thin-film photocatalysts: Effect of Cu content upon methylene blue removal in water. *Ceramics International*, *41*(9), 11184–11193.

Pilkenton, S., & Raftery, D. (2003). Solid-state NMR studies of the adsorption and photooxidation of ethanol on mixed TiO_2–SnO_2 photocatalysts. *Solid State Nuclear Magnetic Resonance*, *24*(4), 236–253.

Prasannalakshmi, P., & Shanmugam, N. (2017). Fabrication of TiO_2/ZnO nanocomposites for solar energy driven photocatalysis. *Materials Science in Semiconductor Processing*, *61*(January), 114–124.

Ghaly, A. E., Ananthashankar, R., Alhattab, M. V. V. R., & Ramakrishnan, V. V. (2014). Production, characterization and treatment of textile effluents: a critical review. *Journal of Chemical Engineering & Process Technology*, 5(1), 1-19..

Nosaka, Y., & Nosaka, A. (2016). Understanding hydroxyl radical (• OH) generation processes in photocatalysis. *ACS Energy Letters*, 1(2), 356-359.

Rajkumar, D., & Kim, J. G. (2006). Oxidation of various reactive dyes with in situ electro-generated active chlorine for textile dyeing industry wastewater treatment. *Journal of Hazardous Materials*, *136*(2), 203–212.

Ren, W., Ai, Z., Jia, F., Zhang, L., Fan, X., & Zou, Z. (2007). Low temperature preparation and visible light photocatalytic activity of mesoporous carbon-doped crystalline TiO_2. *Applied Catalysis B: Environmental*, *69*(3), 138–144.

Reszczyńska, J., Grzyb, T., Sobczak, J. W., Lisowski, W., Gazda, M., Ohtani, B., & Zaleska, A. (2014). Lanthanide co-doped TiO_2: the effect of metal type and amount on surface properties and photocatalytic activity. *Applied Surface Science*, *307*, 333–345.

Robert, D. (2007). Photosensitization of TiO_2 by M_xO_y and M_xS_y nanoparticles for heterogeneous photocatalysis applications. *Catalysis Today*, *122*(1), 20–26.

Sahu, M., & Biswas, P. (2011). Single-step processing of copper-doped titania nanomaterials in a flame aerosol reactor. *Nanoscale Research Letters*, *6*(1), 441.

Sakatani, Y., Ando, H., Okusako, K., Koike, H., Nunoshige, J., Takata, T., Domen, K. (2004). Metal ion and N co-doped TiO_2 as a visible-light photocatalyst. *Journal of Materials Research*, *19*(7), 2100–2108.

Sakatani, Y., Nunoshige, J., Ando, H., Okusako, K., Koike, H., Takata, T., Domen, K. (2003). Photocatalytic decomposition of acetaldehyde under visible light irradiation over La^{3+} and N co-doped TiO_2. *Chemistry Letters*, *32*(12), 1156–1157.

Samsudin, E. M., & Abd Hamid, S. B. (2017). Effect of band gap engineering in anionic-doped TiO_2 photocatalyst. *Applied Surface Science*, *391*, 326–336.

Serpone, N. (2006). Is the band gap of pristine TiO_2 narrowed by anion-and cation-doping of titanium dioxide in second-generation photocatalysts. *ACS Publications.*

Shahzad, M. W., Burhan, M., Ang, L., & Ng, K. C. (2017). Energy-water-environment nexus underpinning future desalination sustainability. *Desalination*, *413*, 52–64.

Shao-You, L., Qun-Li, T., & Qing-Ge, F. (2011). Synthesis of S/Cr doped mesoporous TiO_2 with high-active visible light degradation property via solid state reaction route. *Applied Surface Science*, *257*(13), 5544–5551.

Shao, G. (2008b). Electronic Structures of Manganese-Doped Rutile TiO_2 from First Principles, 18677–18685.

Shayegan, Z., Lee, C.-S., & Haghighat, F. (2017). TiO_2 photocatalyst for removal of volatile organic compounds in gas phase – A review. *Chemical Engineering,* 334, 2408–2439.

Shi, L., & Weng, D. (2008). Formation of impurity bands in iodine cation substitutionally doped TiO_2 and its effects on photoresponse and photogenerated carriers. *Physics Letters A*, *372*(37), 5901–5904.

Silva, G. T. S. T., Carvalho, K. T. G., Lopes, O. F., Gomes, E. S., Malagutti, A. R., Mastelaro, V. R., Mourão, H. A. J. L. (2017). Synthesis of ZnO nanoparticles assisted by N-sources and their application in the photodegradation of organic contaminants. *ChemCatChem*, 9(19), 3795–3804.

Slav, A. (2011). Optical characterization of TiO_2-Ge nanocomposite films obtained by reactive magnetron sputtering. *Digest Journal of Nanomaterials and Biostructures*, *6*(3), 915–920.

Song, S., Hong, F., He, Z., Wang, H., Xu, X., & Chen, J. (2011). Influence of zirconium doping on the activities of zirconium and iodine co-doped titanium dioxide in the decolorization of methyl orange under visible light irradiation. *Applied Surface Science*, *257*(23), 10101–10108.

Song, S., Tu, J., He, Z., Hong, F., Liu, W., & Chen, J. (2010). Visible light-driven iodine-doped titanium dioxide nanotubes prepared by hydrothermal process and post-calcination. *Applied Catalysis A: General*, *378*(2), 169–174.

Soria, J., Conesa, J. C., Augugliaro, V., Palmisano, L., Schiavello, M., & Sclafani, A. (1991). Dinitrogen photoreduction to ammonia over titanium dioxide powders doped with ferric ions. *The Journal of Physical Chemistry*, *95*(1), 274–282.

Soutsas, K., Karayannis, V., Poulios, I., Riga, A., Ntampegliotis, K., Spiliotis, X., & Papapolymerou, G. (2010). Decolorization and degradation of reactive azo dyes via heterogeneous photocatalytic processes. *Desalination*, *250*(1), 345–350.

Štengl, V., Bakardjieva, S., & Murafa, N. (2009). Preparation and photocatalytic activity of rare earth doped TiO_2 nanoparticles. *Materials Chemistry and Physics*, *114*(1), 217–226.

Su, R., Bechstein, R., Kibsgaard, J., Vang, R. T., & Besenbacher, F. (2012). High-quality Fe-doped TiO_2 films with superior visible-light performance. *Journal of Materials Chemistry*, *22*(45), 23755.

Su, W., Zhang, Y., Li, Z., Wu, L., Wang, X., Li, J., & Fu, X. (2008). Multivalency iodine doped TiO_2: preparation, characterization, theoretical studies, and visible-light photocatalysis. *Langmuir*, *24*(7), 3422–3428.

Su, Y., Xiao, Y., Li, Y., Du, Y., & Zhang, Y. (2011). Preparation, photocatalytic performance and electronic structures of visible-light-driven Fe-N-codoped TiO_2 nanoparticles. *Materials Chemistry and Physics*, *126*(3), 761–768.

Subramanian, M., Vijayalakshmi, S., Venkataraj, S., & Jayavel, R. (2008). Effect of cobalt doping on the structural and optical properties of TiO_2 films prepared by sol–gel process. *Thin Solid Films*, *516*(12), 3776–3782.

Sureshkumar, T., Thiripuranthagan, S., Paskalis, S. M. K., Kumaravel, S., Kannan, K., & Devarajan, A. (2018). Synthesis, characterization and photodegradation activity of graphitic C_3N_4-$SrTiO_3$ nanocomposites. *Journal of Photochemistry and Photobiology A: Chemistry*, *356*, 425–439.

Tabasideh, S., Maleki, A., Shahmoradi, B., Ghahremani, E., & McKay, G. (2017). Sonophotocatalytic degradation of diazinon in aqueous solution using iron-doped TiO_2 nanoparticles. *Separation and Purification Technology*, *189*, 186–192.

Tahir, H., Saad, M., Saud, A., & Saleem, U. (2018). Synthesis and Characterization of Kaolin Assisted Metal Nanocomposite and its Tremendous Adsorptive and Photo Catalytic Applications. *Journal of the Chemical Society of Pakistan*, *40*(1), 64–68.

Tahir, M., & Amin, N. S. (2015). Indium-doped TiO_2 nanoparticles for photocatalytic CO_2 reduction with H_2O vapors to CH_4. *Applied Catalysis B: Environmental*, *162*, 98–109.

Tan, P., Chen, X., Wu, L., Shang, Y. Y., Liu, W., Pan, J., & Xiong, X. (2017). Hierarchical flower-like $SnSe_2$ supported Ag_3PO_4 nanoparticles: Towards visible light driven photocatalyst with enhanced performance. *Applied Catalysis B: Environmental*, *202*, 326–334.

Tan, Y. N., Wong, C. L., & Mohamed, A. R. (2011). An Overview on the Photocatalytic Activity of Nano-Doped-TiO_2 in the Degradation of Organic

Pollutants. *ISRN Materials Science*, *2011*.

Tang, H., Chang, S., Wu, K., Tang, G., Fu, Y., Liu, Q., & Yang, X. (2016). Band gap and morphology engineering of TiO_2 by silica and fluorine co-doping for efficient ultraviolet and visible photocatalysis. *RSC Advances*, *6*(68), 63117–63130.

Teh, C. M., & Mohamed, A. R. (2011). Roles of titanium dioxide and ion-doped titanium dioxide on photocatalytic degradation of organic pollutants (phenolic compounds and dyes) in aqueous solutions: a review. *Journal of Alloys and Compounds*, *509*(5), 1648–1660.

Tejasvi, R., Sharma, M., & Upadhyay, K. (2015). Passive photo-catalytic destruction of air-borne VOCs in high traffic areas using TiO_2-coated flexible PVC sheet. *Chemical Engineering Journal*, *262*, 875–881.

Tian, Z., Yu, N., Cheng, Y., Wang, Z., Chen, Z., & Zhang, L. (2017). Hydrothermal synthesis of graphene/TiO_2/CdS nanocomposites as efficient visible-light-driven photocatalysts. *Materials Letters*, *194*(3), 172–175.

Tieng, S., Kanaev, A., & Chhor, K. (2011). New homogeneously doped Fe(III)-TiO_2 photocatalyst for gaseous pollutant degradation. *Applied Catalysis A: General*, *399*(1–2), 191–197.

Tojo, S., Tachikawa, T., Fujitsuka, M., & Majima, T. (2008). Iodine-doped TiO_2 photocatalysts: correlation between band structure and mechanism. *The Journal of Physical Chemistry C*, *112*(38), 14948–14954.

Tristão, J. C., Magalhães, F., Corio, P., & Sansiviero, M. T. C. (2006). Electronic characterization and photocatalytic properties of CdS/TiO_2 semiconductor composite. *Journal of Photochemistry and Photobiology A: Chemistry*, *181*(2), 152–157.

Tseng, I. H., Wu, J. C. S., & Chou, H. Y. (2004). Effects of sol-gel procedures on the photocatalysis of Cu/TiO_2 in CO_2 photoreduction. *Journal of Catalysis*, *221*(2), 432–440.

Tsuyumoto, I., & Nawa, K. (2008). Thermochromism of vanadium–titanium oxide prepared from peroxovanadate and peroxotitanate. *Journal of Materials Science*, *43*(3), 985–988.

Ullah, H., Khan, K. A., & Khan, W. U. (2014). ZnO/TiO_2 Nanocomposite Synthesized by Sol Gel from Highly Soluble Single Source Molecular Precursor. *Chinese Journal of Chemical Physics*, *27*(5), 548–554.

Urgency, U. (2007). Water Caucus Summary. *World Water Council (WWC),* Marseille, France.

Wang, B., Leung, M. K. H., Lu, X.-Y., & Chen, S.-Y. (2013). Synthesis and photocatalytic activity of boron and fluorine codoped TiO_2 nanosheets with reactive facets. *Applied Energy*, *112*, 1190–1197.

Wang, C., Ao, Y., Wang, P., Hou, J., & Qian, J. (2011). Preparation of cerium and

nitrogen co-doped titania hollow spheres with enhanced visible light photocatalytic performance. *Powder Technology*, *210*(3), 203–207.

Wang, C., Chen, Z., Jin, H., Cao, C., Li, J., & Mi, Z. (2014). Enhancing visible-light photoelectrochemical water splitting through transition-metal doped TiO_2 nanorod arrays. *Journal of Materials Chemistry A*, *2*(42), 17820–17827.

Wang, C. L., Lee, H. Y., Azough, F., & Freer, R. (1997). The microstructure and microwave dielectric properties of zirconium titanate ceramics in the solid solution system $ZrTiO_4$–$Zr_5Ti_7O_{24}$. *Journal of Materials Science*, *32*(7), 1693–1701.

Wang, J., Huang, B., Wang, Z., Qin, X., & Zhang, X. (2011). Synthesis and characterization of C, N-codoped TiO_2 nanotubes/nanorods with visible-light activity. *Rare Metals*, *30*(1), 161–165.

Wang, M.-C., Lin, H.-J., Wang, C.-H., & Wu, H.-C. (2012). Effects of annealing temperature on the photocatalytic activity of N-doped TiO_2 thin films. *Ceramics International*, *38*(1), 195–200.

Wang, P., Lu, Y., Wang, X., & Yu, H. (2017). Co-modification of amorphous-Ti(IV) hole cocatalyst and $Ni(OH)_2$ electron cocatalyst for enhanced photocatalytic H_2-production performance of TiO_2. *Applied Surface Science*, *391*, 259–266.

Wang, P., Yap, P.-S., & Lim, T.-T. (2011). C–N–S tridoped TiO_2 for photocatalytic degradation of tetracycline under visible-light irradiation. *Applied Catalysis A: General*, *399*(1), 252–261.

Wang, R., Tan, H., Zhao, Z., Zhang, G., Song, L., Dong, W., & Sun, Z. (2014). Stable ZnO@TiO_2 core/shell nanorod arrays with exposed high energy facets for self-cleaning coatings with anti-reflective properties. *Journal of Materials Chemistry A*, *2*(20), 7313.

Wang, R., Tan, H., Zhao, Z., Zhang, G., Song, L., Dong, W., & Sun, Z. (2014). Stable ZnO@TiO2 core/shell nanorod arrays with exposed high energy facets for self-cleaning coatings with anti-reflective properties. *Journal of Materials Chemistry A*, *2*(20), 7313–7318.

Wang, S., Shi, X., Shao, G., Duan, X., Yang, H., & Wang, T. (2008). Preparation, characterization and photocatalytic activity of multi-walled carbon nanotube-supported tungsten trioxide composites. *Journal of Physics and Chemistry of Solids*, *69*(10), 2396–2400.

Wang, W. K., Chen, J. J., Gao, M., Huang, Y. X., Zhang, X., & Yu, H. Q. (2016). Photocatalytic degradation of atrazine by boron-doped TiO2 with a tunable rutile/anatase ratio. *Applied Catalysis B: Environmental*, *195*, 69–76.

Wang, X., Li, T., Yu, R., Yu, H., & Yu, J. (2016). Highly efficient TiO_2 single-crystal photocatalyst with spatially separated Ag and F^- bi-cocatalysts: orientation transfer of photogenerated charges and their rapid interfacial reaction. *Journal of Materials Chemistry A*, *4*(22), 8682–8689.

Wang, X., Song, J., Huang, J., Zhang, J., Wang, X., Ma, R. R., Zhao, J. (2016).

Activated carbon-based magnetic TiO_2 photocatalyst codoped with iodine and nitrogen for organic pollution degradation. *Applied Surface Science*, *390*, 190–201.

Wang, Y., Huang, Y., Ho, W., Zhang, L., Zou, Z., & Lee, S. (2009). Biomolecule-controlled hydrothermal synthesis of C-N-S-tridoped TiO_2 nanocrystalline photocatalysts for NO removal under simulated solar light irradiation. *Journal of Hazardous Materials*, *169*(1–3), 77–87.

Wang, Y. R., Li, S., & Yi, J. B. (2018). Transition Metal-Doped Tin Monoxide Monolayer: A First-Principles Study. *The Journal of Physical Chemistry C*, *122*(8), 4651–4661.

Wei, F., Ni, L., & Cui, P. (2008). Preparation and characterization of N–S-codoped TiO_2 photocatalyst and its photocatalytic activity. *Journal of Hazardous Materials*, *156*(1), 135–140.

Wen, C., Zhu, Y.-J., Kanbara, T., Zhu, H.-Z., & Xiao, C.-F. (2009). Effects of I and F codoped TiO_2 on the photocatalytic degradation of methylene blue. *Desalination*, *249*(2), 621–625.

Wen, J., Li, X., Liu, W., Fang, Y., Xie, J., & Xu, Y. (2015). Photocatalysis fundamentals and surface modification of TiO_2 nanomaterials. *Chinese Journal of Catalysis*, *36*(12), 2049–2070.

Wu, J., Liu, Q., Gao, P., & Zhu, Z. (2011). Influence of praseodymium and nitrogen co-doping on the photocatalytic activity of TiO_2. *Materials Research Bulletin*, *46*(11), 1997–2003.

Wu, M.-C., Wu, P.-Y., Lin, T.-H., & Lin, T.-F. (2018). Photocatalytic performance of Cu-doped TiO_2 nanofibers treated by the hydrothermal synthesis and air-thermal treatment. *Applied Surface Science*, *430*, 390–398.

Wu, X., Yin, S., Dong, Q., Guo, C., Kimura, T., Matsushita, J. I., & Sato, T. (2013). Photocatalytic properties of Nd and C Codoped TiO_2 with the Whole range of visible light absorption. *Journal of Physical Chemistry C*, *117*(16), 8345–8352.

Xia, X. H., Gao, Y., Wang, Z., & Jia, Z. J. (2008). Structure and photocatalytic properties of copper-doped rutile TiO_2 prepared by a low-temperature process. *Journal of Physics and Chemistry of Solids*, *69*(11), 2888–2893.

Xia, Y., Li, Q., Lv, K., & Li, M. (2017). Heterojunction construction between TiO_2 hollowsphere and $ZnIn_2S_4$ flower for photocatalysis application. *Applied Surface Science*, *398*, 81–88.

Xiao, Q., Ouyang, L., Gao, L., & Yao, C. (2011). Preparation and visible light photocatalytic activity of mesoporous N, S-codoped TiO_2 (B) nanobelts. *Applied Surface Science*, *257*(8), 3652–3656.

Xu, J., Ao, Y., Fu, D., & Yuan, C. (2008). A simple route for the preparation of Eu, N-codoped TiO_2 nanoparticles with enhanced visible light-induced photocatalytic activity. *Journal of Colloid and Interface Science*, *328*(2), 447–451.

Yamashita, H., Nishiguchi, H., Kamada, N., Anpo, M., Teraoka, Y., Hatano, H., Sclafani, A. (1994). Photocatalytic reduction of CO_2 with H_2O on TiO_2 and Cu/TiO_2 catalysts. *Research on Chemical Intermediates*, *20*(8), 815–823.

Yan, J., Wu, G., Guan, N., & Li, L. (2014). Nb_2O_5/TiO_2 heterojunctions: Synthesis strategy and photocatalytic activity. *Applied Catalysis B: Environmental*, *152–153*(1), 280–288.

Yan, Y., Yu, Y., Cao, C., Huang, S., Yang, Y., Yang, X., & Cao, Y. (2016). Enhanced photocatalytic activity of TiO_2–Cu/C with regulation and matching of energy levels by carbon and copper for photoreduction of CO_2 into CH_4. *CrystEngComm*, *18*(16), 2956–2964.

Yang, J., Dai, J., & Li, J. (2011). Synthesis, characterization and degradation of Bisphenol A using Pr, N co-doped TiO_2 with highly visible light activity. *Applied Surface Science*, *257*(21), 8965–8973.

Yang, R., Lu, X., Zhang, Z., Wang, X., Tang, D., & Zhu, L. (2015). Three-dimensionally ordered macroporous $LaMnO_3$ with tunable oxygen vacancies via nitric acid-aided modulating and their catalytic combustion properties. *RSC Advances*, *5*(119), 98404–98411.

Yang, X., Qin, J., Jiang, Y., Li, R., Li, Y., & Tang, H. (2014). Bifunctional TiO_2 /Ag_3PO_4 /graphene composites with superior visible light photocatalytic performance and synergistic inactivation of bacteria. *RSC Advances*, *4*(36), 18627–18636.

Yoon, J.-W. (2009). Dispersion of nanosized noble metals in TiO_2 matrix and their photoelectrode properties. *Journal of the Korean Crystal Growth and Crystal Technology*, *19*(5), 251–255.

Yoshida, T., Niimi, S., Yamamoto, M., Nomoto, T., & Yagi, S. (2015). Effective nitrogen doping into TiO_2 (N-TiO_2) for visible light response photocatalysis. *Journal of Colloid and Interface Science*, *447*, 278–281.

Yu, W., Zhang, J., & Peng, T. (2016). New insight into the enhanced photocatalytic activity of N-, C- and S-doped ZnO photocatalysts. *Applied Catalysis B: Environmental*, *181*, 220–227.

Yuan, Y.-P., Ruan, L.-W., Barber, J., Loo, S. C. J., & Xue, C. (2014). Hetero-nanostructured suspended photocatalysts for solar-to-fuel conversion. *Energy & Environmental Science*, *7*(12), 3934–3951.

Zahoor, M., Arshad, A., Khan, Y., Iqbal, M., Bajwa, S. Z., Soomro, R. A.,Wu, A. (2018). Enhanced photocatalytic performance of CeO_2–TiO_2 nanocomposite for degradation of crystal violet dye and industrial waste effluent. *Applied Nanoscience*, 1–9.

Zaleska, A. (2008). Doped-TiO_2: a review. *Recent Patents on Engineering*, *2*(3), 157–164.

Zha, R., Nadimicherla, R., & Guo, X. (2015). Ultraviolet photocatalytic degradation of methyl orange by nanostructured TiO_2/ZnO heterojunctions. *Journal of Materials*

Chemistry A, *3*(12), 6565–6574.

Zhang, C., Zhang, X., Wang, Y., Xie, S., Liu, Y., Lu, X., & Tong, Y. (2014). Facile electrochemical synthesis of CeO_2 hierarchical nanorods and nanowires with excellent photocatalytic activities. *New Journal of Chemistry*, *38*(6), 2581–2586.

Zhang, C., Zhou, Y., Bao, J., Zhang, Y., Fang, J., Zhao, S.,Sheng, X. (2018). Sn^{2+}-Doped Double-Shelled TiO_2 Hollow Nanospheres with Minimal Pt Content for Significantly Enhanced Solar H2 Production. *ACS Sustainable Chemistry & Engineering*.

Zhang, D., & Zeng, F. (2011). Photocatalytic oxidation of organic dyes with visible-light-driven codoped TiO_2 photocatalysts. *Russian Journal of Physical Chemistry A, Focus on Chemistry*, *85*(6), 1077–1083.

Zhang, H., Chen, G., & Bahnemann, D. W. (2009). Photoelectrocatalytic materials for environmental applications. *Journal of Materials Chemistry*, *19*(29), 5089–5121.

Zhang, Q., Li, Y., Ackerman, E. A., Gajdardziska-Josifovska, M., & Li, H. (2011). Visible light responsive iodine-doped TiO_2 for photocatalytic reduction of CO_2 to fuels. *Applied Catalysis A: General*, *400*(1–2), 195–202.

Zhang, Y., Gu, D., Zhu, L., & Wang, B. (2017). Highly ordered Fe^{3+}/TiO_2 nanotube arrays for efficient photocataltyic degradation of nitrobenzene. *Applied Surface Science*, *420*, 896–904.

Zhao, H., Liu, L., Andino, J. M., & Li, Y. (2013). Bicrystalline TiO_2 with controllable anatase–brookite phase content for enhanced CO_2 photoreduction to fuels. *Journal of Materials Chemistry A*, *1*(28), 8209.

Zhao, W., Zhang, M., Ai, Z., Yang, Y., Xi, H., Shi, Q., Shi, H. (2014). Synthesis, characterization, and photocatalytic properties of SnO_2/rutile TiO_2/anatase TiO_2 heterojunctions modified by Pt. *The Journal of Physical Chemistry C*, *118*(40), 23117–23125.

Zhao, Y., Tao, C., Xiao, G., & Su, H. (2017). Controlled synthesis and wastewater treatment of Ag_2O/TiO_2 modified chitosan-based photocatalytic film. *RSC Advances*, 7(18), 11211-11221.

Zheng, J., Xiong, F. Q., Zou, M., Thomas, T., Jiang, H., Tian, Y., & Yang, M. (2016). Enhanced photocatalytic degradation of rhodamine B under visible light irradiation on mesoporous anatase TiO_2 microspheres by codoping with W and N. *Solid State Sciences*, *54*, 49–53.

Zheng, X., Li, D., Li, X., Chen, J., Cao, C., Fang, J., Zheng, Y. (2015). Construction of ZnO/TiO_2 photonic crystal heterostructures for enhanced photocatalytic properties. *Applied Catalysis B: Environmental*, *168–169*, 408–415.

Zhou, L., Deng, J., Zhao, Y., Liu, W., An, L., & Chen, F. (2009). Preparation and characterization of N–I co-doped nanocrystal anatase TiO_2 with enhanced photocatalytic activity under visible-light irradiation. *Materials Chemistry and Physics*, *117*(2), 522–527.

Zhou, L., Wei, L., Yang, Y., Xia, X., Wang, P., Yu, J., & Luan, T. (2016). Improved performance of dye sensitized solar cells using Cu-doped TiO_2 as photoanode materials: Band edge movement study by spectroelectrochemistry. *Chemical Physics*, *475*, 1–8.

Zhou, P., Le, Z., Xie, Y., Fang, J., & Xu, J. (2017). Studies on facile synthesis and properties of mesoporous CdS/TiO_2 composite for photocatalysis applications. *Journal of Alloys and Compounds*, *692*, 170–177.

Zhou, P., Wu, J., Yu, W., Zhao, G., Fang, G., & Cao, S. (2014). Vectorial doping-promoting charge transfer in anatase TiO_2{0 0 1}surface. *Applied Surface Science*, *319*(1), 167–172.

Zhu, S., Xie, X., Chen, S. C., Tong, S., Lu, G., Pui, D. Y. H., & Sun, J. (2017). Cu-Ni nanowire-based TiO_2 hybrid for the dynamic photodegradation of acetaldehyde gas pollutant under visible light. *Applied Surface Science*, *408*, 117–124.

Zyoud, A., Zaatar, N., Saadeddin, I., Helal, M. H., Campet, G., Hakim, M., Hilal, H. S. (2011). Alternative natural dyes in water purification: anthocyanin as TiO_2-sensitizer in methyl orange photo-degradation. *Solid State Sciences*, *13*(6), 1268–1275.

LIST OF PUBLICATIONS AND PAPERS PRESENTED

1. **Dorraj, M.**, Alizadeh, M., Sairi, N. A., Basirun, W. J., Goh, B. T., Woi, P. M., & Alias, Y. (2017). Enhanced visible light photocatalytic activity of copper-doped titanium oxide–zinc oxide heterojunction for methyl orange degradation. *Applied Surface Science*, 414, 251-261.

2. **Dorraj, M.**, Goh, B. T., Sairi, N. A., Woi, P. M., & Basirun, W. J. (2018). Improved visible-light photocatalytic activity of TiO_2 co-doped with Copper and Iodine. *Applied Surface Science*, 439, 999-1009.

Applied Surface Science 414 (2017) 251–261

Contents lists available at ScienceDirect

Applied Surface Science

journal homepage: www.elsevier.com/locate/apsusc

Full length article

Enhanced visible light photocatalytic activity of copper-doped titanium oxide–zinc oxide heterojunction for methyl orange degradation

Masoumeh Dorraj[a,*], Mahdi Alizadeh[b], Nor Asrina Sairi[a,c,*], Wan Jefrey Basirun[a], Boon Tong Goh[d], Pei Meng Woi[a,c], Yatimah Alias[a,c]

[a] Department of Chemistry, Faculty of Science, University of Malaya, 50603 Kuala Lumpur, Malaysia
[b] UM Power Energy Dedicated Advanced Centre (UMPEDAC), Level 4 Wisma R&D, University of Malaya, Jalan Pantai Baharu, 59990 Kuala Lumpur, Malaysia
[c] University of Malaya Centre for Ionic Liquids, Department of Chemistry, Faculty of Science, University of Malaya, 50603 Kuala Lumpur, Malaysia
[d] Low Dimensional Materials Research Centre, Department of Physics, Faculty of Science, University of Malaya, 50603 Kuala Lumpur, Malaysia

ARTICLE INFO

Article history:
Received 18 January 2017
Received in revised form 27 March 2017
Accepted 6 April 2017
Available online 12 April 2017

Keywords:
Cu-TiO_2/ZnO
Heterojunction
Photocatalysts
Methyl orange
Visible light

ABSTRACT

A novel Cu-doped TiO_2 coupled with ZnO nanoparticles (Cu-TiO_2/ZnO) was prepared by sol-gel method and subsequent precipitation for methyl orange (MO) photodegradation under visible light irradiation. The compositions and shapes of the as-prepared Cu-TiO_2/ZnO nanocomposites were characterized by photoluminescence spectroscopy, X-ray diffraction, X-ray photoelectron spectroscopy, field emission scanning electron microscopy, transmission electron microscopy, UV–vis diffuse reflectance spectra and Brunauer–Emmett–Teller adsorption isotherm techniques. The Cu-TiO_2/ZnO nanocomposites showed considerably higher photocatalytic activity for MO removal from water under visible light irradiation than that of single-doped semiconductors. The effects of Cu-TiO_2 and ZnO mass ratios on the photocatalytic reaction were also studied. A coupling percentage of 30% ZnO exhibited the highest photocatalytic activity. The enhanced photocatalytic activity of the Cu-TiO_2/ZnO nanocomposites was mainly attributed to heterojunction formation, which allowed the efficient separation of photoinduced electron–hole pairs at the interface. Moreover, these novel nanocomposites could be recycled during MO degradation in a three-cycle experiment without evident deactivation, which is particularly important in environmental applications.

1. Introduction

Photocatalysts have been attracting significant attention as effective environment-friendly technology because of their wide spectral range of solar energy conversion into chemical energy. This technology is used to control and remove different types of organic pollutants in water. Among all the semiconductor-based photocatalysts, TiO_2 has been the ideal material because of its nontoxicity, high chemical stability, and oxidization feature [1,2]. However, the high TiO_2 bandgap energy restricts its practical application in the ultraviolet region, which corresponds to only 4%–5% of the entire solar spectrum. Hence, numerous studies have developed visible-light-driven TiO_2-based photocatalyst by doping metal [3,4] and non-metal [5–8] ions in the TiO_2 lattice. Transition-metal-doped TiO_2 can be effectively used to improve the visible-light-induced photocatalytic performance. Incorporating 3d transition metal ions in the titania crystal lattice creates impurity states close to the valence band (VB) and conduction band (CB), thereby resulting in a remarkable energy gap narrowing toward the visible region [9,10]. Guo and Du [11] reported that Cu doping can broaden the adsorption edge of TiO_2 in the visible region by forming dopant states above the VB caused by the Cu-3d orbital. Khalid et al. [12] reported that doping TiO_2 with Cu could enhance the visible light response and photocatalytic activity during methyl orange (MO) photodegradation. Although an improved photocatalytic activity of the bulk-doped TiO_2 particles has been reported, adverse side effects could not be eliminated because many of the newly created interband energy states can also act as recombination centers, which increase the recombination rate of charge carriers and degrade the photocatalytic activity [13–15].

* Corresponding authors at: Department of Chemistry, Faculty of Science, University of Malaya, 50603 Kuala Lumpur, Malaysia.
E-mail addresses: masidor20@gmail.com (M. Dorraj), asrina@um.edu.my (N.A. Sairi).

http://dx.doi.org/10.1016/j.apsusc.2017.04.045
0169-4332/

Applied Surface Science 439 (2018) 999–1009

Contents lists available at ScienceDirect

Applied Surface Science

journal homepage: www.elsevier.com/locate/apsusc

Full Length Article

Improved visible-light photocatalytic activity of TiO_2 co-doped with copper and iodine

Masoumeh Dorraj [a,*], Boon Tong Goh [b], Nor Asrina Sairi [a,c], Pei Meng Woi [a,c], Wan Jefrey Basirun [a,*]

[a] Department of Chemistry, Faculty of Science, University of Malaya, 50603 Kuala Lumpur, Malaysia
[b] Low Dimensional Materials Research Centre, Department of Physics, Faculty of Science, University of Malaya, 50603 Kuala Lumpur, Malaysia
[c] University of Malaya Centre for Ionic Liquids, Department of Chemistry, Faculty of Science, University of Malaya, 50603 Kuala Lumpur, Malaysia

ARTICLE INFO

Article history:
Received 23 October 2017
Revised 23 December 2017
Accepted 29 December 2017
Available online 10 January 2018

Keywords:
Codoped TiO_2
Photocatalytic degradation
Visible light absorption
Methyl orange

ABSTRACT

Cu-I-co-doped TiO_2 photocatalysts active to visible light absorption were prepared by hydrothermal method and calcined at various temperatures (350 °C, 450 °C, and 550 °C). The co-doped powders at 350 °C displayed the highest experimental Brunauer–Emmett–Teller surface area and lowest photoluminescence intensity, which demonstrated that a decrease in electron–hole recombination process. The synthesis of co-doped TiO_2 was performed at this optimized temperature. In the co-doped sample, the Cu^{2+} doped TiO_2 lattice created a major "red-shift" in the absorption edge due to the presence of the 3d Cu states, whereas the amount of red-shift from the I^{5+} doping in the TiO_2 lattice was minor. Interestingly, the presence of Cu^{2+} species also boosted the reduction of I^{5+} ions to the lower multivalance state I^- in the TiO_2 lattice by trapping the photogenerated electrons, which resulted in effective separation of the photogenerated charges. The Cu-I-co-doped TiO_2 was able to degrade methyl orange dye under visible-light irradiation with improved photocatalytic activity compared with the single metal-doped TiO_2 and pure TiO_2 because of the strong visible light absorption and effective separation of photogenerated charges caused by the synergistic effects of Cu and I co-dopants.

1. Introduction

TiO_2 has received considerable attention as an ideal photocatalytic material for the degradation of organic contaminants from wastewater or gas phase due to its high photoactivity, good photostability, cost effectiveness, and environmental friendliness [1,2]. Unfortunately, the poor capability of TiO_2 to absorb visible light as a main part of solar spectrum has limited its large-scale industrial applications [3]. For increased utilization of sunlight, various modifications have been made to the crystal structure of TiO_2-based materials, such as metal doping or non-metal element doping [4–9], coupling [10–14], and co-catalyst modification [15,16] for the enhanced absorption of sunlight. Among them, ion doping (either metal or nonmetal) is considered a simple and effective modification method that has been undertaken by several research groups to extend the light absorption from UV to the visible region [17–20] . In general, the dopant ions in the TiO_2 lattice introduce mid-gap energy states at the top of the valence band or at the bottom of the conduction band of TiO_2, which extend its absorption band edge from the UV to the visible-light region [21–25]. These as-produced impurity energy levels can also function as a trapping center for the effective separation of photogenerated electron–hole pairs, thus leading to increased photocatalytic activity [26]. However, these dopant ions must be utilized in small quantities to prevent subsequent recombination of electrons and holes. However, low concentration doping causes only a slight red shift of the optical absorption edge to the visible-light region, which is insufficient for the effective utilization of visible solar light [1,27]. Considering the increased doping concentration, the impurity levels act as electron–hole pair recombination sites that cause a negative effect on the photocatalytic activity [28,29]. In other words, extending the absorption edge to the visible region at the same time to prevent electron–hole recombination is a challenging task.

Recently, co-doping with two different types of ions has become a highly useful approach to improve the visible light-driven photocatalytic activity of TiO_2. In such system, the synergic combination of different types of dopants not only enhances the absorption of visible light but also decreases the photogenerated charge carrier recombination [1,3,30]. The N and C nonmetal dopants in TiO_2 have been widely utilized as co-dopants with various metals,

* Corresponding authors at: Department of Chemistry, Faculty of Science, University of Malaya, 50603 Kuala Lumpur, Malaysia.
E-mail addresses: masoumeh_dorraj@siswa.um.edu.my (M. Dorraj), jeff@um.edu.my (W.J. Basirun).

https://doi.org/10.1016/j.apsusc.2017.12.248
0169-4332/